TUBE EQUAL CHANNEL ANGULAR EXTRUSION AS A NOVEL SEVERE PLASTIC DEFORMATION TECHNIQUE FOR MG-3AL-1ZN ALLOY AND PURE NIOBIUM

A Dissertation

by

ABHINAV SRIVASTAVA

Submitted to the Graduate and Professional School of
Texas A&M University
in partial fulfillment of the requirements for the degree of

DOCTOR OF PHILOSOPHY

Chair of Committee,	Karl T. Hartwig
Co-Chair of Committee,	Ibrahim Karaman
Committee Members,	Ankit Srivastava
	Bilal Mansoor
Head of Department,	Ibrahim Karaman

August 2021

Major Subject: Materials Science and Engineering

ABSTRACT

Severe plastic deformation (SPD) processed ultrafine grained (UFG) materials are finding wide application in many industries because of their superior properties. Plenty of work has been done on the SPD processing of bar, plate, and rod forms of materials. Unfortunately, not much study has been conducted on improving the fabrication technique of tubular forms of materials. The conventional tube manufacturing processes involve either a seamless tube production method using high temperature extrusion which results in a large, non-uniform grain size or production of tubes that are seam welded after extrusion through a porthole or spider die. Welded regions are often the weak part of the tube and are prone to early failure.

An attractive substitute for conventional tube forming could be SPD processing that imparts high strength by reducing the grain size and not having a seam weld. To achieve improvement in the physical and mechanical properties of tubes, use of a novel SPD processing technique of tube equal channel angular extrusion (tECAE) is presented in this dissertation. Processing of magnesium (Mg) alloy and pure niobium (Nb) tubes were conducted in this study.

Mg alloys tubes are promising candidates to be used in biomedical industries for stent application, in transportation, and lightweight engineering application. Mg alloys are difficult to work with and possess anisotropic properties. The tECAE technique successfully processed Mg-3Al-1Zn alloy tubes at temperatures as low as 120 °C. The role of starting texture on strength and deformation behavior of the Mg alloy was

investigated by developing new processing routes. A viscoplastic self-consistent crystal plasticity model was used to supplement the experimental findings and improve the understanding of deformation modes in Mg alloy. Improved mechanical properties and unique textures were obtained after tECAE processing.

Pure Nb tubes were also tECAE processed. Nb tubes are important for particle accelerators to make superconducting radio frequency cavities. The effect of accumulated strain during tECAE processing on the grain size, texture, and post-processing recrystallization temperature was investigated.

This work shows that tECAE processing has the potential to reduce asymmetry in the mechanical properties and improve the strength and ductility by effective grain refinement.

DEDICATION

I dedicate this dissertation work:

To the loving memory of my mother Ranjana Srivastava.

To my father Anand Kumar Srivastava.

To my brother Ashvini and sister-in-law Ridhima.

To my sister Akanksha and brother-in-law Sandeep

Finally, to my fiancé Stuti Srivastava.

ACKNOWLEDGEMENTS

I would like to express my special thanks of gratitude to my advisor Dr. Karl T. Hartwig for his continuous guidance and support throughout my PhD education. His constant encouragement for writing and insightful discussions on the projects made my research experience exciting.

I would like to acknowledge my co-advisor Dr. Ibrahim Karaman for welcoming me in his research group and providing me complete freedom to conduct all my experiments. I will always remember the weekly meetings which helped me stay on track for my PhD. I am grateful for all the support he provided throughout my studies.

I thank Dr. Bilal Mansoor for hosting me at Texas A&M University Qatar campus for continuing my research there and having valuable discussions. I am also thankful to Dr. Ankit Srivastava for his support and valuable comments.

I am highly appreciative of Robert Barber for assisting with the SPD processing and discussions during the experiments. I would also like to thank Dr. Shreyas Balachandran for useful discussions on the niobium work. A special thanks to Michael Elverud and Dr. Anup Bandyopadhyay for their assistance in the lab.

I would also like to thank Dr. Wahaz Nazim and Matthew Vaughan for the valuable discussions on magnesium projects.

Special thanks to the wonderful graduate students and staff of Materials Science and Engineering department. Special thanks to Wesley Higgins and Dexin Zhao for help with the ion milling and EBSD. Thanks also goes to Dr. Tejas Umale, Dr. Daniel Salas,

Dr. Hande Ozcan, Hemant Rathod and many more friends for offering their advice, and friendship.

Last but not the least, this work would not have been possible without the constant support and love of my family.

CONTRIBUTORS AND FUNDING SOURCES

Contributors

This work was supervised by a dissertation committee consisting of Professor Karl T. Hartwig (advisor) and Professor Ibrahim Karaman (co-advisor) and Assistant Professor Ankit Srivastava of the Department of Materials Science and Engineering and Associate Professor Bilal Mansoor of the Department of Mechanical Engineering, Texas A&M University Qatar campus. The VPSC hardening parameters described in Chapter II were provided by Dr. Wahaz Nasim from the Materials Science and Engineering department. The SEM images shown in Chapter VI were provided by Dr. Shreyas Balachandran from National High Magnetic Field Lab, Tallahassee, Florida. All other work conducted for the dissertation was completed by the student independently.

Funding Sources

This work was made possible by a National Priorities Research Program (NPRP) grant from the Qatar National Research Fund (a member of The Qatar Foundation), under grant number NPRP 8-856-2-364, and the U.S. Department of Energy under grant number DE-SC0007601.

TABLE OF CONTENTS

Page

LIST OF FIGURES

Page

LIST OF TABLES

Page

CHAPTER I

INTRODUCTION AND LITERATURE REVIEW

1.1 Motivation

Tubular forms of materials are used in a variety of applications. The tubes are fabricated using conventional processes such as extrusion, welding, and casting [1-5]. Such conventionally produced tubes often show inhomogeneous grain size, non-uniform mechanical properties, and the presence of impurity elements. In many applications such as transportation of fluid, the conventionally processed tubes may provide adequate properties but there are certain instances where high purity, good formability, and homogenous mechanical and physical properties are desired such as for stent application [6, 7], high pressure fluid transfer [8], or tube as a precursor for hydroforming [4, 9]. Additionally, if inferior regions such as weld zones are present, the usability or further formability of the tubes get limited by the property of that region [2]. Therefore, a need exists to develop fabrication techniques that give axisymmetric properties, uniform microstructure, high strength, and good ductility to the tubes.

Severe plastic deformation (SPD) processes such as equal channel angular extrusion (ECAE) [10, 11] are widely used methods to refine grain size, alter texture, and improve formability in plate and bar forms of materials. The deformation is achieved via simple shear leading to grain refinement and microstructural uniformity. Materials can undergo multiple ECAE passes to homogenously refine the grain size via various routes that are based on the rotation of the billet [11]. ECAE also holds scale-up

capability providing it an advantage over some other SPD processes [12]. Although, ECAE has proven to be a successful SPD technique to process materials, only a limited work has been done on processing tubular forms of materials due to complications in tool design [13-16].

With the above information in mind, a novel method to process tubular forms of materials, using the principle of equal channel angular extrusion, called tube equal channel angular extrusion (tECAE) [17] is introduced in this study. The materials used for this processing are a magnesium (Mg) alloy tube and commercially pure reactor grade niobium (Nb) tube.

Magnesium alloy tubes are promising candidates to be used in the transportation industry and biomedical industry due to their high strength-to-weight ratio, adequate mechanical properties, and biocompatibility. Mg's use is limited because it shows low ductility, hence, it is difficult to perform forming operations on it. The commercially used techniques for magnesium tube fabrication include casting, extrusion, and porthole die extrusion that involves welding [18]. Such processing techniques often impart undesired texture, local composition variations, and a coarse grain size resulting in poor mechanical properties [1]. Although previous research works have demonstrated the potential of using ECAE for improving the formability and strength of Mg alloys bars and plates via grain refinement, favorable texture modification, and redistribution of secondary phases [19-25], very few techniques have been used to process Mg alloy tubes [26-28]. Unfortunately, low temperature processing and texture evolution have not yet been studied for SPD of Mg alloy tubes, which are significant for these alloys as low

temperature reduces the possibility of softening due to recrystallization and the starting texture influences the ability to process the material. Therefore, the present study aims at investigating the effect of both texture and temperature on tECAE processing.

Another material investigated in this research is Nb tube. Niobium has wide application in charged particle accelerators because of its superconducting properties. Non-uniform and large grain size, and inconsistent mechanical properties are major challenges associated with Nb. Therefore, this work has explored the potential of tECAE to process Nb tubes suitable for subsequent hydroforming to form superconducting radiofrequency (SRF) cavities for particle accelerators.

1.2 Objective

The objectives of the present work are motivated by the problems and lack of knowledge in fabrication and understanding of tubular forms of Mg alloys and pure Nb as explained in the previous section. The objectives of this study are:

1. To test the hypothesis that high-shear, lower temperature thermomechanical conditions inherent to the tube equal channel angular extrusion processing will enable the formation of fine-grained microstructure in AZ31 magnesium alloy tubes, enhancing the mechanical properties and concomitantly, develop novel textures not possible through conventional processing routes.
2. To develop an improved understanding of the role of temperature and initial texture in severe plastic deformation processing of Mg alloys.
3. To examine the scale-up capability of ECAE processing and understand the effects of hybrid ECAE plus tECAE processing on AZ31 alloy. This will be

achieved by ECAE processing AZ31 bars having dimensions 50 x 50 x 250 mm^3 via route 4A and $4B_C$, and subsequently cutting tubes from different orientations followed by tECAE processing.

4. To develop a viscoplastic self-consistent (VPSC) crystal plasticity model for predicting and analyzing the texture evolution during the novel tECAE processing of AZ31 alloy.
5. Develop a fundamental understanding of failure mechanisms of AZ31 tubes both commercially produced and tECAE processed.
6. To test the hypothesis that tECAE processing will lead to formation of seamless, and fine grained pure Nb tube with improved isotropic mechanical properties in the as-worked and recrystallized conditions.

1.3 Dissertation organization

A systematic approach involving experiments and modeling was taken to meet the above-mentioned objectives and is reported in the following chapters:

Chapter I provides the introduction and background for this work. The general background about Mg alloys is provided specifically highlighting the synergy between the deformation mechanisms, texture, grain size and mechanical properties. A brief introduction about pure niobium and the challenges faced involving its application in superconductive radio frequency cavities is also presented. Lastly, the chapter presents a general overview about severe plastic deformation processing and discusses the current state of research in tube processing.

Chapter II gives information about the experiments conducted and explains the model used for texture simulation. In Chapter III, a detailed analysis of one pass tECAE processing of AZ31 at temperatures as low as 120 °C is discussed combined with VPSC predicted texture results. Chapter IV investigates the role of different starting textures in tECAE processing. Additionally, the failure mechanisms of Mg alloys during tensile tests are also discussed. Chapter V presents the hybrid ECAE plus tECAE processing approach, involving the scale-up use of ECAE. Chapter VI investigates tECAE processing of niobium and discusses its recrystallization behavior post SPD processing. Chapter VII presents the main conclusions from these studies along with suggestions for future work.

1.4 Background and Literature review

1.4.1 Magnesium alloys

Mg offers a unique combination of lightweight and biocompatibility. The low density of magnesium (1.74 g/cm^3) makes it significantly lighter than aluminum, steel and titanium that are the most commonly used structural and bio-implant materials [29-31]. Cast Mg alloys have been widely used for decades due to their inherently low melting temperature (650 °C), good fluidity, and low susceptibility to hydrogen porosity [32]. However, the cast structures have big grains and modest mechanical properties, hence, with the advancement of materials processing techniques, a growing interest in the development of wrought Mg alloys is observed [33].

In the recent times, significant efforts have been made for conservation of energy, reduction in emissions and improvement in fuel economy in the transportation

sector, which presents a pressing need to develop lightweight automobiles [34], creating a renewed interest in Mg alloys due to its low density and high strength to weight ratio. Mg also has the potential to be used in the biomedical industry as biodegradable implant material for coronary stents [35], and orthopedic applications as its physical and mechanical properties (density, elastic modulus, compressive yield strength, and fracture toughness) are comparable to natural bone, and thus reduces stress shielding [36]. Mg is an important component of the human body and is metabolized. It is also found in human bone tissue, hence its degradation products are less harmful to the body than its ceramic, metallic and polymer counterparts [35-37]. Tubular forms of Mg alloys are showing much promise in being used as bioabsorbable stents [7].

Even though Mg alloys provide the above-mentioned benefits, its widespread use is limited in the industries because of the following reasons:

a) The low strength, low ductility, and limited formability of Mg at ambient temperatures, make it difficult to use in the transportation industries where most of the component forming operations are performed at room temperature.

b) Wrought Mg alloys develop undesirable texture during processing which further limits its formability.

c) Mg shows low corrosion resistance, hence limiting its use in all industries where exposure to moisture is common.

The promising benefits of using Mg alloys has led to much research and development to improve its properties. Mg alloys' properties can be tailored in various

ways, the most common being addition of alloying elements, and developing thermomechanical processes to refine grains and control texture.

Generally, pure metals do not have enough strength to be used for structural applications. Alloying elements are then added to improve the mechanical properties either by solid solution strengthening, precipitation hardening or by dispersion strengthening [38]. Rare earth elements are now being used as alloying elements for Mg because they have relatively higher solubility and provides precipitation hardening. Significant improvements in the mechanical properties are the result [39, 40]. Additionally, rare earth elements may activate non-basal slip activity and weaken basal texture [41]. However, the high price of rare earth elements has caused hindrance in its use. Mg alloys without rare earth additions have limited strength for structural applications.

1.4.1.1 Magnesium alloy formability

Magnesium has a hexagonal close-packed (hcp) structure as shown in Figure 1.1 [42]. All the possible slip and twinning systems active in hcp materials are shown in Figure 1.1. Mg's limited formability is attributed to the fact that it has only one close-packed plane i.e. the basal plane (0001). Slip on the basal plane follows the Schmid law [43], hence, slip occurs when the applied stress on the slip plane and along the slip direction attains a critical value known as the critical resolved shear stress (CRSS).

The CRSS for basal $< a >$ slip is the lowest among all the other possible slip systems in Mg and is independent of temperature, therefore it is the most easily activated (soft) slip system [44]. However, the basal plane has only two independent $< 11\bar{2}0 >$

co-planar slip directions, hence the basal slip system cannot accommodate deformation along c-axis [45, 46].

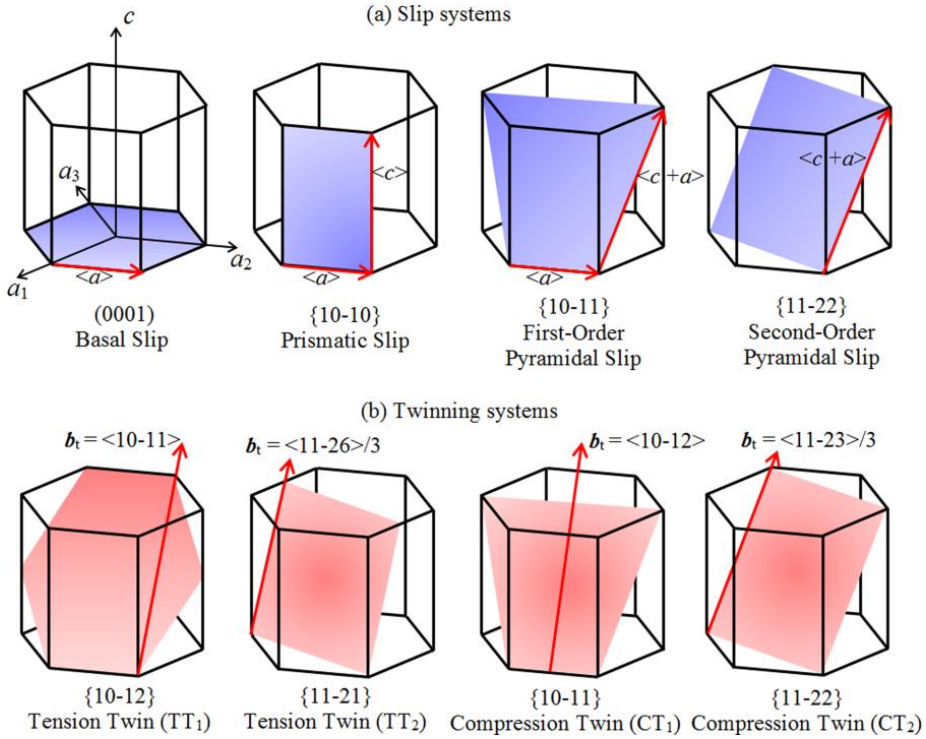

Figure 1.1 Schematic of HCP unit cell with all the possible slip and twinning systems [42].

For a polycrystalline material to undergo uniform deformation, five independent slip systems are required as the per Von Mises [47] or Taylor criteria [48]. Since Mg does show limited elongation to failure, it must have other slip systems that facilitate the deformation. Prismatic $< a >$ slip system provides two more independent slip system, but it cannot accommodate c-axis deformation. Pyramidal I $< a >$ and pyramidal II $< c + a >$ are the other slip systems present in Mg alloys, out of which the pyramidal I $< a >$ is not completely independent and can be presented as a combination of basal and

prismatic slip system. Activation of the pyramidal II $< c + a >$ slip system is required for uniform deformation [49]. However, CRSS values of the hard prismatic and pyramidal II slip systems depend on temperature and are very high at room temperature, therefore, they are difficult to activate [50]. A few studies [46, 51, 52] did show activation of prismatic $< a >$ and pyramidal II $< c + a >$ slip along with basal slip system at room temperature, but such deformation was restricted to the grain boundaries. So, activation of hard deformation modes is possible at room temperature but not homogenously in the material. Hence, Magnesium's formability is low at room temperature whereas at temperatures greater than 180 °C, Mg shows good formability due to activation of non-basal, pyramidal $< c + a >$ slip which accommodates the deformation [45]. From the above discussion, it is clear that uniform deformation of Mg at room temperature by the slip mechanism is difficult, hence, deformation twinning modes may assist in deformation.

The twinning mode that accommodates c-axis extension is called extension twinning $(10\bar{1}2)$, whereas the one that may accommodate c-axis contraction is called contraction twinning $(10\bar{1}1)$ and $(10\bar{1}3)$. Thus, twinning deformations are polar in nature [53, 54]. The CRSS value for extension twinning is lower than that of non-basal slip at room temperature, and it competes with any non-basal slip that has a component of Burger vector along c-axis. Although extension twinning may accommodate c-axis of its deformation, it can only sustain strain upto 6.5% and is accompanied by texture change and crack formation in the material [45]. Extension twinning has a detrimental effect on formability, and it is better to suppress activation of extension twins.

Contraction twins are hard to activate because their CRSS is high. They also lead to crack formation in the material. In many cases, double twinning can be observed which is the formation of extension twins inside contraction twins. This often leads to failure of the material as basal slip activity can be observed in these double twins due to the preferred grain orientation. This results in inhomogeneous strain distribution, and failure of the material [25, 49, 54].

The formability of Mg alloys is also influenced by dynamic recrystallization (DRX). The kinetics of this depend on temperature, strain rate, and starting grain size. DRX is active at elevated temperatures influencing the microstructure and texture while, at low temperatures DRX activity is not uniform which may form local soft DRX grains leading to void formation and fracture of the material from that region due to strain incompatibility. The non-basal planes typically have high stacking fault energy and cause continuous DRX (CDRX) in which accumulation of low angle grain boundaries due to applied strain leads to formation of high angle grain boundaries [25, 55].

Lastly, the Hall-Petch relation [56] is applicable in Mg alloys but the effect of texture along with grain size is important for understanding the mechanical behavior. Figure 1.2 shows the relation between grain size and various mechanical property parameters (yield strength (YS), ultimate tensile strength (UTS), and % elongation) of AZ31 alloys having undergone different metal forming processing routes explained in ref. [24]. Unlike the face centered cubic (fcc) and body centered cubic (bcc) systems, no clear correlation can be found in mechanical properties and grain size of Mg alloys. Such

a result is obtained because difference in texture plays a significant role in the mechanical properties variations.

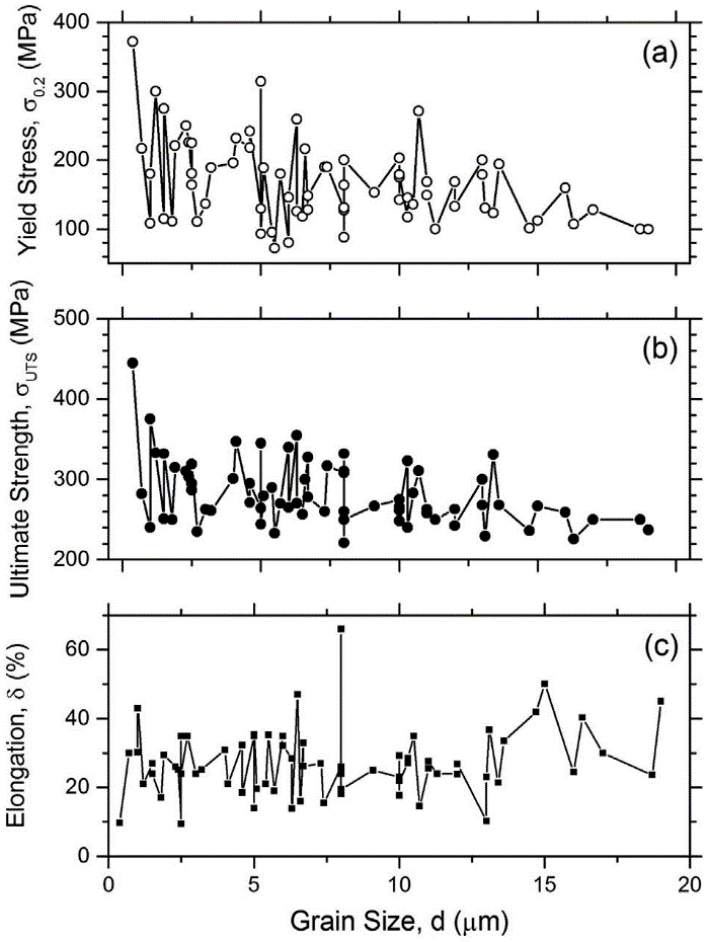

Figure 1.2 Effect of grain size on yield strength, ultimate tensile strength, and elongation during tension testing of AZ31 alloys [24]. Each alloy is processed via different SPD route.

1.4.2 Niobium

Superconducting radio frequency (SRF) cavities are a key component of charged particle accelerators providing energy to the particles by utilizing a carefully controlled

radio frequency electric field. The most widely used material for SRF cavities is high purity (RRR grade) niobium (Nb). The as-cast pure Nb is made via electron beam remelting with slow cooling which allows for the evaporation of most of the impurities except tantalum as it has a low vapor pressure. A drawback of slow cooling is that it leads to the formation of large grains in the as-cast material which impart inhomogeneous properties [57].

The conventional fabrication technique for SRF cavities involves the electron beam welding of two deep drawn half cells. This leads to the formation of welding seams, resulting in microstructural changes near the weld which, in turn, may cause residual resistance ratio (RRR) degradation [57-59]. Modification in welding parameters, better quality control, and improvement in subsequent electropolishing techniques have resulted in closing the gap between the theoretical field limits and the obtained field values [60]. However, increased interest in the fabrication of seamless tubes has been seen in the past, as seamless tubes give an opportunity to simultaneously avoid the irregularities caused by welds and reduce the cost of fabrication. Some of the earlier efforts made to produce seamless Nb tubes involve spinning [4, 61, 62] and hydroforming [9]. One of the major problems in using these techniques is the existence of batch to batch variations making it hard to predict the mechanical response and structural homogeneity of the tubes, which lead to taking time consuming corrective measures. Additionally, inhomogeneous deformation may occur due to non-uniform initial microstructure.

To address the challenges involved in fabrication of Nb tubes for SRF cavity, it is important to understand the formability characteristics of Nb. The deformation behavior of any metal depends on its crystal structure, crystallographic texture, presence of secondary particles, temperature, and strain rate. Niobium's crystal structure, active slip systems, prevalent deformation textures and their role in formability are discussed here.

Nb has a body centered cubic (BCC) crystal structure and a high melting point of 2469 °C. It behaves as a Type II superconductor with a T_c of 9.46 K [63]. A BCC material has 48 distinct slip systems: two $< 111 >$ slip directions on six $\{110\}$ slip planes each, and four $< 111 >$ slip directions on 12 $\{112\}$ and 24 $\{123\}$ slip planes. Therefore, the possible slip systems active in Nb are $\{110\} < 111 >, \{112\} < 111 >$, and $\{123\} < 111 >$.

Nb has the lowest spring constant (most compliant) among all the BCC metals, with $< 111 >$ being the most compliant direction [64]. Texture and grain size play a crucial role in the deformation processing of Nb. Since the as-cast material has extremely large grains, it is difficult to achieve the desired properties for tube fabrication, hence deformation processes are used to refine the grain size. Rolling of Nb into plate and sheet is the conventional process of grain refinement and material shape change. The grain orientation after such processing in Nb generally varies from the surface to the interior of the material. The applied strain leads to grain orientations such that the majority of the $\{100\}$ planes are parallel to the sheet normal direction (ND) on the sheet surface (rotated cube texture). In contrast, in the interior, the $\{111\}$ planes are often parallel to the sheet ND (γ-fiber texture). This texture difference between the

interior and the surface leads to varied and non-uniform mechanical properties [57]. Additionally, the accumulated strain after deformation processing can reduce the cavity performance due to the presence of high dislocation density, hence subsequent heat treatment is done to remove these dislocations. The rolling process also interferes with the repeatability of the properties as grains orient in an unpredictable manner after recrystallization heat treatment. Batch to batch variations are observed. Additionally, producing a uniform fine-grained recrystallized microstructure is challenging after conventional thermo-mechanical processing as these processes are unable to adequately break-down the initial as-cast structure [65].

It has been reported that rolling to greater than 70% reduction (high strain) in thickness leads to an increased fraction of the desired {111}||ND orientations by slip on {123} planes. Application of such an amount of strain during rolling, reduces the size of the material and hence further application of strain becomes difficult. A limitation in texture development and modification is the result. The consequence of a non-uniform recrystallized grain size and texture variations is difficulty in obtaining optimum performance from the SRF cavity.

Severe plastic deformation (SPD) is an effective technique to overcome the challenge of limited accumulated strain and formation of ultrafine-grained material. Equal channel angular extrusion (ECAE), an SPD technique, has been used in the past to process bars and plate forms of various metals including Nb. It has been shown by Balachandran et. al. [66] that fine-grain recrystallized microstructures can improve the performance of SRF cavities. Therefore, the SPD process of tECAE is used in this study

for Nb tube deformation. tECAE applies axisymmetric strain in the material, hence, forming a seamless tube with ultrafine grain structure. This study aims at evaluating various processing routes to produce tubes having uniform recrystallized microstructure, favorable texture, and desired mechanical properties suitable for hydroforming.

1.4.3 Current state of research in tube fabrication

Material microstructure such as grain size significantly influences mechanical, physical, and chemical properties. Specifically, the strength of the material is related to its grain size as per the Hall-Petch relation [56], and it follows from this relation that a reduction in grain size imparts higher strength to the material. Such an increase in strength with reduction in grain size is a result of increased grain boundaries inhibiting dislocation motion. Therefore, several metal forming techniques have been developed to convert a coarse-grained material to a fine-grained material. The conventional forming methods such as rolling, forging, and extrusion provide limited grain refinement due to the limitation in total strain that can be imposed before the material's cross-section becomes too small to process further.

To achieve ultrafine grains (UFG), grain size in the range of 100 nm to 1 μm, severe plastic deformation (SPD) techniques are used where extremely high strains are imposed on the material either in one step or multiple steps [67]. It is a metal forming process that applies high plastic strain leading to microstructural refinement in bulk material which in turn improves the strength and provides reasonable ductility. Additionally, SPD processing introduces a high dislocation density in the material, hence, leading to further increase in strength. The ability of such processing to improve

and alter the strength and properties of materials has led to development of several new SPD processes including equal channel angular extrusion [10, 11, 68] (ECAE, also known as equal channel angular processing or ECAP), high pressure torsion (HPT) [69], accumulative roll-bonding (ARB) [70], cyclic extrusion compression (CEC) [71] to name a few. These SPD studies have been conducted on plates, sheets, and bars of various alloys. However, studies on enhancing the mechanical performance and understanding the role of texture in tubular forms of materials using SPD remain scarce in the literature.

Initial attempts were made in 2006 to utilize conventional ECAP for processing tubes using a flexible mandrel to prevent buckling of the tube. Nagasekhar et. al. [14], ECAP processed titanium grade-1 tube by using an ECAP tool with deformation angle of 150° and sand filling as a flexible mandrel to prevent the buckling of the tube during processing as shown in Figure 1.3. Using the same tool, Valder et. al. [15] in 2012, ECAP processed Aluminum tubes. In both of these processing approaches, limited grain refinement and limited improvement in mechanical properties were observed.

Djavanrodi et. al. [16] in 2013 utilized a polyurethane rubber mandrel to ECAP process Cu tube. Jafalour et. al. [72] in 2016 used hydraulic oil as a flexible mandrel to in a 120° deformation angle ECAP tool to process 6061 Al alloy. In all these tube processing approaches using an ECAP tool, several problems occurred: (1) non-uniform tube thickness (2) non-uniform circumferential deformation occurs in the tube, hence axisymmetric properties was not achieved. 3) Lower hydrostatic stress makes ECAP less effective in processing tubular materials. 4) A non-uniform heterogenous hardness

distribution was observed through the cross section 5) Using oil as a mandrel can cause sealing difficulties.

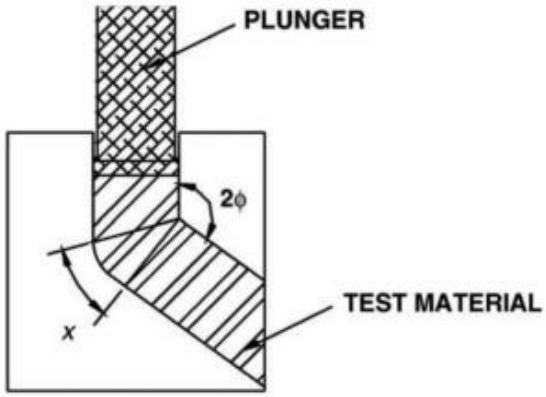

Figure 1.3 Schematic of ECAP for processing tubular material. Sand used as mandrel [15].

Toth et. al. [73] and Wang et. al. [74] developed a high-pressure tube twisting and a tube high pressure shearing process based on the HPT technique to process tubular forms of metals. The shortcomings of these methods include non-uniform strain distribution, through material thickness variations, and limited scale-up capability. Another SPD processing technique developed was tubular channel angular pressing (TCAP) [75]. In this approach, inhomogeneous strain is applied during the processing due to the tool design. One more technique was developed by Faraji et. al. [76] called parallel tubular channel angular pressing (PTCAP). This tool design is similar to the tool used in the present study, but unfortunately, not much work was done on low

temperature processing of Mg alloys, texture evolution, and no work was done on Nb processing using the PTCAP tool.

CHAPTER II

EXPERIMENTAL METHODS AND SIMULATIONS*

2.1 Introduction

In this study, bulk severe plastic deformation (SPD) processing was conducted on bar and tubular forms of materials. The process of equal channel angular extrusion (ECAE) and tube equal channel angular extrusion (tECAE) are described and explained in this chapter. Two materials that are SPD processed in this research are AZ31 Mg alloy (nominal composition: 3% Aluminum, 1% Zinc, 0.20% Manganese, and the rest Magnesium) and commercially pure reactor grade niobium (99.7% Nb). SPD processing results in a change in crystallographic texture. Specifically, Mg alloys having hcp structure, are anisotropic, and hence, understanding its deformation mechanisms by analysis with a crystal plasticity model is important. Therefore, along with the experimental work, modeling and simulation are utilized. This chapter explains the model used in the research.

2.2 Equal channel angular extrusion (ECAE)

Equal channel angular extrusion is one of the most effective and versatile SPD techniques used for material processing. It was developed by Segal in the 1970s in the

---

*Portions of this chapter reprinted with permission from "Tube equal channel angular extrusion" by A. Srivastava, M.W. Vaughan, B. Mansoor, W. Nasim, R.E. Barber, I. Karaman, K.T. Hartwig. Materials Science and Engineering: A 814 (2021), 141236

former Soviet Union. During ECAE processing, a thin region of material undergoes simple shear at the intersection of two channels of equal cross-section, resulting in microstructural break up and grain refinement [10, 11, 68]. The two channels form an angle φ at the intersection. A schematic of an ECAE tool with φ = 90° as die angle (deformation angle) is shown in Figure 2.1. Few tool designs have a curvature near the outside region at the intersection of two channels. This is referred to as corner angle or fan angle (The fan angle is 0° in Figure 2.1) and is denoted as ω in this text. It has been observed that presence of a non-zero fan angle reduces the shear applied on the workpiece [77]. The material to be processed (workpiece) could be in the form of bar, billet, or plate [19-21, 78-83]. The workpiece is inserted into the upper channel and pressed through the die into the lower channel using a punch. The material undergoes shear deformation at the intersection of the two channels. As both channels are of equal cross section, the initial and final area of cross-section of the workpiece remains nearly the same, hence, multiple passes can be performed which enables a large amount of total accumulated strain. The result can be a homogenous and uniform ultra-fine grain size.

The effective strain imposed on the material is a function of die angle φ and the fan angle ω. The relationship is shown in Eq. 2.1 [84].

$$\varepsilon_{ECAE} = N\left(\frac{1}{\sqrt{3}}\left(2\cot\left(\frac{\varphi}{2}+\frac{\omega}{2}\right)+\omega cosec\left(\frac{\varphi}{2}+\frac{\omega}{2}\right)\right)\right) \quad (2.1)$$

where, φ is the deformation angle and ω is the fan angle, which is equal to 0° in the schematic shown. N is the number of passes.

For a 90° tool, an effective strain of 1.15 is applied on the workpiece per pass. If the same bar is extruded for multiple passes, the total strain accumulates.

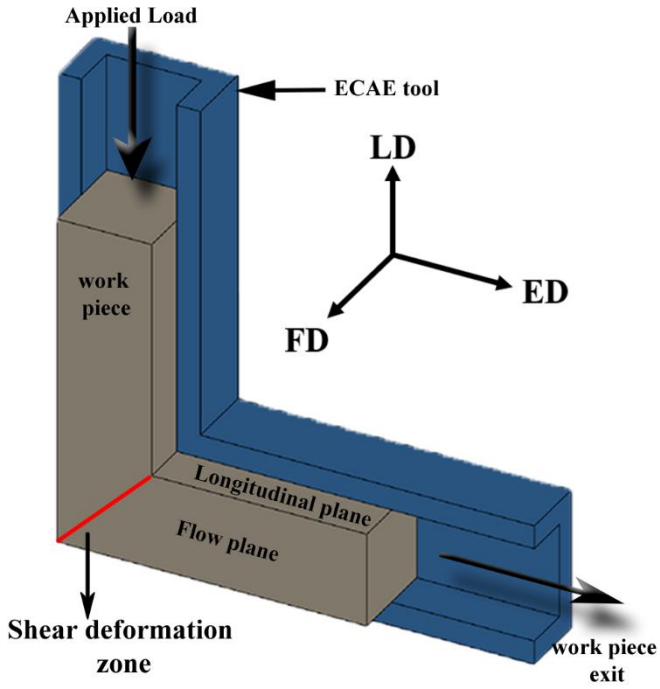

Figure 2.1 ECAE tool schematic. LD, ED, and FD are the longitudinal direction, extrusion direction, and flow direction, respectively [85].

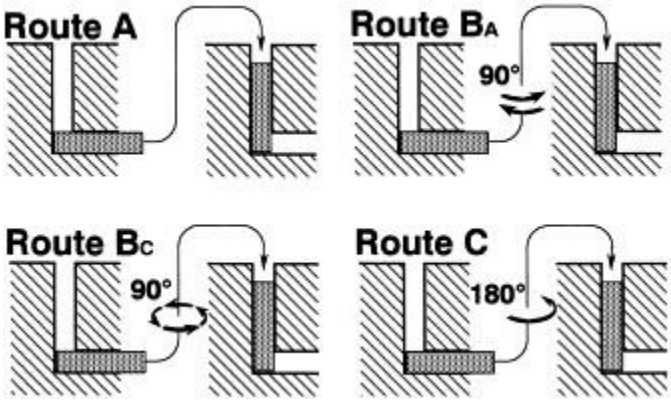

Figure 2.2 Schematic of different ECAE routes. Route B is also known as route B_A. Note that route E is a hybrid route, therefore it is not shown separately in the schematic [86].

The multiple passes in ECAE can be performed by rotating the bars in between each pass leading to formation of different routes of ECAE processing [10]. These routes are based on the change in shear plane orientation with respect to the original orientation of the bar, resulting in development of different microstructure, grain morphology, and texture. The important ECAE routes are shown in Figure 2.2 and explained as follows:

Route A: Orientation of the bar remains the same throughout all passes. This processing results in formation of elongated and laminar grains.

Route B: Rotation of 90° for even numbered passes and 270° for odd numbered passes. This forms a fibrous microstructure.

Route Bc: Rotation of 90° in the same direction (clockwise or anti-clockwise) between each pass. This results in formation of an equiaxed microstructure.

Route C: Rotation of 180° between each pass. Strain reversal occurs in this route. The material element deforms in odd numbered passes and is restored in even number of passes. The microstructure consists of equiaxed grains after even number of passes.

Route E: Rotation of 180° for all even numbered passes and by 90° (either clockwise or anti-clockwise) for the odd number of passes. This is a hybrid route which is based on route C with a rotation of 90° at each even numbered of pass. During route C, deformation occurs along one plane, with an added 90° rotation, the deformation occurs on 2 planes and the material element still reverts to its original shape. The microstructure for this route is more equiaxed compared to route C.

Various parameters are needed to be optimized to best process different kinds of material via ECAE. Some difficult to work with materials that have low ductility can be

ECAE processed by increasing the die angle, reducing the extrusion speed, increasing the processing temperature, or applying back pressure [11].

2.3 Tube equal channel angular extrusion (tECAE)

Based on the ECAE process, the tECAE process is developed to process tubular forms of material. The tECAE process is conducted in two passes (steps) in which a tubular workpiece undergoes a shear expansion step followed by a shear contraction step. This combined expansion and contraction ensures that the tube's dimensions remain unchanged after processing, thus allowing for further multi-pass processing. A schematic of tECAE tool is shown in Figure 2.3 and consists of the following components: a top die (dark blue), a bottom die (light blue), and a mandrel (gray). The workpiece is placed in a cavity in the top die; a hollow punch is used to push it through the channel into the bottom die. Heating bands are used to achieve the appropriate processing temperature (not shown in Figure 2.3). The tool is mounted on a platform, where a hydraulic press is used to push the hollow punch.

During each step, the workpiece passes through two deformation zones, hence after one complete tECAE processing (2 steps), the material passes through a total of four shear deformation zones. During the first pass, (expansion step) the tube passes through the deformation zones 1 and 2. A small copper ring, 6 mm long, is placed between the workpiece and the hollow punch. The onset of deformation of the copper tube marks the completion of one pass. This protects the hollow punch from deforming in each pass enabling it to be re-used. After the expansion pass, the expanded tube undergoes the second pass (contraction step) in another die shown in Figure 2.3. During the second pass,

the tube passes through the deformation zones 3 and 4 enabling the tube diameter to contract back to its original dimensions. The finished tube is deformed symmetrically, via axisymmetric circumferential uniform strain [17], in addition to the shear strain. This type of axisymmetric uniform strain cannot be developed via conventional ECAE processing, where the cross-sectional area is conserved in each pass. After complete extrusion, the deformed tubular workpiece is removed from the bottom die. The axis notation used in tECAE processing is shown in Figure 2.4(b), where TD represents the tangential direction, RD represents the radial direction, and tED represents the tECAE processing direction.

The angle of deformation in zone 1 is φ_1, which is equivalent to the first pass of deformation of a bar in conventional ECAE [10]. Deformation zone 2 in tECAE is at an angle φ_2, which is equivalent to rotating the bar by 180° after the first pass in conventional ECAE and processing it again, which is essentially route 2C in conventional ECAE nomenclature [10].

In each pass, the sum of the simple shear strains in the two deformation zones and the circumferential strain for the expansion (or contraction) pass of tECAE gives the accumulated plastic strain per pass. Eqs. 2.2-2.4 are used to calculate the accumulated shear strain per pass. More details about the tool can be found in refs. [17, 85].

$$\varepsilon_{tECAE} = \varepsilon_{Simple\ shear} + \varepsilon_{\theta} \tag{2.2}$$

$$\varepsilon_{tECAE} = \sum_{i=1}^{2} \frac{1}{\sqrt{3}} \left(2\cot\left(\frac{\varphi_i}{2} + \frac{\omega_i}{2}\right) + \omega cosec\left(\frac{\varphi_i}{2} + \frac{\omega_i}{2}\right)\right) + \frac{2}{\sqrt{3}} \ln \frac{D_2}{D_1} \tag{2.3}$$

$$\varepsilon_{Simple\ shear} = \sum_{i=1}^{2} \frac{1}{\sqrt{3}} \left(2\cot\left(\frac{\varphi_i}{2} + \frac{\omega_i}{2}\right) + \omega cosec\left(\frac{\varphi_i}{2} + \frac{\omega_i}{2}\right)\right) \tag{2.4}$$

$$\varepsilon_{\theta} = \frac{2}{\sqrt{3}} \ln \frac{D_2}{D_1} ; \varepsilon_{circumferential\ strain} = \ln \frac{D_2}{D_1}$$

where φ_i $(i = 1,2)$ is the deformation angle equal to 135° in this study, D_1 is the inner diameter of the tube before each pass (equal to 32 mm in this study), and D_2 is the inner diameter of the tube after each tECAE processing pass (38 mm here). ω_i is the fan angle (corner angle) which in theory is equal to 0° by tool design.

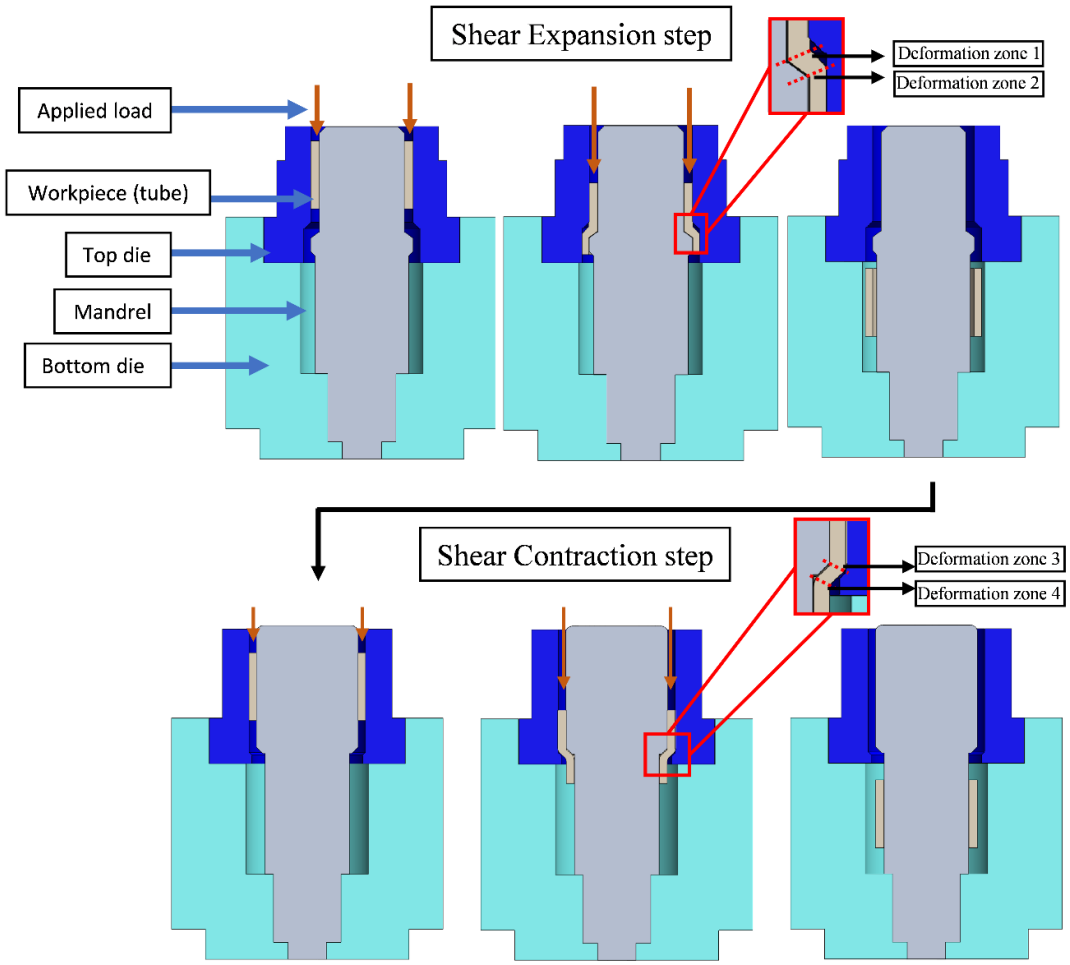

Figure 2.3 Schematic of the tube equal channel angular extrusion (tECAE) process. The shear expansion step shows the first pass whereas the shear contraction step shows the second pass.

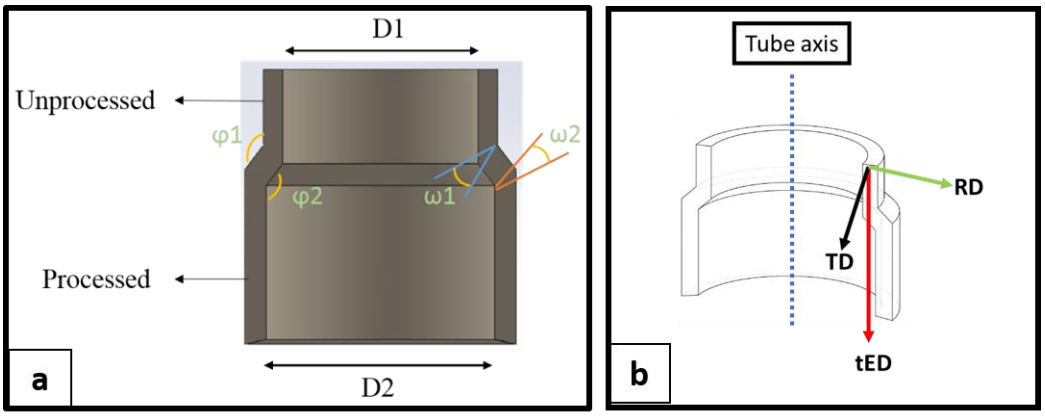

Figure 2.4 Tube cross-section during the expansion pass of tECAE showing deformation angles (ϕ1, ϕ2) and fan angles (ω1, ω2). (b) The axes notation used for the tube are shown. RD is the radial direction, TD is the tangential direction, and tED is the tECAE direction[85].

The cylindrical die used in this study has an inner diameter of 3.81 cm, while the mandrel's diameter is 3.18 cm. The accumulated strain calculated from Eqs. 2.2-2.4 is 1.16 per pass. Although, after considering the material flow, the obtained φ_1 and φ_2 values were 141° and 135° respectively, whereas fan angle ω_1 and ω_2 were 30° and 22° respectively, which resulted in a accumulated strain of 1.05 per pass.

A tECAE tool having smaller deformation angles (say 90°) would give a higher total accumulated strain per pass. Figure 2.5 shows the calculated total plastic strain accumulated per pass for tools with different deformation angles and varying fan angles. Note that, for the tools having smaller tool deformation angles, close to 90°, the change in the fan angle has a significant effect on the total strain per pass. This effect decreases as the deformation angle increases.

2.4 Viscoplastic self-consistent crystal plasticity modeling and simulation

The ECAE and tECAE processed materials develop textures different from the starting condition. In the present study, the experimentally measured texture evolution results after the tECAE process are supplemented with viscoplastic self-consistent (VPSC) crystal plasticity model that has been effective in texture predictions and analyzing flow response of non-cubic metals [25, 87]. While the details of the model can be found in the refs. [25, 87-89], a brief introduction to the model is presented here.

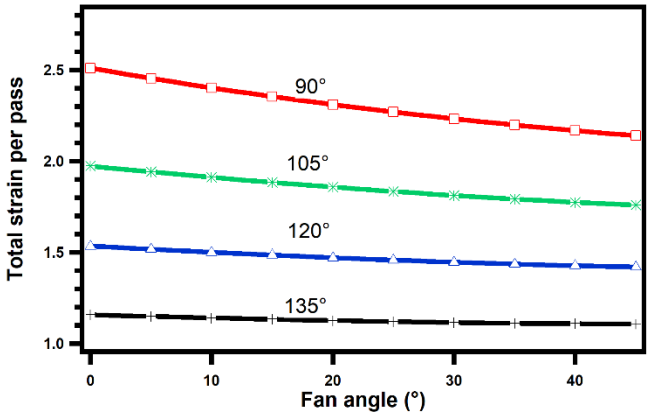

Figure 2.5 Total strain per pass vs. fan angle (ω) for different die angles (φ). As the angle of deformation is increased, the total strain per pass decreases and the effect of fan angle on total strain per pass also decreases.

Many crystal plasticity models have been used for texture simulation that works on the basis of interaction of each grain with its surrounding, such as relaxed constraints [90], full constraint [48, 91], and rate-sensitive crystal plasticity [92] model which works well for cubic materials. For non-cubic (e.g. hexagonal) materials, the limited slip systems and role of twinning increases the complexity in the model. The VPSC model

works well for non-cubic metals. It considers grains to be ellipsoidal shaped viscoplastic inclusions that are embedded in a homogenous effective medium. For texture, the grains having same orientations are represented by their volume fraction in the polycrystalline aggregate, resulting in discrete texture that is comparable to the experimentally measured continuous texture.

2.4.1. VPSC model for tECAE processing

In the present study, the VPSC model is used for texture evolution and analysis of active deformation modes during tECAE processing. Among the possible active deformation modes, three slip systems, namely, basal, prismatic, and pyramidal and two twining systems, namely, extension and contraction twins are considered. For the individual deformation mechanisms, the evolution of threshold stress (τ^s) is associated with the accumulated shear strain (Γ), defined by the Voce hardening law as:

$$\tau^s = \tau_0^s + (\tau_1^s + \theta_1^s \Gamma)\left\{1 - exp\left(\frac{\theta_0^s \Gamma}{\tau_1^s}\right)\right\} \qquad (2.5)$$

where τ_0^s is the critical resolved shear stress (CRSS), τ_1^s the back-extrapolated threshold stress, θ_0^s is the initial hardening rate, and θ_1^s the latent hardening parameter for deformation system s.

The Voce hardening parameters for the Voce hardening law were obtained by using an optimization tool for simulating tensile stress-strain responses along the three orthonormal directions of the AZ31 pre-tECAE hot-rolled plate (the plate was heat-treated at 350 °C for 12 hours under vacuum and then water-quenched) at different temperatures. Details regarding the determination of these parameters and tensile stress-strain responses are given in Ref. [25]. Table 2.1 depicts the voce hardening parameter values used.

The Predominant Twin Reorientation (PTR) scheme [88] is implemented to account for the reorientation of grains due to twinning. In this scheme, at each deformation step, the reorientation of a grain by twinning is assessed by comparing the accumulated twin volume (V^{accu}) in each grain with a threshold value (V^{th}). If the accumulated twin volume exceeds the threshold value, grain reorientation occurs, and the volume of the reoriented grain is added to the effective twin volume fraction (V^{eff}). Eq. 2.6 shows the relation used in the PTR scheme.

$$V^{th} = A_1 + A_2\left(\frac{V^{eff}}{V^{accu}}\right) \qquad (2.6)$$

where A_1 and A_2 are constants set to 0.1 and 0.4 respectively in the present study. Further details about the PTR scheme can be found in refs. [25, 88, 93].

The tubes undergo two passes (expansion and contraction) of tECAE. The strain acting on the tubes in each pass comprises of two parts - simple shear strain from the conventional ECAE simple shear model and the circumferential strain that accounts for changes in wall thickness and length of the tube. Although the changes in tube thickness take place in-between odd and even deformation zones, it is assumed that such dimensional change are accounted for after even (2,4) deformation zones for the purposed calculations. Hence, Eq. 2.8 is used to determine the strain rate after deformation zones 1 and 3 whereas Eq. 2.9 is used after zones 2 and 4. Δt, the time required for one pass is given by Eq. 2.7 [77].

$$\Delta t = W\omega/\sqrt{2}V \qquad (2.7)$$

$$\dot{\gamma_{1,3}} = \left(\varepsilon_{simple\ shear}/\ \Delta t\right) \qquad (2.8)$$

$$\dot{\gamma_{2,4}} = (\varepsilon_{tECAE}/\Delta t) \qquad (2.9)$$

where Δt is the time required for one pass, W is the width of the tube, V is the extrusion speed and ω is the fan (corner) angle.

For the deformation zone 2 calculations, the strain rate was calculated using equation $\dot{\gamma_2} = (\varepsilon_{tECAE}/\Delta t)$. The velocity gradient tensor in the global coordinate system for deformation zone 1 (L_1) and for deformation zone 2 (L_2) are given by Eq. 2.10 and 2.11, respectively:

$$L_1 = \begin{pmatrix} cos\theta sin\theta\dot{\gamma_{1,3}} & -cos^2\theta\dot{\gamma_{1,3}} & 0 \\ sin^2\theta\dot{\gamma_{1,3}} & -cos\theta sin\theta\dot{\gamma_{1,3}} & 0 \\ 0 & 0 & 0 \end{pmatrix} \qquad (2.10)$$

$$L_2 = \begin{pmatrix} (cos\theta sin\theta + \ln\frac{D_2}{D_1})\dot{\gamma_{2,4}} & cos^2\theta\dot{\gamma_{2,4}} & 0 \\ -sin^2\theta\dot{\gamma_{2,4}} & -(cos\theta sin\theta + \frac{\Delta h}{h})\dot{\gamma_{2,4}} & 0 \\ 0 & 0 & 0 \end{pmatrix} \qquad (2.11)$$

After completion of first pass, the tube is further processed for a second pass (contraction step). Although the deformation angle during the second pass is the same as the first pass, the shear direction is opposite, so the velocity gradient tensor for the different deformation zones (deformation zone 3 and 4) of the second pass are given by Eq. 2.12 and 2.13, respectively:

$$L_3 = \begin{pmatrix} cos\theta sin\theta\dot{\gamma_{1,3}} & cos^2\theta\dot{\gamma_{1,3}} & 0 \\ -sin^2\theta\dot{\gamma_{1,3}} & -cos\theta sin\theta\dot{\gamma_{1,3}} & 0 \\ 0 & 0 & 0 \end{pmatrix} \qquad (2.12)$$

$$L_4 = \begin{pmatrix} (cos\theta sin\theta + \ln\frac{D_1}{D_2})\dot{\gamma_{2,4}} & -cos^2\theta\dot{\gamma_{2,4}} & 0 \\ sin^2\theta\dot{\gamma_{2,4}} & -(cos\theta sin\theta + \frac{\Delta h}{h})\dot{\gamma_{2,4}} & 0 \\ 0 & 0 & 0 \end{pmatrix} \qquad (2.13)$$

where θ = (90° - φ /2), φ= 135°, h_1 is the initial length of the tube = 25 mm, h_2 is the length of the tube after one pass = 23 mm, and Δh is the change in the length of the tube. In this study, the initial texture measured via x-ray diffraction (XRD) was converted into a weight file, as required for the VPSC model. The starting texture was discretized into ~335 orientations (i.e. grains) to be used as input for the model.

Table 2.1 Voce hardening parameters obtained by simulating the tensile stress-strain responses along three orthonormal directions of the pre-tECAE hot rolled plate at different temperatures using an optimization tool.

	τ_0 (MPa)			**τ_1 (MPa)**		
	120 °C	175 °C	200 °C	120 °C	175 °C	200 °C
Basal	23.2	17.5	14	5.51	10.5	14.5
Prismatic	110.4	88.9	82.4	21.2	24.3	40
Pyramidal <c+a>	170.5	76.8	62.5	93.9	85.3	9.4
Extension twinning	52.8	74.4	99.3	0	0	0.1
Contraction twinning	130	121	110	62.4	64.1	83.2
	θ_0 (MPa)			**θ_1 (MPa)**		
	120 °C	175 °C	200 °C	120 °C	175 °C	200 °C
Basal	3718	655.4	347.6	33.72	1.65	0.15
Prismatic	532.3	175.5	0.8	0	0	0.1
Pyramidal <c+a>	909.3	475.2	121.9	0	0	0.1
Extension twinning	0	0	0.8	0	0	0.1
Contraction twinning	3122.7	1294.5	1261	0	0	0.1

CHAPTER III

TUBE EQUAL CHANNEL ANGULAR EXTRUSION AS A METHOD FOR PROCESSING MG-3AL-1ZN ALLOY TUBES AT VARIOUS TEMPERATURES*

This study describes a severe plastic deformation processing technique for tubular materials, in the interest of enhancing mechanical properties via grain refinement and crystallographic texture control. tECAE processing was conducted at 200 °C, 175 °C, and 120 °C. A refined microstructure and increased strength levels after only one pass were achieved. The texture evolution and the active deformation modes, and their relative activities, were successfully predicted using a viscoplastic self-consistent (VPSC) crystal plasticity model as a function of processing temperature.

3.1 Materials and Methods

A commercial hot rolled 25 mm thick AZ31 plate, with a nominal composition of 3% Al, 1% Zn, 0.20% Mn and remaining Mg, was obtained from MetalMart International Inc. and used for all experiments. The as-received material was annealed at 350°C for 12 hours in an argon atmosphere, and subsequently water quenched to produce a twin free, homogenous starting microstructure, as shown in Figure 3.1(b).

---

*Portions of this chapter reprinted with permission from "Tube equal channel angular extrusion" by A. Srivastava, M.W. Vaughan, B. Mansoor, W. Nasim, R.E. Barber, I. Karaman, K.T. Hartwig. Materials Science and Engineering: A 814 (2021), 141236

This annealed and quenched material is called the pre-tECAE condition in this work. The starting texture of AZ31 is shown in Figure 3.1(d).

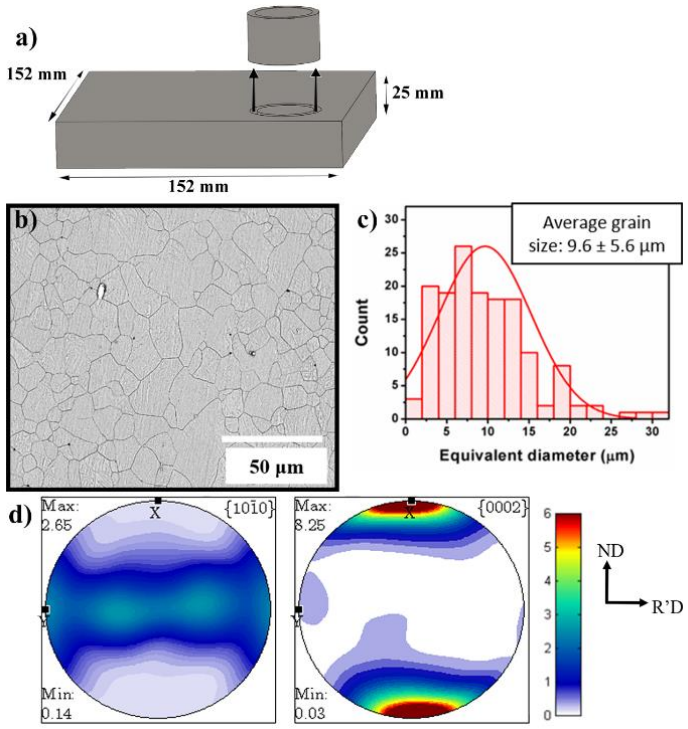

Figure 3.1 (a) Schematic of the AZ31 magnesium plate from which the tube was sectioned. The scanning electron microscopy (SEM) image of the pre-tECAE condition and corresponding grain size distribution are shown in (b) and (c), respectively. (d) shows the experimentally measured $\{10\bar{1}0\}$ and {0002} pole figures of the pre-tECAE condition.

Three tubes with 2.9 mm thick walls and lengths of 25 mm, with 37.8 mm outer and 32.0 mm inner diameters, were cut by wire electrical-discharge machining (EDM) from the AZ31 plate in the pre-tECAE condition (Figure 3.1). The sample orientation was selected such that the axis of the tube was parallel to the normal direction of the plate (see Figure 3.1(a)). This selection gives a unique starting texture for tECAE, with the c-axes

aligned with the axis of the tube (see Figure 3.2(a)), which is for example, different than the initial textures for conventional ECAE of the AZ31 alloy (Figure 3.2(b and c)) taken from Al-Maharbi *et al.* [19]. It is important to note that the starting texture of Mg alloys being processed by ECAE has a significant influence on the formability and the resulting mechanical properties [21].

The tECAE tool was preheated to the desired processing temperature, and one pass of tECAE processing was carried out on three different tubes at 200 °C, 175 °C, or 120 °C. All tubes were lubricated with boron nitride to minimize friction with the tooling. The tECAE experiments were carried out at an extrusion rate of 4.57 mm/min, and each workpiece was removed from the tool following extrusion and water quenched. This extrusion rate was selected based on prior studies on ECAE processing of AZ31 alloys to minimize chances of shear localization [20, 21, 94]. The final dimensions of the tubes after processing were measured, where the outer diameter was about 43 mm, the inner diameter was about 38 mm, and the height was about 23 mm.

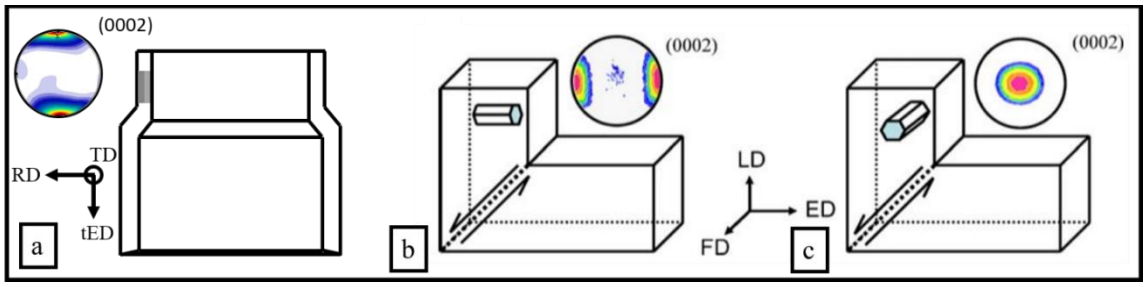

Figure 3.2 The unique initial texture for tECAE in the current work orients the basal planes normal to the tED. In contrast, (b-c) show that in conventional ECAE of AZ31 billets, the basal planes must be parallel to the ED. (b-c) have been adapted from [19].

The samples for microstructure and texture analysis were cut via wire EDM in the plane perpendicular to the tangential direction (TD), which was chosen for investigation because the TD in tECAE is equivalent to the flow direction (FD) in conventional ECAE, and thereby is easy to compare with past studies [19]. To reveal grain boundaries, samples were polished to a final step of 1 μm diamond paste, followed by etching for 5 seconds in acetal-picric solution (2.5 ml acetic acid, 17.5 ml ethanol, 2.5 ml water, and 1.05 g picric acid). The SEM and optical microstructures were observed using an FEI Quanta-600 SEM and a Keyence VH-Z100 digital microscope, respectively. Grain size analyses were done using MIPAR® image analysis software [95].

For crystallographic texture measurements, a Bruker-AXS D8 X-ray diffractometer (XRD) with Cu K_α (wavelength of 0.15406 nm) radiation was used. Pole figures were plotted via the Matlab MTEX toolbox [96]. Vickers microhardness measurements were taken via a Qualitest QV-1000 hardness machine, where at least ten measurements were made on the plane perpendicular to TD. Tensile tests were conducted on flat, "dog-bone" specimens with gage dimensions of 1.5 x 3 x 12 mm^3, cut on the wire EDM in the tube extrusion direction (tED). Tensile tests were performed on an MTS Insight system using a 5 kN load cell at an initial strain rate of 5 x 10^{-4} s^{-1}. Two samples were tested for each tECAE processing.

A viscoplastic self-consistent (VPSC) crystal plasticity model was calibrated (system variables defined) to predict the post-deformation texture and identify the active slip and twinning modes during tECAE processing at various temperatures. The

parameters used are described in Chapter II. The basal (0002) and prismatic $(10\bar{1}0)$ pole figures were predicted along with the active deformation modes.

3.2 Results

3.2.1 Microstructural evolution

Figure 3.3 presents optical microscopy (OM) images of as-annealed (pre-tECAE) and tECAE processed AZ31 magnesium alloy at low magnifications, to illustrate the microstructural changes seen across the thickness of the tube. Here, intersecting micro-shear band regions are observed in the middle of the cross section. In Figure 3.3(c-d), the regions labelled '1' were formed due to shear in deformation zone 1, whereas the regions labelled '2' were formed due to shear in deformation zone 2. Such micro-shear bands are clearly visible in samples processed at 200 °C and 175 °C; however, in the tube processed at 120 °C (Figure 3.3(e)), the shear bands formed almost horizontally. In addition, the tube processed at 120°C showed a high density of twin boundaries (see Figure 3.6).

The average grain size in the material before tECAE was 9.6 ± 5.6 μm (Figure 3.1(b-c)), and it was unimodal. However, a bimodal grain size distribution was obtained in the samples processed at 200 °C and 175 °C, as shown in Figure 3.4-3.5, respectively. These images were obtained from the tangential plane (refer to Figure 2.4 for axis notations).

The bimodality was investigated by dividing the microstructural area into coarse and fine grain regions. The equivalent grain diameters were measured individually as shown in Figure 3.4 (b-c) and Figure 3.5 (b-c). The separate and combined grain size distributions are shown with a normal distribution fitting. For 200 °C processed material,

the average coarse grain diameter is 7.5 ± 2.2 μm, and the average fine grain diameter is 1.6 ± 0.9 μm, giving a combined overall grain diameter of 1.8 ± 1.5 μm. A similar grain size analysis was done for the sample tECAE processed at 175 °C (see Figure 3.5). In this case, the average coarse grain diameter is 7.6 ± 2.1 μm, whereas the average fine grain diameter is 1.4 ± 0.7 μm giving a combined overall grain diameter of 1.5 ± 1.3 μm. The grain size distribution in material processed at 175 °C shows a narrow spread and a higher number of fine grains than the material processed at 200 °C. A similar trend in grain refinement was observed following two passes of conventional ECAE using the routes A and C [19]. A "necklace" grain structure is present in the samples processed at 200 °C and 175 °C (see Figure. 3.4(c) and 3.5(c)), indicative of continuous dynamic recrystallization (CDRX) activated via non-basal slip [25].

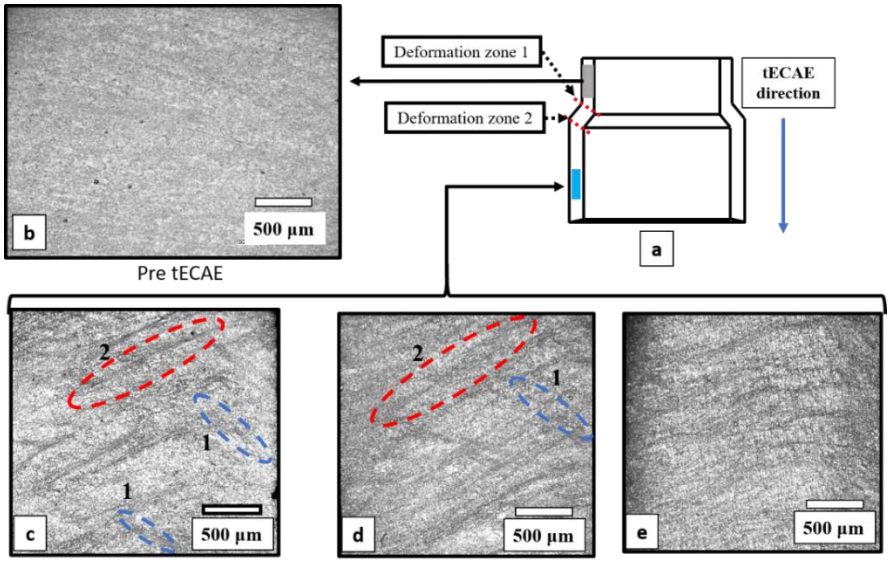

Figure 3.3 (a) Schematic of the pre- and post-tECAE processed tubes, showing the region from which optical microscopy images are taken for (b) pre-tECAE, (c) 200°C tECAE, (d) 175°C tECAE, and (e) 120°C tECAE. Dashed ovals labelled 1 and 2 represent micro shear bands developed during shearing in zones 1 and 2 respectively.

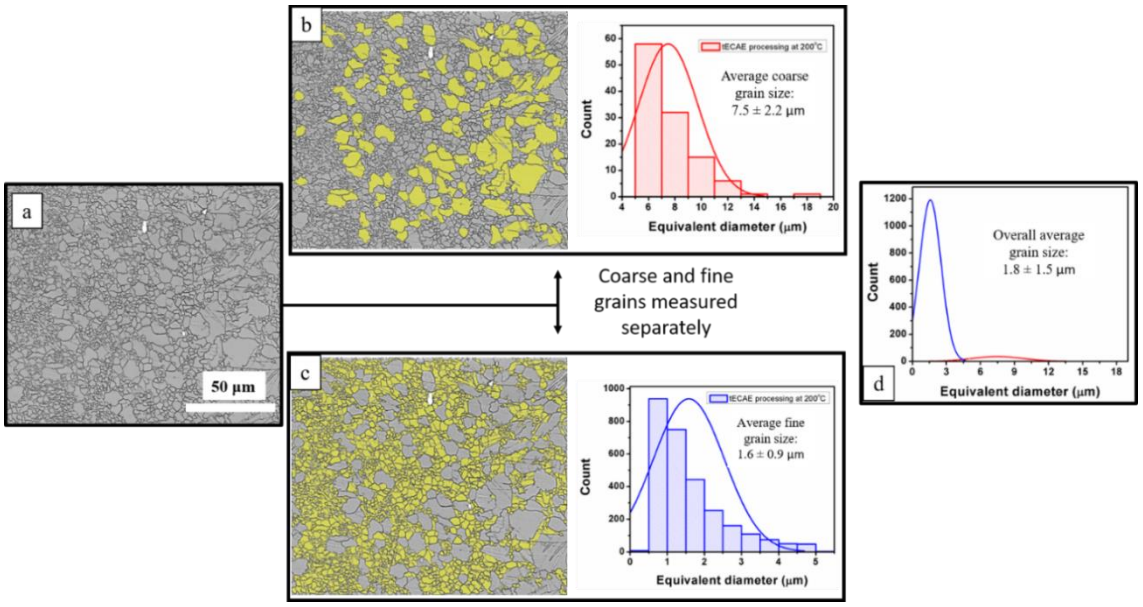

Figure 3.4 (a) SEM image of 200°C tECAE processed AZ31 taken on the tangential plane. (b) and (c) show, respectively, the individual coarse and fine grains, with their size distributions. (d) presents the combined grain size distribution.

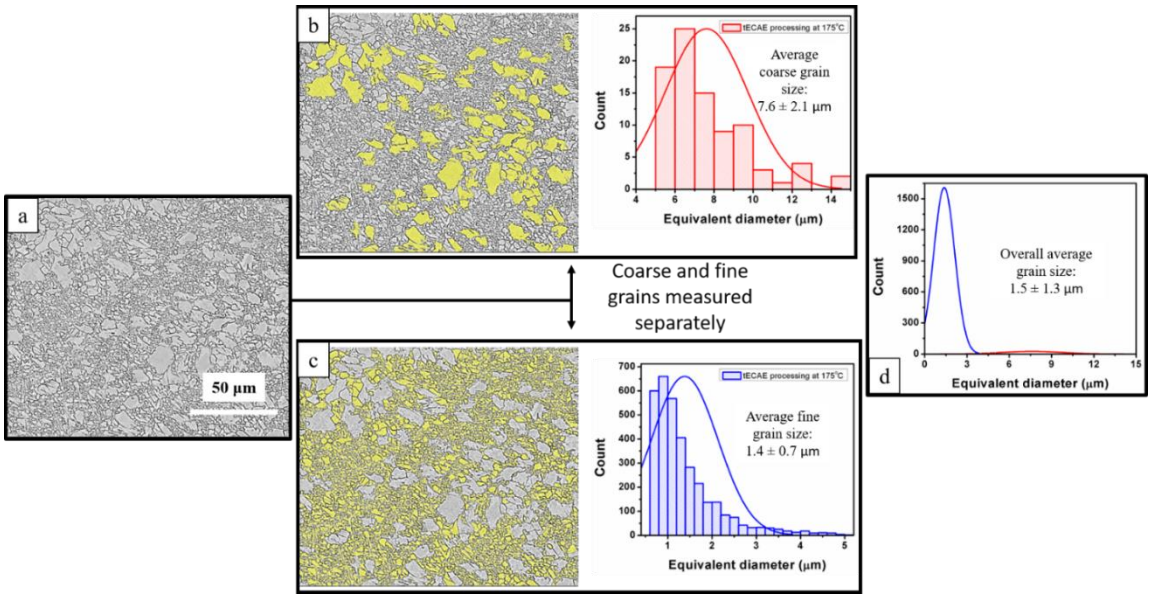

Figure 3.5 (a) SEM image of 175°C tECAE processed AZ31 taken on the tangential plane. (b) and (c) show, respectively, the individual coarse and fine grains, with their size distributions. (d) presents the combined grain size distribution.

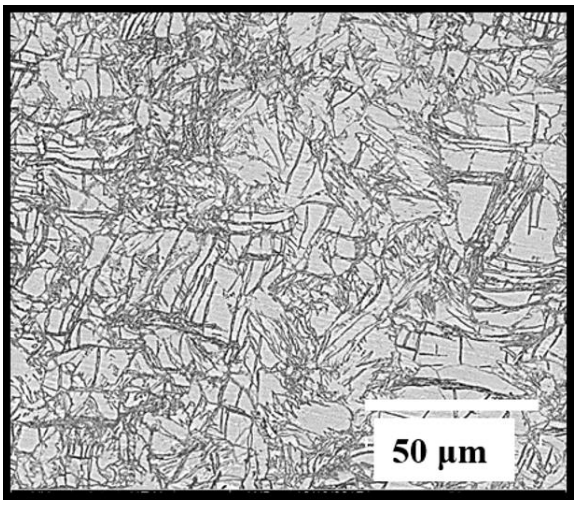

Figure 3.6 SEM image of the AZ31 magnesium alloy sample, tECAE processed at 120°C. Extensive twinning activity is evident.

3.2.2 Texture evolution

The XRD measured texture evolution during one pass of tECAE at 200 °C, 175 °C, and 120 °C are shown in Figs. 11-13, respectively. For comparison, the basal pole figure of pre-tECAE material is also demonstrated in Figures 3.7-3.9, which represents the typical texture of a rolled AZ31 magnesium alloy plate, with the basal planes parallel to the rolling plane and the c-axes generally aligned along the ND [97, 98].

In all the tECAE processed conditions, only subtle changes in texture were observed. In addition, the grains were oriented away from the tED, towards the RD. The final texture obtained after tECAE is, in general, similar to the initial texture.

As texture predictions were conducted using the VPSC crystal plasticity model, for comparison, the simulated results, including the relative deformation mode activities, are displayed along with the experimental results in Figures 3.7-3.9. Here, the simulated

textures showed higher concentrated intensity peaks than the experimental textures, which is due to the model's limitations, i.e. a lack of consideration for dynamic recrystallization (DRX) and grain refinement.

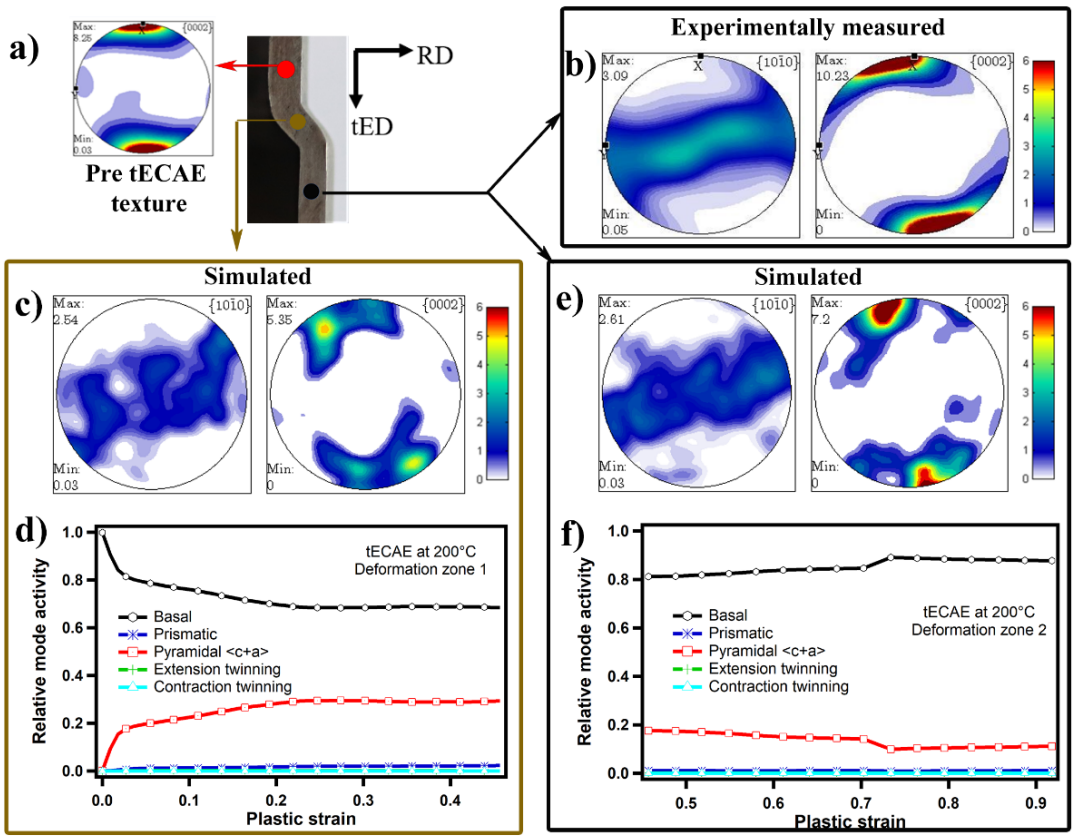

Figure 3.7 (a) Cross-section view of a tECAE processed AZ31 magnesium alloy tube showing regions before tECAE (red arrow), after deformation zone 1 (brown arrow), and deformation zone 2 (black arrow). (b) Experimentally measured prismatic $\{10\bar{1}0\}$ and basal $\{0002\}$ pole figures of the tube after tECAE at 200°C. (c) and (d) show VPSC simulated pole figures and deformation mode activities after deformation zone 1. (e) and (f) display VPSC simulated pole figures and deformation mode activities after deformation zone 2.

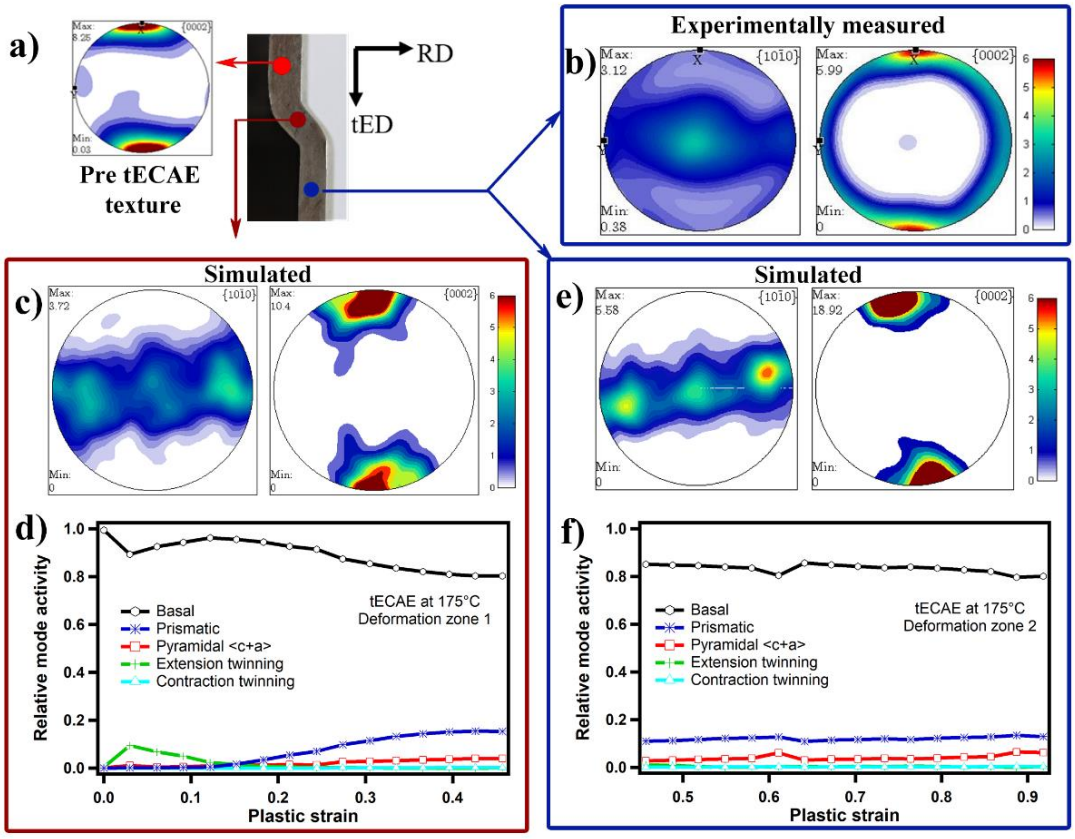

Figure 3.8 (a) Cross-section view of a tECAE processed AZ31 magnesium alloy tube showing regions before tECAE (red arrow), after deformation zone 1 (maroon arrow), and deformation zone 2 (blue arrow). (b) Experimentally measured prismatic $\{10\bar{1}0\}$ and basal $\{0002\}$ pole figures of the tube after tECAE at 175°C. (c) and (d) show VPSC simulated pole figures and deformation mode activities after deformation zone 1. (e) and (f) display VPSC simulated pole figures and deformation mode activities after deformation zone 2.

Because the AZ31 workpiece passes through two deformation zones during one pass of tECAE, the resultant texture evolution is a combination of a two-step deformation process. While the imposed deformation through both zone 1 and zone 2 from one pass of tECAE initially appears reminiscent of the 2C route in conventional ECAE [19], one cannot model tECAE as the conventional 2C route because in conventional ECAE, route

2C imposes a rigid rotation of 90° between passes. In contrast, in tECAE, no such rigid rotation occurs between deformation zones 1 and 2. This effect is further discussed in the next section.

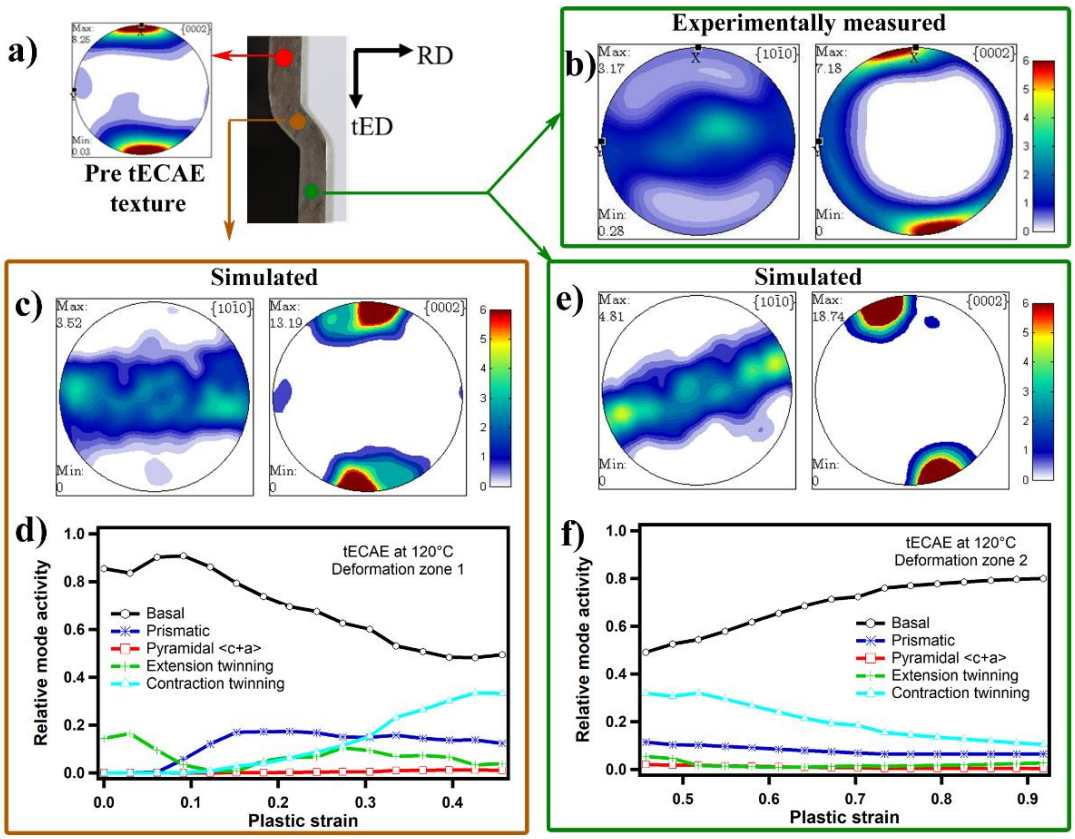

Figure 3.9 (a) Cross-section view of a tECAE processed AZ31 magnesium alloy tube showing regions before tECAE (red arrow), after deformation zone 1 (brown arrow), and deformation zone 2 (green arrow). (b) Experimentally measured prismatic $\{10\bar{1}0\}$ and basal $\{0002\}$ pole figures of the tube after tECAE at 120 °C. (c) and (d) show VPSC simulated pole figures and deformation mode activities after deformation zone 1. (e) and (f) display VPSC simulated pole figures and deformation mode activities after deformation zone 2.

The onset of texture weakening from the initial strong wrought basal plate texture was observed in all the tECAE cases due to the presence of the active deformation modes, as shown in Figures 3.7-3.9. Basal slip was found to be active at all temperatures, which is well documented as it is the most active deformation mechanism in Mg alloys. It was found that tECAE processing at 200°C enabled pyramidal $< c + a >$ slip to become much more active relative to lower tECAE temperatures, demonstrating readily activation of this slip system above 180°C [45] (see Figure 3.7 (d) and (f)). In contrast, tECAE at 175°C favored the activation of extension twinning during the initial stages of deformation, until a strain of ~ 0.1, and, subsequently, prismatic $< a >$ slip activity was observed along with the basal slip (see Figure 3.8 (d) and (f)). Lastly, for tECAE at 120°C, twinning played a major role in the deformation process. Here, extension and contraction twinning were active along with basal $< a >$ and prismatic $< a >$ slip.

3.2.3 Mechanical properties

The average Vickers hardness values obtained for the AZ31 magnesium alloy before tECAE and after tECAE processing at 200°C, 175°C, and 120°C are listed in Table 3.1. The microhardness of the pre-tECAE processed sample was the lowest whereas an increase in microhardness is observed as the tECAE processing temperature decreased. The maximum microhardness was obtained for the sample processed at 120°C.

Figure 3.10 presents the tensile true stress vs. true strain responses of the pre-tECAE and post-tECAE processed samples. The tensile response of a bulk AZ31 sample processed by one pass of conventional ECAE at 200°C [19] is also shown in Figure 3.10

for comparison. The strain level achieved in one pass of tECAE (i.e. two shear deformation zones) is about the same as the strain level imparted to the material processed by one pass (single shear zone) of conventional ECAE.

Table 3.1 Tensile mechanical properties and Vickers hardness results for the AZ31 magnesium alloy after different processing conditions.

	Tensile test			Vickers Hardness
Processing Condition	**0.2% YS* (MPa)**	**UTS** (MPa)**	**Elongation (%)**	**HV_{300}**
Pre-tECAE	79	345	17.6	55.8 ± 3.0
tECAE @ 200°C	132	357	20.5	63.2 ± 2.1
tECAE @ 175°C	161	305.5	10.5	66.2 ± 3.0
tECAE @ 120°C	199	265	3.2	76.7 ± 1.8
Pre ECAE [19]	58.5	319	14.9	-
200°C ECAE (1A) [19]	100	256.5	11.2	-

*YS = Yield strength, **UTS = Ultimate tensile strength

The tension test samples, from the conventional ECAE processed billet, are machined along the longitudinal direction (LD) of the billets, to enable texture comparison with tECAE processed samples. The c-axes are oriented along the LD for conventional ECAE, which is similar to their orientation after tECAE. Relative pole figures of ECAE and tECAE processed samples at 200°C are also shown in Figure 3.10 for comparison with the tensile loading direction, which is the LD for conventional ECAE and the tED for tECAE. Therefore, both tensile results are comparable and allow for texture effects to be largely ignored when comparing mechanical properties.

Table 3.1 shows the yield strength, ultimate tensile strength (UTS), elongation to failure, and Vickers hardness values of all processed materials. The sample tECAE

processed at 200°C shows the highest UTS and elongation. As the tECAE processing temperature was decreased, the yield strength increased, but the tensile strength decreased. A comparison of the tECAE and conventional ECAE results for 200°C processing shows that the tECAE material has significantly higher yield strength, tensile strength, and elongation to failure despite the similarity of textures (Figure 3.10).

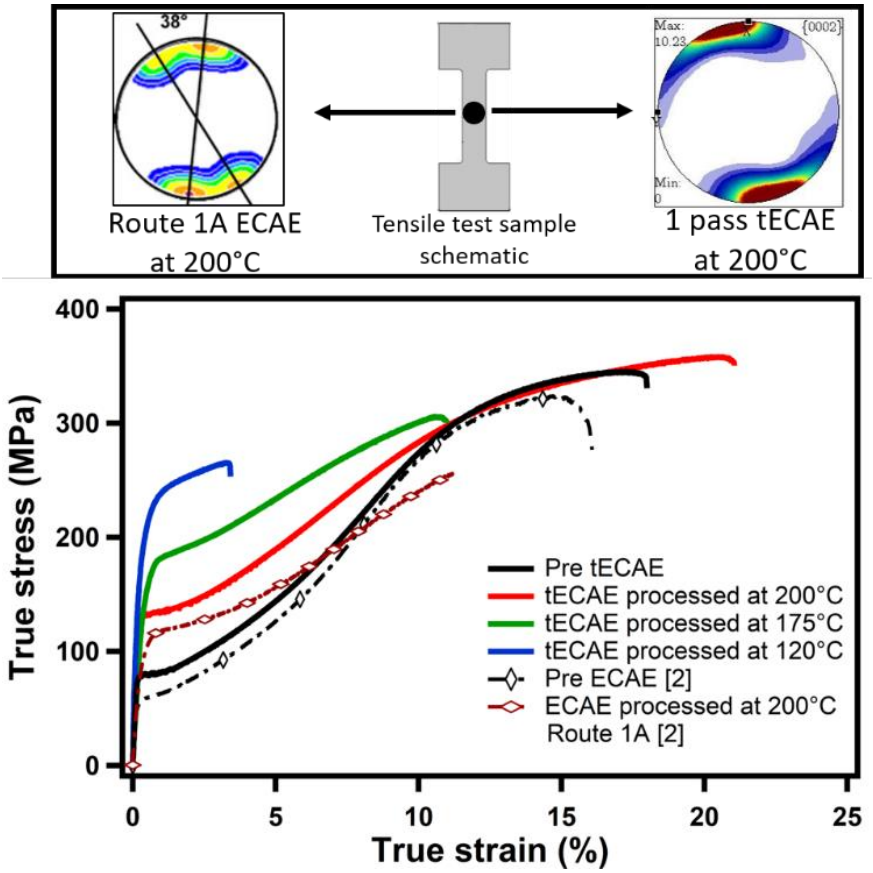

Figure 3.10 Top – the crystallographic texture results for the 200°C ECAE [19] and 200°C tECAE tensile samples are included for comparison. Bottom - room temperature tensile true stress vs. true strain responses of bulk AZ31 after different processing conditions.

3.3 Discussion

3.3.1 Microstructure evolution

Figures 3.3-3.6 show the microstructures of the AZ31 tubes after one pass of tECAE conducted at 200 °C, 175 °C, or 120 °C, respectively. The tECAE processing temperature has a significant effect on the microstructure developed. For 200 °C processing, a bimodal grain size distribution is obtained after one pass (Figure 3.4), and two observations are noteworthy. First, microstructure is refined from the original large grain size, but the refinement is not homogenous. A plausible explanation for such a size distribution is that the accumulated strain intensity was insufficient for uniform grain refinement as the material has undergone only one tECAE pass. Second, no twin deformation modes are active, thereby limiting refinement via the formation of twin boundaries. Similar to 200 °C tECAE, the material after tECAE processing at 175 °C (Figure 3.5) showed bimodal grain size distributions, where twinning was rarely observed. In general, when a Mg alloy is deformed, high stress concentration occurs at the grain boundaries due to limited slip compatibility with the neighboring grains [99]. This high stress concentration along with elevated temperature (above 175 °C in present study) assists in activation of hard non-basal slip systems to maintain slip compatibility. The non-basal dislocation could cross slip or lattice rotation could occur leading to formation of sub-grains along grain boundaries. Accumulation of dislocations or grain boundary migration will increase the misorientation of sub-grains, hence, resulting in a necklace like formation of new fine grains along grain boundaries via dynamic recrystallization mechanism while leaving the core of the grains less refined hence leading to bimodal grain

size distribution [99, 100]. These findings are also supported by VPSC simulations (Figure 3.8(d, f)), indicating that tECAE at 200 °C and 175 °C favors the activation of non-basal slip systems to accommodate plastic flow, which likely limits the degree of grain refinement due to lack of twinning.

In contrast, the material processed at 120 °C (Figure 3.6) displays a significant volume fraction of twins. At lower temperatures, the critical resolved shear stress (CRSS) for prismatic and pyramidal slip are high and hence much harder to activate, so achieving homogenous deformation is difficult [50]. Therefore, activation of twinning systems is expected, and relative activity of deformation modes simulated by VPSC supports this observation. However, twin boundaries can serve to strengthen the material, as evident by the higher hardness and yield strength for tECAE samples processed at 120 °C (Table 3.1). Performing multiple passes of tECAE should result in further grain refinement and homogenization of the microstructure similar to conventional ECAE as strain accumulates with each pass.

Notice also that fragmented substructures, such as the micro shear bands, are produced that extend along the shear direction in tECAE samples processed at 200 °C and 175 °C (Figure 3.3). The fine shear bands formed at different deformation zones intersect in the middle of the sample and results in fine dynamically recrystallized (DRX) grains [21]. From Figure 3.4 and 3.5, it is likely that these DRX grains formed via continuous DRX (CDRX), due to the accumulation of applied strain, which leads to the formation of low angle grain boundaries which eventually transform into high angle grain boundaries [101, 102] via non-basal slip [103]. VPSC predictions of active deformation modes at 200

°C (see Figure 3.7) showed that along with basal slip, pyramidal $< c + a >$ slip was also active at 200 °C especially during deformation zone 1, while prismatic slip was active at 175°C to accommodate applied deformation, supporting the inference that CDRX was the mechanism by which these DRX grains formed.

3.3.2 tECAE-imposed texture evolution and VPSC modeling

The textures shown in Figures 3.7-3.9 for tECAE at different temperatures show only subtle changes after one pass in comparison to the initial pre-tECAE texture. Nevertheless, the materials processed at different temperatures show differing degrees of shift in texture orientations. This minimal change in texture is probably due to the combined effects outlined as follows:

(i) The amount of deformation imposed by tECAE is insufficient to necessitate significant changes in texture after one pass. In this regard, notice that only a small change in texture is obtained after 1 pass of conventional ECAE as well [19, 21], where the imposed total accumulated strain is slightly higher than it is here (1.16 vs. 1.05).

(ii) The possible lack of texture change is rooted in the nature of the tECAE shearing. The shear strain applied in deformation zone 1 is opposite in direction to that applied in deformation zone 2 (similar to route 2C of conventional ECAE). So, the grains, which oriented to the new orientation after deformation zone 1, are partially reoriented back towards the initial orientation after deformation zone 2.

(iii) The starting texture in deformation processing of Mg alloys plays a significant role in the texture evolution. The initial texture in all the tECAE conditions is such

that the c-axis is along the tED direction, leading to contraction along c-axis during tECAE processing. It is also reported in the literature, that contraction along the c-axis leads to limited texture modification [104]. The contraction twins formed, during low temperature deformation, are narrow and, hence, the volume fraction of twins is low. Because twinning is largely responsible for texture evolution, the minimal activation of twinning results in only a small change in texture for tECAE at 175 °C and 200 °C [104]. However, when twinning is strongly active, as in tECAE at 120 °C, it appears that the unique nature of tECAE, being symmetric with two shear deformation zones that are orthogonal to one another, results in minimal texture evolution overall.

Regarding deformation mechanisms, it is well established that Mg, having an HCP crystal structure, has insufficient slip system for homogenous deformation at low temperatures; hence, twinning compensates for this limitation and provides formability to Mg [105]. Activation of these deformation modes depend on their critical resolved shear stress (CRSS), which is dependent on temperature for non-basal slip whereas it is athermal for basal slip and twinning systems [44, 50, 105]. Thus, slip systems along with twinning, play a significant role in the texture evolution during tECAE.

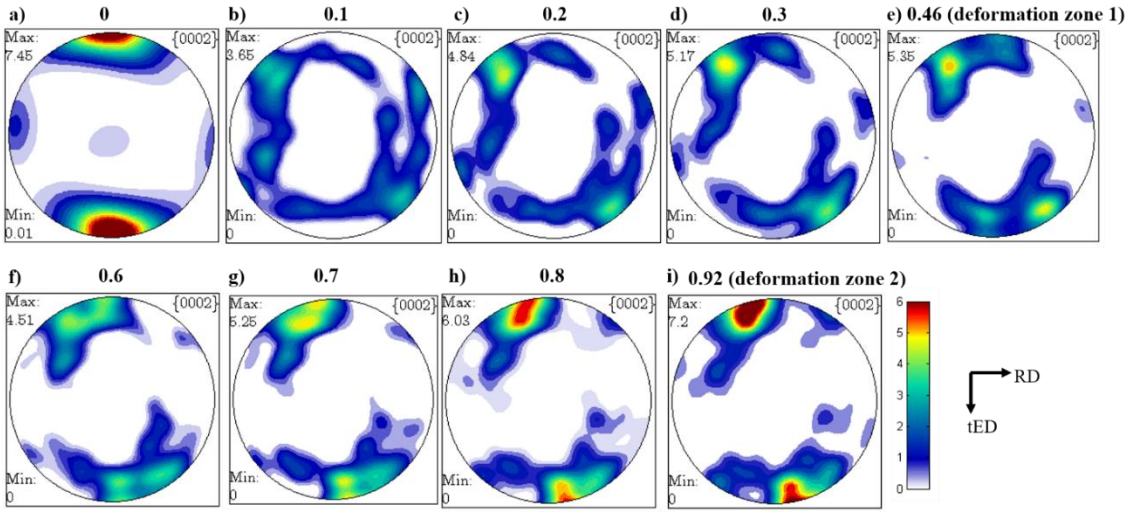

Figure 3.11 Simulated texture evolution during tECAE of AZ31 magnesium alloy at 200°C with increasing plastic strain ({0002} pole figures are shown). Applied plastic strain on (a) 0, (b) 0.1, (c) 0.2, (d) 0.3, (e) 0.45 (after deformation zone 1), and (f) 0.6, (g) 0.7, (h) 0.8, and (i) 0.92 (after deformation zone 2).

With this in mind, the texture evolution and the active deformation modes are shown in Figure 3.7 after tECAE processing at 200 °C. Simulated texture results, after passing through deformation zone 1, shows a rotation of basal poles away from the tED direction. This rotation gets partially reverted towards the tED after the material passes through deformation zone 2. To understand the texture evolution incrementally with applied strain during tECAE processing, VPSC simulations are used to predict the texture evolution at different stages of plastic strain. For 200°C, Figure 3.11 (a-i) shows the predicted basal pole textures with incremental strain during tECAE processing.

Basal poles appear to orient away from the tED when the tube passes through deformation zone 1, and as the strain increases, the basal texture intensifies, indicating that most of the material's basal planes have reoriented in the same fashion. However,

when the tube passes through deformation zone 2, due to the reversal in strain direction, the basal texture reorients towards tED direction again (Figure 3.11 (f-i)), hence confirming that the shear direction plays a significant role in the texture change. The deformation mechanisms' activities leading up to deformation zone 1 and deformation zone 2 are shown in Figure 3.7 (d) and (f), respectively, for 200°C tECAE processing. Here, the relative mode activity vs plastic strain plot shows basal slip to be the most active mode, followed by pyramidal $< c + a >$ slip (see Figure 3.7 (d) and (f)). At this temperature, the pyramidal $< c + a >$ slip accommodates the c-axis deformation. Additionally, prismatic slip or twinning activity were suppressed. Similar texture results were obtained by Al-Maharbi *et. al.* [19] during conventional ECAE processing as well. Thus, it seems plausible that texture evolution was enacted via pyramidal $< c + a >$ slip during tECAE at 200°C, where deformation zone 2 reversed the texture evolution imposed via deformation zone 1, resulting in minimal texture changes overall while yielding significant grain refinement after only a single pass.

When the tECAE processing temperature was reduced to 175 °C, a limited change in texture was seen as well. At 175 °C, the activation of extension twinning was seen in the initial stages of deformation and was followed by prismatic slip activity (Figure 3.8 (d, f)). The activation of extension twinning causes the grains to reorient by 86.4°, which leads to the basal plane orienting perpendicular to the tECAE direction; hence, prismatic slip can activate later in the process [25]. Again, due to the nature of shear deformation in tECAE, texture change was limited. It appears from Figure 3.8 and 3.12 that extension twinning resulted in texture evolution away from the tED. However, after extension

twinning was activated, it was replaced for the more favorable prismatic $< a >$ slip through the rest of the shear deformation zones 1 and 2. Thus, prismatic slip prevented abrupt texture evolution at 175 °C. It is also worth noting for 200 °C and 175 °C that strain can be accommodated via DRX, which is not accounted for in the VPSC model. Thus, the experimental textures can maintain perhaps an even more similar texture to the pre-tECAE one, given the contributions of DRX.

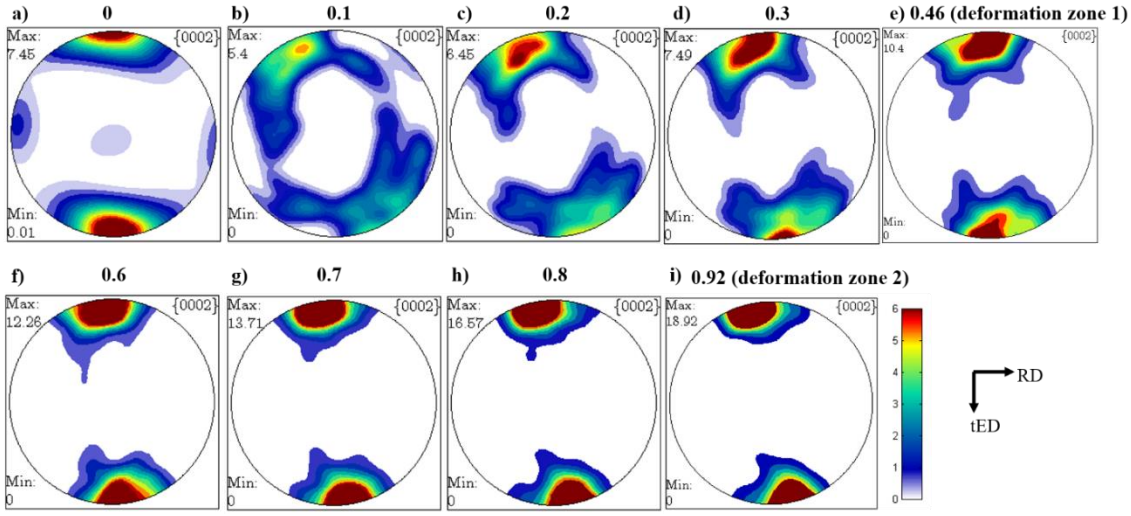

Figure 3.12 Simulated texture evolution during tECAE of AZ31 magnesium alloy at 175°C with increasing plastic strain ({0002} pole figures are shown). Applied plastic strain on (a) 0, (b) 0.1, (c) 0.2, (d) 0.3, (e) 0.45 (after deformation zone 1), and (f) 0.6, (g) 0.7, (h) 0.8, and (i) 0.92 (after deformation zone 2).

In comparison to 175 °C and 200 °C, AZ31 tubes tECAE processed at 120 °C are somewhat of a novelty, as it is not possible to conduct first pass conventional ECAE directly at such a low temperature on AZ31. Given the discussion of the texture evolution effects of tECAE, it appears that the 180° opposed deformation zones 1 and 2 in tECAE

can enhance the capability for grain refinement and formability at such low temperatures. According to Figure 3.9, tECAE at 120 °C results in minimal texture change overall, yet Figure 3.9 (d,f) show that extension twinning is highly active initially, while passing through deformation zone 1. In contrast, contraction twinning becomes favored afterwards, throughout deformation zone 2. These deformation modes are coupled strongly by prismatic and basal slip activity, indicating that many deformation mechanisms are activated simultaneously during tECAE at 120 °C.

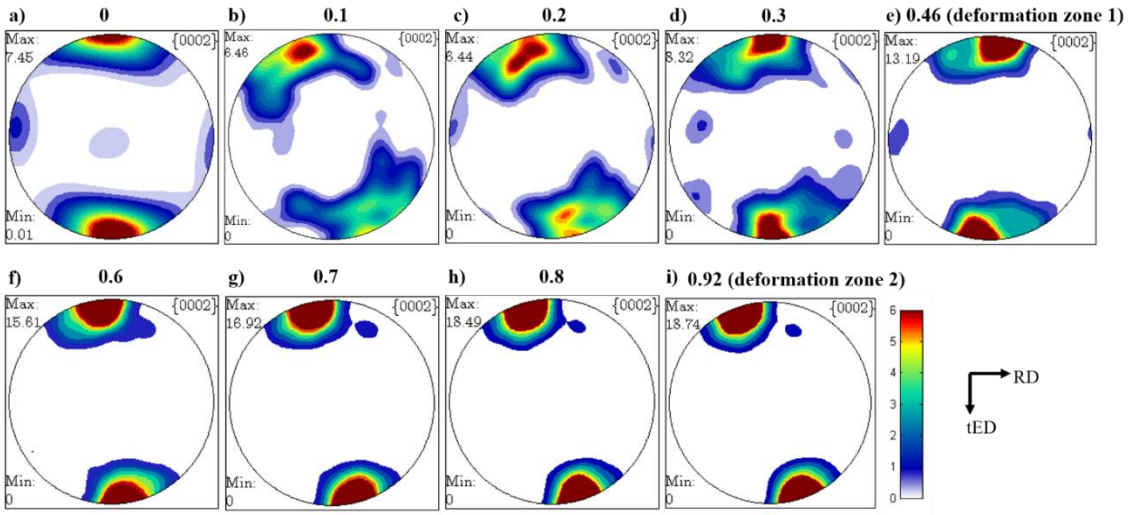

Figure 3.13 Simulated texture evolution during tECAE of AZ31 magnesium alloy at 120°C with increasing plastic strain ({0002} pole figures are shown). Applied plastic strain on (a) 0, (b) 0.1, (c) 0.2, (d) 0.3, (e) 0.45 (after deformation zone 1), and (f) 0.6, (g) 0.7, (h) 0.8, and (i) 0.92 (after deformation zone 2).

Given the complexity of the active deformation mechanisms from Figure 3.9 (d,f), Fig. 3.13(a-i) sheds some additional light on the intermediate textures that develop during tECAE at 120 °C. Here, it appears that the texture initially is modified via extension

twinning, as shown previously in tECAE at 175 °C. Given the extensive activity of deformation mechanisms favoring c-axis strain for tECAE at both 120 °C and 200 °C, the greater texture change for these two conditions after tECAE in comparison to tECAE at 175 °C may be a consequence of the c-axis strain accommodation at 200°C and 120 °C. In addition, the presence of extension twinning, followed by contraction twinning at 120 °C, indicates that double twinning occurred at this temperature. This could explain the lower elongation to failure levels for tECAE at 120 °C, as double twinning leads to void nucleation and macroscopic failure [25, 54]. Thus, it appears that tECAE processing is, in a way, a combination of contraction along the tED direction and extension along the RD direction, so, to accommodate c-axis contraction, either the pyramidal slip or contraction twinning deformation mode is required [49]. Since at 120 °C, the tECAE processing is performed at low temperature, activation of hard pyramidal $< c + a >$ slip is difficult [50]; hence, extension, contraction, and perhaps double twins formed to accommodate this strain imposed via tECAE given the initial texture.

Overall, it appears that one pass of tECAE results in minimal texture change, despite the activation of a variety of different deformation mechanisms. Here, it appears that the unique strain state imposed by deformation zone 1 and 2, which are orthogonal to one another, prevent strong texture change while favoring grain refinement. In fact, even at 120 °C, texture change is minimal. This is advantageous when texture change is undesirable; however, if strong texture modification is the goal, tECAE may not serve the purpose, although, the results of multiple passes of tECAE are yet to be determined. Thus, the introduction of different die angles for deformation zone 1 and deformation zone 2

may be important for future tECAE tool designs, in the interest of designing a SPD technique of tubes that enables unique tube textures to be developed.

3.3.3 Mechanical properties

Tensile tests were conducted by applying tension along the tED axis. The texture evolution results indicate that mostly c-axis extension is involved for tension in this direction. Significant strain hardening is observed in all cases. The initial stain hardening occurs due to extension twinning, which further leads to hardening by non-basal slip [97]. A significant increase in yield strength after tECAE processing is seen in Figure 3.10. This was expected at lower temperatures due to the grain size refinement and the existence of twin boundaries. Also, according to the Basinski mechanism, glissile dislocations in the matrix are transformed into sessile dislocations inside twins, leading to a further increase in strength [104]. Among the tECAE processed materials, the lower the processing temperature, the higher the resulting yield strength. However, at lower temperatures, the tensile strength is low. In 120 °C tECAE processed material, which has a heavily twinned structure, abrupt and early failure occurs possibly due to stress concentration at the twin boundaries [25].

The sample processed at 200 °C shows the highest elongation to failure compared to the lower temperature processed samples. This is due to the presence of small DRX grains and the absence of twinned grains obtained after tECAE processing. The tensile response of the conventional ECAE processed AZ31 magnesium alloy, taken from [19], is also shown in Figure 3.10 for comparison with the tECAE processing. Tensile stress-strain responses of similarly textured AZ31 samples processed at 200 °C by conventional

ECAE and tECAE are shown, thus, isolating the effect of texture on tensile flow response of AZ31. The tECAE processed materials demonstrate better tensile properties than the conventional ECAE processed materials due to the improved grain refinement in tECAE processed material. The grains obtained in [19] have DRX grains of 1 - 5μm and a non-recrystallized average grain size of 20 μm which is larger than that obtained in the tECAE processed material. Note that the initial grain size in conventional ECAE processed material in ref. [19] was larger than the present AZ31 hot rolled plate (25 μm vs. about 10 μm). Along with this, the microhardness of tECAE processed material is higher than the pre-tECAE material, as expected from Hall-Petch strengthening [56]. Tube ECAE processed materials have refined grains, and additional twin boundaries at lower temperature processing which contribute to the strength, resulting in a higher hardness.

3.3.4 Opportunity for low temperature processing of Mg alloy tubes

It is important to note that in the present study, one pass of tECAE directly at the low temperature of 120 °C was successful, which may be attributable to important microstructural and likely configurational factors. In comparison, several prior works have shown that hot rolled AZ31 cannot be directly processed successfully at temperatures below 150 °C via conventional ECAE [19, 21, 94]. Rather, in conventional ECAE, typically, multiple passes via a temperature-step-down method are required in order to process AZ31 below 150 °C [21].

One important factor that may have contributed to successful processing of AZ31 by tECAE at such low levels of temperature i.e. 120 °C is the relatively fine grain size (~10 μm) of the starting material. Refined grain size minimizes twinning-induced failure

[106, 107] by suppressing twinning modes. Likewise, the initial texture of material significantly affects the active deformation modes [21, 25]. This is highlighted by the stark differences between the texture of starting material used for tECAE versus conventional ECAE which appears to have had a positive impact on formability in tECAE. Regarding formability, it is worth noting that the accumulated strain per deformation zone was lower in tECAE as compared to conventional ECAE. Also, the axisymmetric deformation in tECAE by a combination of simple shear and circumferential strain provided a uniform tube thickness which was not possible to attain using conventional ECAE. Thus, tECAE is indeed useful for low temperature processing of Mg alloy tubes.

3.4 Summary

A new technique of tube ECAE processing, called tECAE, has been introduced herein. This SPD technique has the potential of drastically enhancing the mechanical properties of tubular materials. The influence of one pass of this SPD technique on texture evolution and deformation mode activity was investigated utilizing both experimental observations and simulations. The tECAE approach successfully processed AZ31 alloy tube directly at 120 °C, where conventional ECAE processing of AZ31 bulk alloy is not possible. Refined grain sizes, with higher yield strengths and elongation to failure levels in comparison to the pre-tECAE material was obtained after only a single pass of tECAE.

tECAE imposed minimal texture change at a variety of different processing temperatures, owing to the tool geometry. In addition, tECAE appears to maintain minimal texture change due to the activation of c-axis deformation mechanisms; thus, texture changes remained subtle even when twinning modes were highly active, at 120°C.

Although only a slight change in texture is obtained after one tECAE pass, the onset of weakening the basal texture obtained, forecasts that multi-pass tECAE is an appealing method to promote further texture modification and possibly further weakening the basal texture.

VPSC simulations were used to accurately predict texture and active deformation modes during the one pass tECAE processing. Different deformation mode activities were obtained by tECAE processing at different temperatures. Being able to predict the deformation modes can help in designing the experiments and tools to achieve better desired properties via tECAE.

Only one pass of tECAE was performed herein. Grain refinement and improvement in mechanical strength of AZ31 tubes after one pass of tECAE confirm that this technique could be used to fabricate strong tubular Mg products. The effects of multiple passes of tECAE on other materials is explored in the later chapters of this report.

CHAPTER IV

THE ROLE OF STARTING TEXTURE ON TUBE EQUAL CHANNEL ANGULAR EXTRUSION OF MG-3AL-1ZN ALLOY

The evolution of texture after tECAE processing of AZ31 alloy depends on several factors including rate of extrusion, temperature, and initial grain orientations in the tube. The effect of processing temperature is already discussed in Chapter III. In this chapter, AZ31 tubes are tECAE processed at the most widely used ECAE processing temperature of 200 °C while investigating the role of the starting texture on processability of the tubes. The objectives of this study are:

1. To understand the influence of starting texture on tECAE processing of Mg alloys. In the previous studies on conventional ECAE [19, 21] it has been observed that mechanical properties and processabilities are significantly influenced by the starting texture.
2. Develop a VPSC model that successfully predicts texture evolution after complete (2 passes) tECAE processing.
3. To compare the strengths and ductility of post-processed AZ31 tubes with commercially extruded tube.
4. To investigate the failure mechanism of tubes during tension tests.

4.1 Materials and Methods

A 50 mm thick commercial hot-rolled AZ31 plate (nominal composition: 3% Al, 1% Zn, 0.20% Mn and remaining Mg) purchased from MetalMart International Inc. was

used in this study. The plate was annealed at 350 °C for 12 hours in argon atmosphere followed by quenching in water to reduce the presence of mechanical twins and have a homogenous starting microstructure prior to deformation processing. The material in this condition is called AsRec from here onwards throughout the text. Three tubes, 50 mm long, 38 mm outer diameter and 3 mm thickness were cut from the plate on a wire electro-discharge machine (EDM) from three different orientations as shown in Figure 4.1. Each tube was further sectioned from the middle to obtain the final tube length of 25 mm for tECAE processing.

The tubes are named according to the orientation of their axes with respect to the reference axes shown in Figure 4.1. The rolling direction (R'D) of the plate is along the x-axis; the transverse direction (TD) is along y-axis; the normal direction (ND) is along z-axis. The tubes along x and y axes essentially show similar behavior, hence results from only one tube, along the y-axis, are presented here. The tube with its axis along the y-axis is referred to as AY and that along the z-axis is referred to as AZ in this work. The different tube orientations were selected to study the effect of different starting textures for tECAE processing of this Mg alloy. This was possible because the rolled Mg plate has strong texture with basal poles oriented primarily along the plate normal direction as expected.

The tECAE processing was performed at 200 °C with an extrusion speed of 4.57 mm/min. The tool was preheated to 200 °C and the sample was placed in the tool for 20 minutes, a sufficient time for the tubes to reach thermal equilibrium. All the tubes were wrapped in Teflon sheet to reduce friction between the tool and the tube workpiece. In

the expansion pass, the tube comes out in the expanded form with the outer diameter of the tube being 43 mm, and the inner diameter being 38 mm, and the height being 23 mm. The expanded tube after the expansion pass is then processed in the tECAE contraction tool for the contraction pass at 200 °C. This brings the tube back to its original dimensions which is the essence of ECAE processing so that a high amount of strain can accumulate by multiple passes. The tECAE process applies axisymmetric loading, leading to uniform axial and radial deformations. Additionally, after each tECAE pass, the tube is quenched in water to retain the as-processed microstructure.

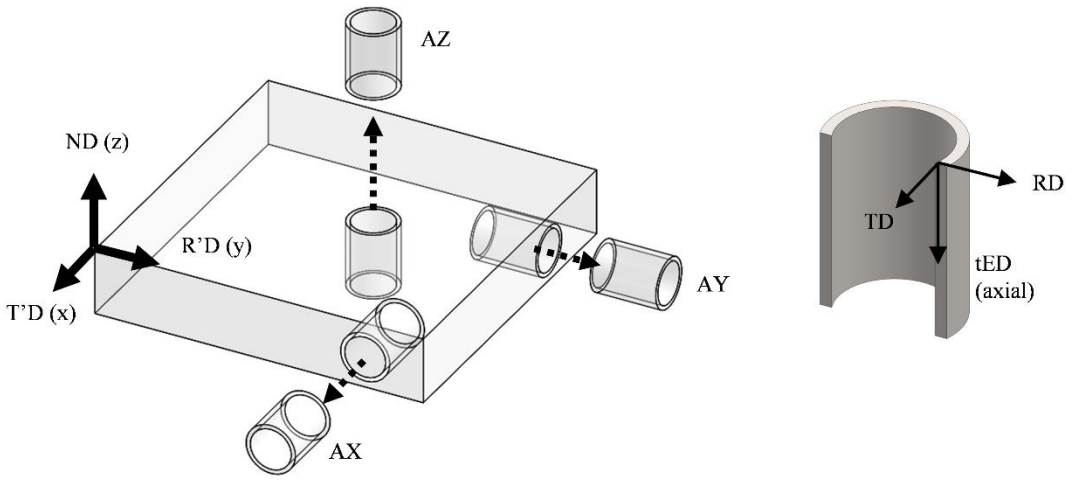

Figure 4.1 Schematic of AZ31 plate and the orientations of the tubes cut from it. ND is the normal direction along the z-axis. R'D is the rolling direction along the y-axis. T'D is the transverse direction along the x-axis. The tubes are labelled according to the orientation of the tube axis with respect to x, y, or z co-ordinates. The reference used for the tubes are TD for the tangential direction, RD for the rolling direction, and tED for the tECAE processing direction.

To analyze the microstructural features of the material, all the samples were cut by wire EDM along the plane perpendicular to the tangential direction (equivalent to the

flow plane in ECAE, refer to Figure 2.1 for orientation notation). The microstructure was investigated using a Keyence VH-Z100 optical microscope (OM), and a Tescan FERA scanning electron microscope (SEM). The samples were mechanically polished upto 1 μm followed by etching with acetic-picral solution the composition of which is already mentioned in Chapter III to reveal the grain boundaries.

Texture results were obtained using a electron backscatter diffraction (EBSD) detector from Oxford Instruments equipped on the Tescan FERA SEM. The samples were mechanically polished to 1200 grit size, then chemically polished in 10% Nital solution for 10 minutes, followed by a final surface preparation via ion milling using a Leica EM TIC 3X for 30 minutes with an accelerating voltage of 5 KeV and a sample inclination of 3° to get a clean, flat surface. For EBSD data, 20 keV accelerating voltage was used with the resulting indexing rate between 60% and 95%. The step size was appropriately selected depending on the grain size of the sample. Since the AsRec grains are coarse, a step size of 0.5 μm was used, whereas for tECAE processed fine grain material, a step size of 0.1 μm was used. The EBSD results were analyzed using AztecCrystal software from Oxford Instruments. The data clean-up consisted of wild spikes (isolated pixels different from all of their neighbors) removal and zero solution removal with no less than 5 indexed neighbors' agreement. Various information such as Inverse pole figure (IPF), kernel average misorientation (KAM), twin boundaries on band contrast (BC) maps, and pole figures were obtained during post-processing of data for a detailed investigation of texture evolution.

Microhardness measurements were taken on a Leco LM300AT Vickers hardness set up from the extrusion plane of the sample by applying a load of 300 g with a dwell time of 13 seconds. For the hardness measurements, the cross-section was divided into 12 regions each separated by 30° angle. Five readings were taken from each region starting from a location close to the outer surface and moving towards the inner surface. A total of 60 measurements were taken on each sample to determine the homogeneity of hardness.

Flat "dog-bone" shaped tension specimens with gage length of 8 mm and cross-section of 1.5 x 3 mm^2 were prepared to conduct tensile tests on a servo-hydraulic MTS system at room temperature. From the AsRec condition, samples were cut from two different orientations, one with gage length along the normal direction (referred to as 0° ND), and another perpendicular to the ND (referred to as 90° ND). For the tECAE processed condition, the gage length was along the tED orientation. At least two tension specimens were tested for each condition with an initial strain rate of 5×10^{-4} s^{-1}. To carry out a detailed investigation of the failure mechanism during the tension tests, fractured samples were polished and etched with acetic-picral solution along the gage length near the fractured region to reveal the grain boundaries, and analyzed under the SEM and OM. For comparison, a commercial AZ31 extruded tube was also tensile tested, and the fractured microstructure investigated. While EBSD results were obtained for fractured commercial AZ31 tube, an extremely low indexing rate was obtained for samples tensile tested post tECAE processing, hence, not included in this study.

A VPSC crystal plasticity model was used in this study as well to predict the texture evolution after two passes of tECAE. A brief introduction to the model is provided in Chapter II.

4.2 Results

4.2.1 Microstructure and texture evolution

Figure 4.2 depicts the OM and SEM images of the AsRec and tECAE processed tubes. Here, the AsRec material shows fully recrystallized microstructure with a mixture of coarse and relatively fine grains distributed throughout the material with an average grain size of 10.8 ± 9.9 μm. The particles circled in Figure 4.2(b) aligned mostly along the rolling direction (R'D) are Al_8Mn_5 particles. The AY and AZ tubes both show substantial grain refinement after tECAE processing, although the grain refinement is not homogenous, especially in the AZ tube. Fine grains formed by shear deformation and dynamic recrystallization are arranged in-between unrefined grains (dotted white circle in Figure 4.2(e)) forming large shear bands in the AZ tube. The presence of several twinned grains can also be seen in the AZ tube. The average grain size in the tECAE processed AY tube is 1.5 ± 0.9 μm with the largest grain size being 11.3 μm and the smaller grain size being 0.4 μm. In contrast, the AY tubes show more uniform grain refinement. The tECAE processed AY tube is free of shear bands, although some coarse grains are still present. The average grain size in the tECAE processed AZ sample is 1.8 ± 1.2 μm with the larger grain size of 13.9 μm, and the finer grains of 0.4 μm.

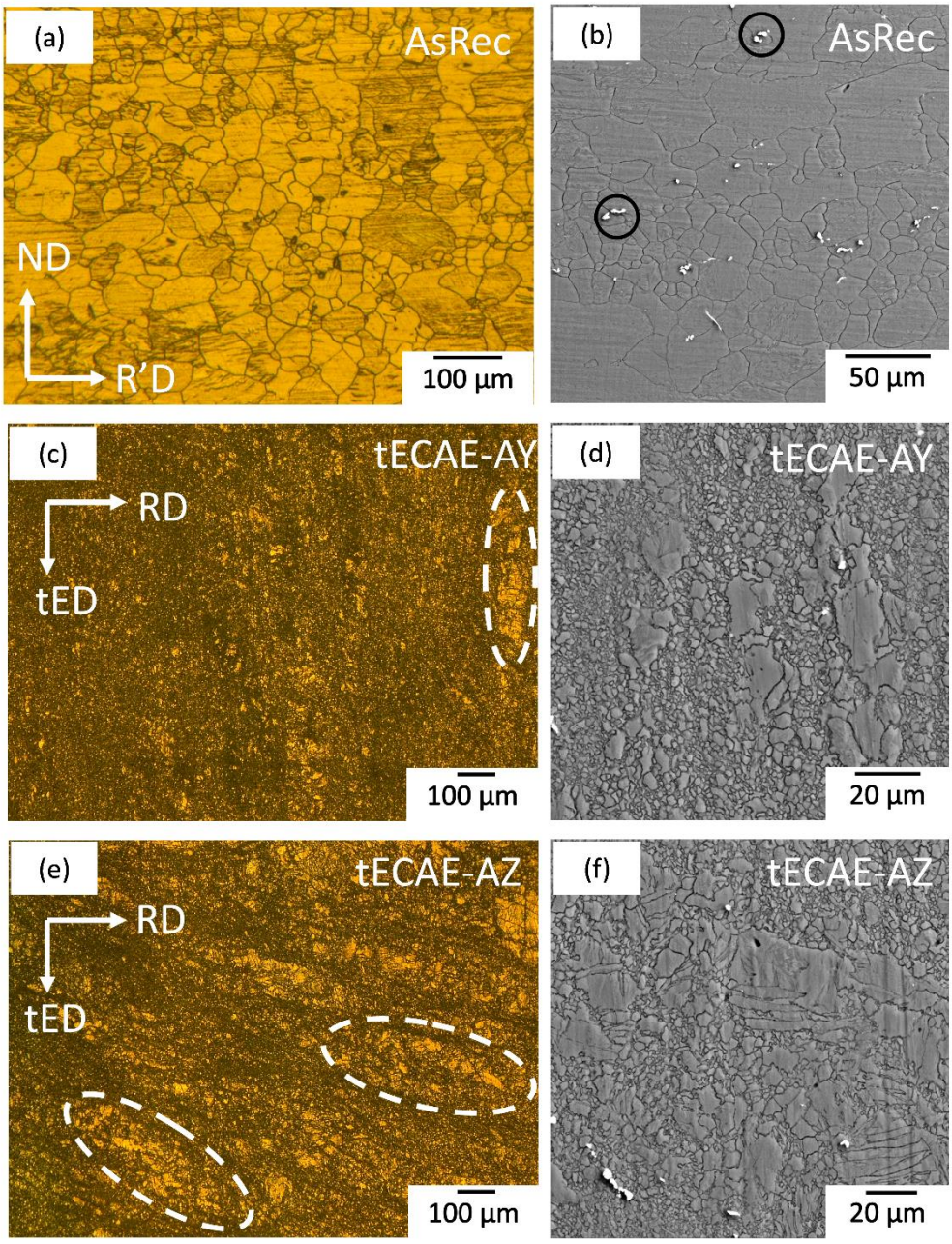

Figure 4.2 OM and SEM images of AsRec, and tECAE processed AY and AZ samples

The EBSD crystallographic texture results of the AsRec sample are shown in Figure 4.3. A typical rolled texture found in a hot-rolled AZ31 [108] with the c-axis

oriented towards the normal direction (ND) is seen. Although the material was annealed at 350 °C for 12 hours, it still exhibits the presence of a small fraction of twins as indicated in the band contrast map overlapped with special boundaries (see Figure 4.3(c)). Various twins that can possibly be present in Mg alloys are differentiated by measuring the misorientation angle of the c-axis with the $< 1\bar{2}10 >$ direction. The misorientation angle for $\{10\bar{1}2\}$ extension, $\{10\bar{1}1\}$ contraction, and $\{10\bar{1}1\} - \{10\bar{1}2\}$ double twins are 86° ± 5, 56° ± 5, 38° ± 5 respectively [109].

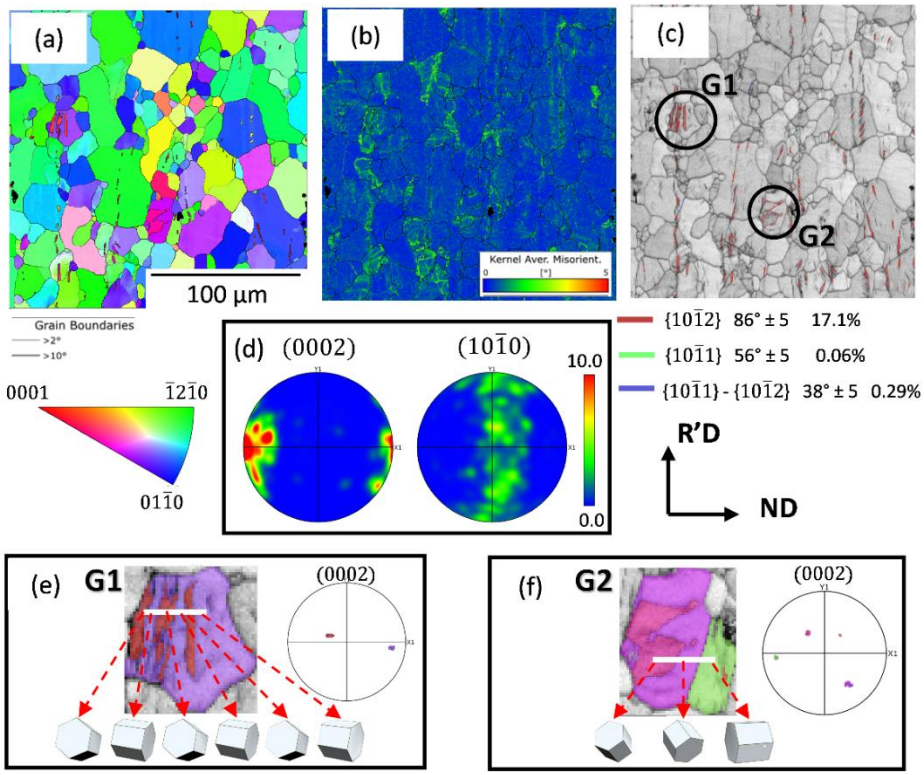

Figure 4.3 Texture results of the AsRec AZ31 sample (a) inverse pole figure map, (b) kernel average misorientation map, (c) band contrast map with twin boundaries, and (d) (0002) and $(10\bar{1}0)$ pole figures. (e) and (f) show Grain G1 and Grain G2 with twinned structures respectively.

Figure 4.3(c) shows a higher fraction of extension twins compared to other twin variants. To elucidate the reorientation caused by extension twins, unit cell orientations in grain G1 and G2 are shown in Figure 4.3(e) and (f). In G1, three twinned regions with similar extension twin variants are formed. The corresponding pole figure demonstrates the reorientation caused by extension twinning. The amount of twin fraction present is very small; hence its effect is not seen in the Figure 4.3(d) pole figure. Grain G2 shows the formation of sub-grains because of twinning.

The kernel average misorientation (KAM) map shows the internal residual strain in the grains. KAM of AsRec material shown in Figure 4.3(b) shows high strain concentrations near the twins and low angle grain boundaries.

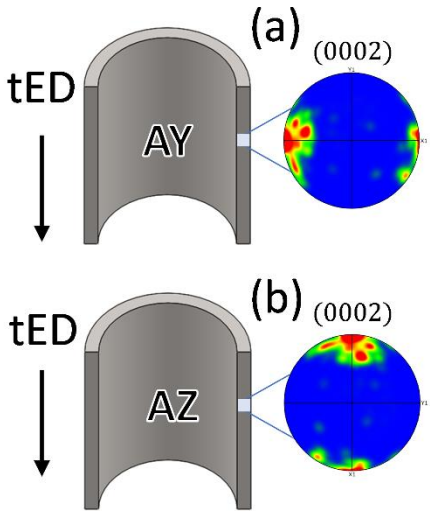

Figure 4.4 Starting texture for AY and AZ samples shown in (a) and (b) respectively before tECAE processing. Basal poles are orientated perpendicular to tED in AY whereas it is along tED in the AZ sample, before tECAE processing.

The starting textures for both the tECAE cases are shown in Figure 4.4. In the case of AZ, the basal poles are parallel to the tECAE direction whereas in AY, the basal poles are perpendicular to tECAE direction. This provides an opportunity to investigate the effect of starting texture, and texture evolution during tECAE processing. Note, it is not possible to perform conventional ECAE with the starting texture of AZ sample.

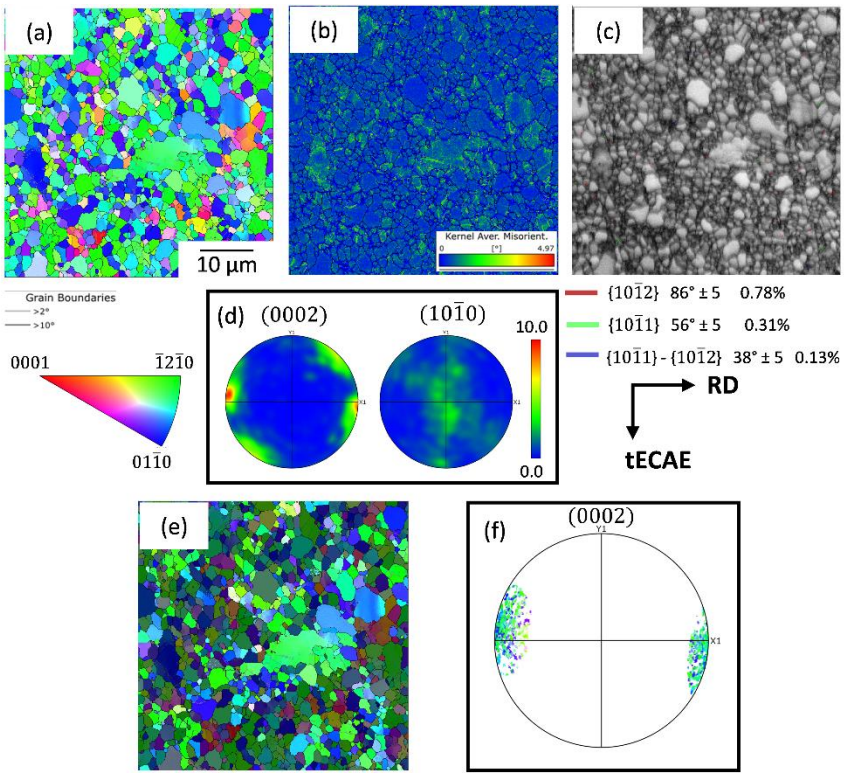

Figure 4.5 Texture results of the tECAE processed AY sample (a) inverse pole figure map, (b) kernel average misorientation map, (c) band contrast map with twin boundaries, and (d) (0002) and $(10\bar{1}0)$ pole figures. (e) shows the grain orientations of comparatively coarse grains and (f) shows the (0002) pole figure of the coarse gains.

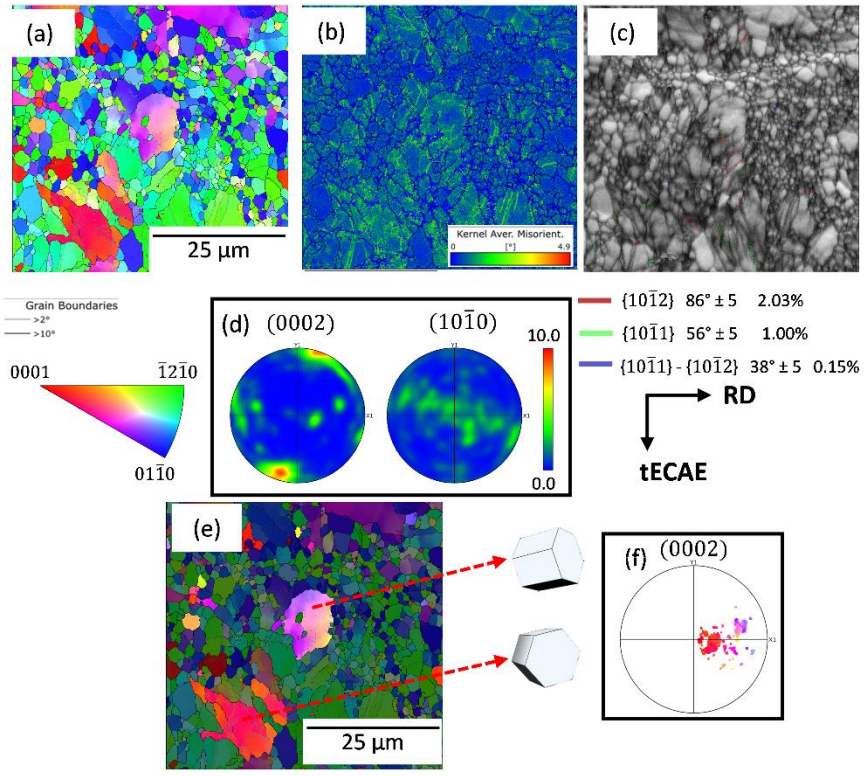

Figure 4.6 Texture results of the tECAE processed AZ sample (a) inverse pole figure map, (b) kernel average misorientation map, (c) band contrast map with twin boundaries, and (d) (0002) and $(10\bar{1}0)$ pole figures. (e) shows the grain orientations of comparatively coarse grains and (f) shows the (0002) pole figure of the coarse gains.

The texture results of the AY tube after tECAE are shown in Figure 4.5. Basal peak splitting is evident from the (0002) and $(10\bar{1}0)$ pole figures. A similar texture evolution was observed in AZ31 processed via route 2C of ECAE having similar starting texture [19]. After 2 passes of tECAE processing, a significant grain refinement is achieved, although the refinement is not uniform. The grains which did not undergo refinement, maintained its original orientation as observed in Figure 4.5 (e) and (f). Almost no twins are present in the microstructure which is expected as the slip system

accommodates the majority of deformation at 200 °C [45]. The KAM map shows high residual strain in the coarse grains and along low angle grain boundaries.

The texture evolution of tECAE processed AZ tube is shown in Figure 4.6. It is clear from the microstructure that grain refinement is less uniform than in the tECAE processed AY tube. The majority of the basal poles have rotated away from the tECAE direction by approximately 15 - 35°. These results indicate that the finer recrystallized grains are formed along the un-recrystallized coarse parent grains. The un-recrystallized coarse grains are analyzed separately as shown in Figure 4.6 (e) and (f). The basal poles of large un-recrystallized grains are oriented along the TD direction. The AY tube shows a comparatively more uniform microstructure than the AZ tube after tECAE.

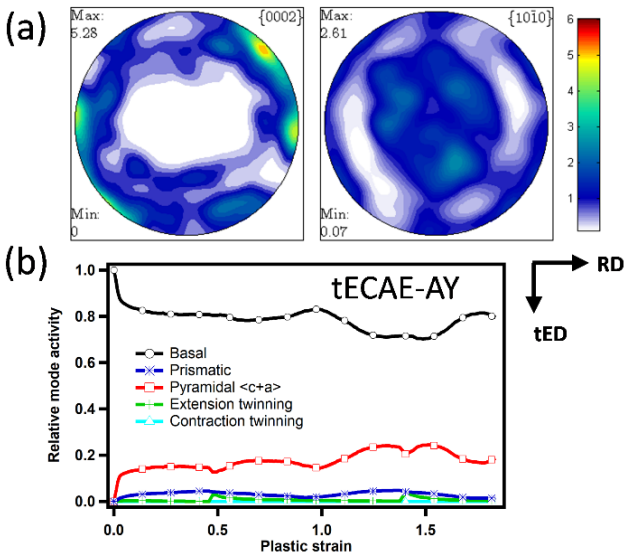

Figure 4.7 VPSC simulated pole figures and deformation mode activities for the AY sample after tECAE

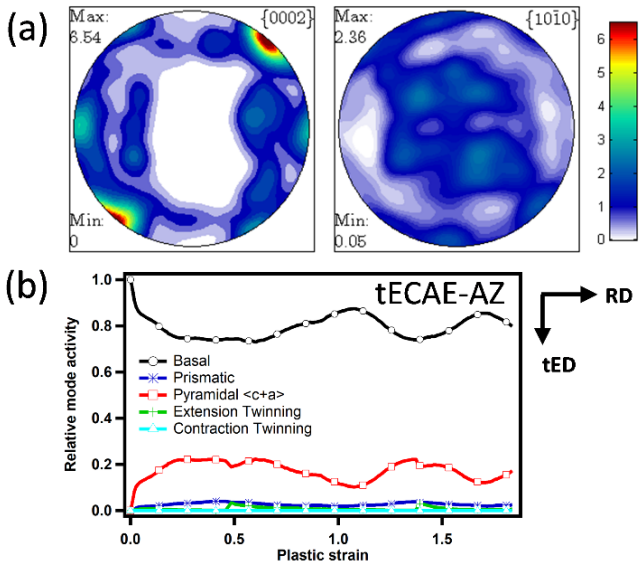

Figure 4.8 VPSC simulated pole figures and deformation mode activities for the AZ sample after tECAE

The VPSC model accurately predicted the texture results for the AY and AZ tubes. The predicted (0002) and $(10\bar{1}0)$ pole figures and deformation mode activities are shown in Figure 4.7 and 4.8. Activation of the basal and pyramidal $< c + a >$ slip systems was obtained for both the cases.

4.2.2 Mechanical properties

The hardness measurements obtained for the tECAE processed AY and AZ samples are plotted on a contour plot shown in Figure 4.9. A relatively homogenous hardness distribution is observed, showing that tECAE is an effective method of obtaining uniform mechanical properties.

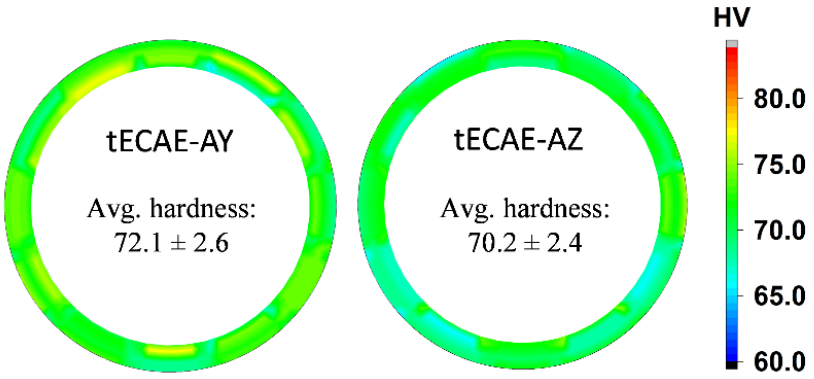

Figure 4.9 Contour plots of the Vickers hardness of tECAE processed AY and AZ samples. Relatively uniform hardness values were obtained across the cross-section of the tubes.

Table 4.1 Mechanical properties of AZ31 alloy in the as-annealed and tECAE condition compared with commercially made AZ31 tube under tension. (YS: yield strength, UTS: ultimate tensile strength, VH_{300} is Vickers hardness)

Sample	Orientation	0.2% YS (MPa)	UTS (MPa)	Elongation (%)	VH_{300}
AsRec	0° ND	62.8 ± 0.5	293.9 ± 1.5	11.5 ± 0.3	55.8 ± 3.0
	90° ND	180.3 ± 2.6	270.3 ± 0.1	9.2 ± 0.2	
tECAE-AY	tED	195.8 ± 0.2	327.9 ± 3.8	17.3 ± 1.4	72.1 ± 2.6
tECAE-AZ	tED	165.6 ± 12	289.6 ± 3.3	10.7 ± 1.8	70.2 ± 2.4
Commercial AZ31 tube	ED	200.4 ± 5.8	316.5 ± 5.8	9.9 ± 0.7	-

Table 4.1 shows the mechanical properties and the average Vickers hardness of AZ31 alloy before and after tECAE. The hardness increases after tECAE as expected. Uniaxial tension responses are shown in Figure 4.10. For the AsRec condition, a large variation between the 0° ND and 90° ND flow response is seen. The tECAE processed AZ sample has a yield strength slightly lower than the AsRec 90° ND sample and its

ductility also did not increase much whereas the AY sample shows significant improvement in ductility and strength. For comparison, an extruded commercial AZ31 tube was also tested.

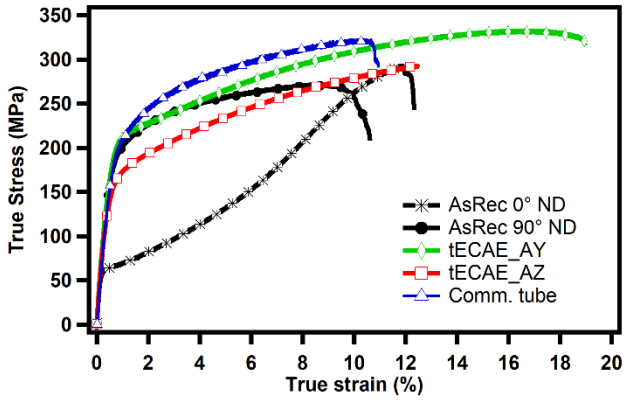

Figure 4.10 Room temperature tensile flow response of AZ31 after different processing conditions.

4.3 Discussion

4.3.1 Microstructure and texture

The microstructure of AsRec AZ31 shows a non-uniform grain size and the presence of a small fraction of twins. The grains are equiaxed with both coarse and fine grain structure. Even though the heat treatment was performed, all the extension twins were not eliminated. This could be due to incomplete recrystallization during the annealing process as the plate size was large and thick, probably limiting the core of the plate from reaching a high enough temperature for adequate time.

The tECAE processed AY and AZ tubes both show grain refinement, however, a difference in microstructure is observed. In the AY sample, the grains are more equiaxed

and do not show shear band formation, whereas, in the AZ sample, grains are slightly elongated and show shear band formation. The shear bands (circled with white broken lines in Figure 4.2) are formed at an inclination of about 45 - 50° from the tECAE direction (vertical) near the inside surface of the tube which increases to about 70 - 75° from the tECAE direction near the outer surface of the tube. A theoretical inclination angle calculated for one pass of conventional ECAE processing with a 90° deformation angle is 26.6° from the extrusion direction[110]. Additionally, the AY tube shows comparatively more homogenous grain size distribution than the AZ tube that has a higher fraction of coarse grains. Although, coarse grains exist in the tECAE processed AZ sample, they are finer than the starting grain size. It should be noted that the initial material also exhibits inhomogeneous grain size distribution with several coarse and fine grains in the microstructure. So, the grains are possibly refined from the initial size, but for a more uniform refinement, higher number of tECAE passes with more accumulated shear strain is needed.

Further, the difference is grain morphology is probably due to fewer dynamically recrystallized (DRX) grains in the AZ sample compared to the AY sample, which enables slip to cause grain elongation [19]. The KAM maps shown in Figure 4.5 and 4.6 for tECAE processed AY and AZ samples respectively show the amount of strain gradient present in the material. The strain gradient is less in the AY sample meaning that more DRX has occurred whereas in the case of the AZ sample, a higher strain gradient is seen, specifically in the coarse grains. This situation provides enough strain gradient to trigger continuous DRX (CDRX). Thus, the significance of the starting

texture in the SPD processing of Mg alloys is identified. Non-uniformity in the microstructure is also obtained in conventional ECAE studies performed on AZ31 as shown in refs [19, 21].

The texture obtained in the AY and AZ tubes is a result of 2 passes of tECAE processing. The tECAE processed AY tube shows basal peak splitting. Grains that did not undergo refinement maintained the initial texture whereas the refined grains are rotated by 40 - 60° away from the initial orientation, resulting in basal poles being 30 - 50° away from the tED direction. This confirms the role of shear direction for texture change. Similar basal poles split have been observed in other studies performed on Mg alloys [19, 111, 112]. Such texture evolution is attributed to the activation of the $< c + a >$ slip system. In other studies, such a tilt of basal poles has been attributed to the double twinning mechanism [113]. Since in this study the processing was performed at elevated temperatures, the pyramidal $< c + a >$ slip system activated along with basal slip to accommodate the deformation. This is further confirmed by the activities results from the VPSC simulation shown in Figure 4.7 which depicts the basal slip to be the most active mode followed by pyramidal $< c + a >$ slip. This is expected as temperature-sensitive slip mechanisms are preferentially activated at 200 °C [44]. Pyramidal slip system accommodates deformation along the c-axis at this elevated temperature. An almost negligible amount of twinning activities exists. The few twins that are observed are formed mostly in the coarse grains where twin growth is easier than twin nucleation.

Texture evolution in the tECAE processed AZ sample is shown in Figure 4.6. Tilting of basal poles by 15-35° away from the tECAE direction, towards the shear direction, again depicts the role of shear direction. The VPSC results shown in Figure 4.8 accurately predict the texture evolution. While the split basal peaks show almost equal intensity in the AY sample, the AZ sample's pole figure shows more tilting than peak splitting, with less intensity of the basal peaks observed along the radial direction (RD). It is important to note here that the texture obtained after tECAE processing of both AY and AZ tubes approaches a similar grain orientation and are significantly influenced by the shear direction. Hence, more passes of tECAE could lead to the development of unique axisymmetric textures in Mg alloys showing reduced asymmetry in mechanical properties. Additionally, the texture developed after tECAE is significantly different from the conventionally extruded tubes in which strong basal textures form perpendicular to the extrusion direction [114]. Development of such a unique and weakened basal texture provides an opportunity to achieve enhanced mechanical and physical properties in Mg alloys.

4.3.2 Evolution of mechanical properties

The microhardness of tECAE processed materials are higher than in the AsRec condition due to the difference in grain size as per Hall-Petch strengthening [56]. The hardness distribution, after tECAE process, is quite uniform as shown in Figure 4.9. This confirms a homogenous strain distribution through the thickness of the tube providing circumferential uniformity. Other tools designed to process tubes have shown variability in the strain distribution [115, 116].

The tensile test responses are presented in Figure 4.10. The two orientations of AsRec samples, namely, 0° ND and 90° ND show a noticeable difference in their tensile flow response which is expected and attributed to a difference in texture [117]. The 0° ND sample shows the highest strain hardening. In this case, the basal poles are oriented along the ND, hence, c-axis extension takes place during tensile deformation, leading to activation of basal slip and extension twinning. During the initial deformation, the extension twins reorient the grains to 86° away from the tension axis [53, 117]. This reorientation makes the grains favorably oriented for hard non-basal prismatic slip to activate, resulting in strain hardening [25]. The twin boundaries limit dislocation motion inside the twins, causing strain hardening at the later stages of deformation [104]. In contrast, for the 0° ND sample, the c-axis is perpendicular to the tension axis, hence, deformation should occur via prismatic slip based on the grain orientation [25]. It is known that prismatic slip cannot accommodate c-axis compression, therefore, either contraction twins or pyramidal slip system activates. Since the critical resolved shear stress (CRSS) for pyramidal slip is temperature dependent and is high at room temperature [44], it is plausible to assume that contraction twins are activated in this case. The strain hardening shown in 0° ND sample is less than the 90° ND sample because the reorientation caused by contraction twins is 56° which is lower than that for extension twins, hence comparatively softer twin mechanisms are active. Also, extension twins can form inside contraction twins, forming double twins which causes a reorientation of 38° which further facilitates activation of basal slip system [25, 53, 54, 117].

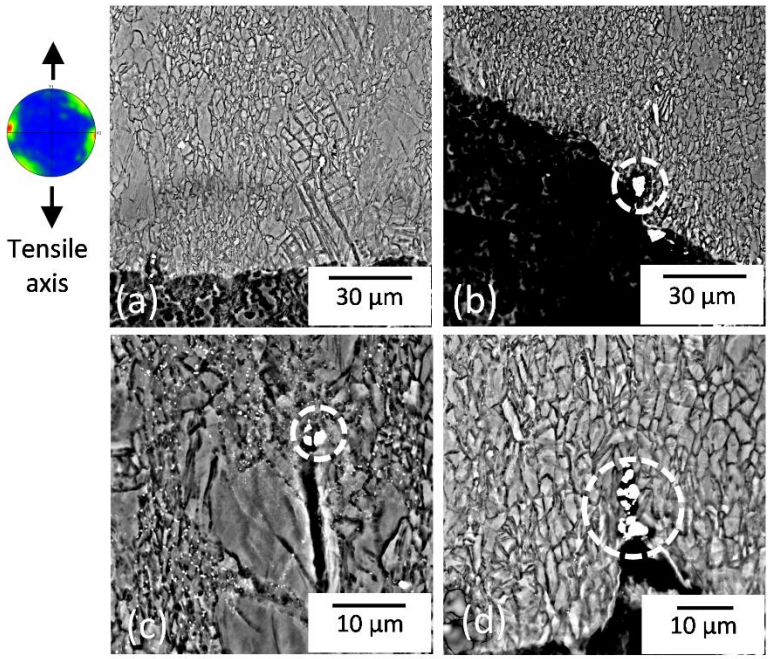

Figure 4.11 SEM images of a fractured surface after tensile loading on the tECAE processed AY sample. The basal (0002) pole figure is provided for reference. The white dotted circled regions indicate secondary Al_8Mn_5 particles.

Figure 4.10 also shows the tensile flow response of tECAE processed samples, and commercially produced tube for comparison. A large improvement in the ductility of tECAE processed AY material can be seen, whereas the AZ sample shows only a modest improvement in ductility. Both AZ and AY tECAE processed materials have a smaller grain size, which is generally expected to give a higher strength in the material [56]. In the case of Mg alloys, not only grain size, but texture play a major role in determining the mechanical properties. In order to understand the deformation modes active, and failure mechanisms of the tECAE processed tensile specimens, microstructure along the gage length near the fracture surface were prepared and observed under SEM and optical

microscope. Attempts were made to obtain EBSD texture but due to the high strain in the material, indexing could not be done. We were able to obtain EBSD maps of extruded commercial AZ31 material probably because it has a large grain size.

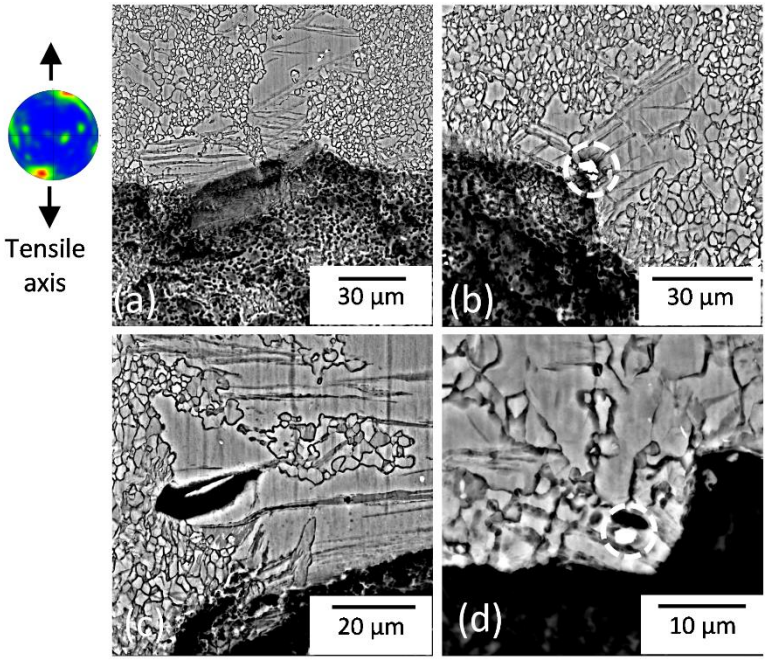

Figure 4.12 SEM images of the fracture surface after tensile tests on the tECAE processed AZ sample. A basal (0002) pole figure is provided for reference. The white dotted circled regions indicate the secondary Al_8Mn_5 particles.

In general, the void formation observed in the AZ31 material can be categorized as two types: (V1): voids at the second phase particles and (V2): voids formed away from second phase particles. The formation of both types of voids is evident from the microstructure of the tECAE processed and tensile tested AY and AZ samples. Figure 4.11 shows the tECAE processed AY sample's fractured surface. Elongated grains, with

a few coarse grains can be seen. A complicated network of twins can also be observed in the samples, specifically in the coarse grains. The nucleation of large voids occurs from the twinned region and it has been shown by Azghandi et. al. [118] that coarse grains provide a comparatively easy path for void growth. The analysis of the deformation mechanism active can be performed looking at the texture developed after tECAE processing. The split basal peaks favor activation of both basal and prismatic slip. The fact that most of the grains are elongated along the tension direction, shows that this is a slip-dominated deformation. Still, both these slip systems cannot accommodate deformation along the c-axis, hence, activation of either pyramidal slip or twinning system is possible. Therefore, the twins formed in the AY sample tensile test could be extension or contraction or double twins. The activity of twins means that pyramidal slip was not activated to accommodate deformation. In contrast, the AZ sample did not show grain elongation. The AZ sample has a large fraction of coarse grains which provide an easier path for void growth, leading to early failure.

On comparing the tensile flow response of AY and AZ with that of an extruded commercial AZ31, we see that the yield strength of the tECAE processed AZ is lower than that of commercial AZ31 tube whereas the ductility is similar. For tECAE processed AY, the yield strength is similar to commercial AZ31 tube, but the ductility is greater. The deformation behavior of commercial AZ31 is analyzed and the microstructure along with inverse pole figure maps, pole figures, and grain misorientation are shown in Figure 4.14. From the SEM images, the formation of a high fraction of twins is seen. EBSD results confirm the formation of a high fraction of

double twins. The maxima obtained in the range of 5-10° misorientation with the $< 1\bar{2}10 >$ axis could show either low angle grain boundaries or twinning of grains or both. In the present situation, grains twinning has the higher possibility. The local maxima obtained with around 30-40° misorientation with the $< 1\bar{2}10 >$ axis shows the presence of $\{10\bar{1}1\} - \{10\bar{1}2\}$ double twins. In double twins, extension twins nucleate within contraction twins resulting in grain reorientation by 38°, and hence favor activation of soft basal slip. This results in strain incompatibility inside the twin, resulting in void formation and abrupt material failure.

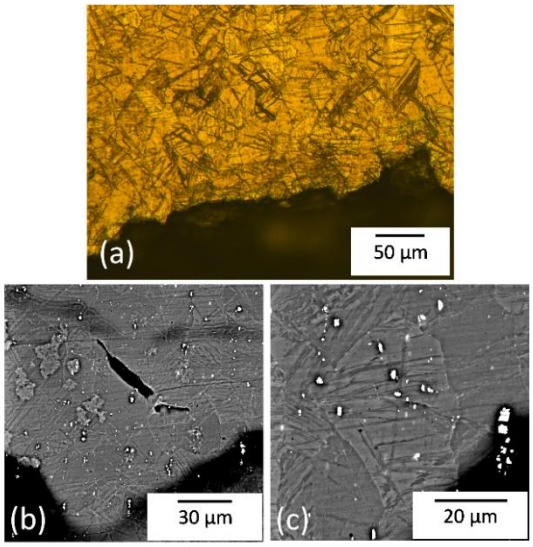

Figure 4.13 OM and SEM of the fractured surface along the extrusion direction after tensile testing on commercially manufactured AZ31 tube.

To sum up, the higher ductility in the tECAE processed AY material is due to: (1) The grain orientation in the AY sample promotes slip dominated deformation. (2)

More homogenously refined grains in the AY sample makes void growth difficult. It has been reported in ref. [118] that the void growth rate is higher in coarse-grained material than in fine-grained material. (3) Coarse grains lead to the formation of twins, which in turn leads to a concentration of stress at the twin boundaries, causing early failure.

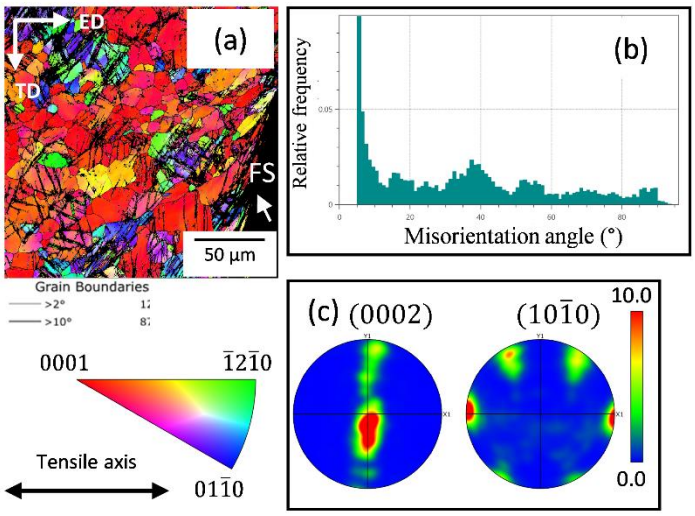

Figure 4.14 ESBD mapping results of tensile tested commercially manufactured AZ31 tube. (a) Inverse pole figure map, (b) misorientation angle distribution, and (c) (0002) and $(10\bar{1}0)$ pole figures

4.4 Summary

Two passes of tECAE at 200 °C was implemented in this study to process AZ31 alloy tubes having two different starting textures. Drastic grain refinement and changes in texture and mechanical properties were obtained after the tECAE process. The influence of texture change and grain refinement were clearly observed on the mechanical properties. The sample with basal poles being perpendicular to the tECAE direction showed the highest increase in strength and ductility. A uniform distribution of

microhardness was achieved after tECAE processing validating the fact that tECAE provides uniform grain refinement leading to improved mechanical properties throughout the tube.

The discussion of the failure mechanism confirms that the texture orientation in the AY material promotes slip dominated deformation, providing better ductility. A comparison of mechanical properties was made with commercial AZ31 tube which confirms that tECAE indeed improves the mechanical properties of Mg alloy tubes.

CHAPTER V

EVOLUTION OF MICROSTRUCTURE, TEXTURE, AND STRENGTH OF MG-3AL-1ZN ALLOY BY HYBRID PROCESSING USING ECAE PLUS TECAE

The previous Chapter IV investigated the role of two different starting textures on mechanical properties and processability via tECAE. The improvement in mechanical properties obtained, specifically from one texture orientation, influenced the action to investigate the effect of other unique starting textures. Therefore, in this chapter, a hybrid SPD processing route for tubular forms of AZ31 alloy at 200 °C is investigated. This combination of ECAE and a following tECAE process is investigated here. The objectives of this study are:

1. To examine the scale-up capability of ECAE for processing large bars of Mg alloys. It is expected that ECAE processing will provide homogenous grain refinement irrespective of the workpiece size.
2. To provide a unique starting texture for tECAE processing, different from that reported in Chapter IV.
3. To determine the influence of the combined ECAE plus tECAE on the mechanical properties of AZ31.

5.1 Materials and Methods

The AZ31 alloy plate used in this study is the same that was used in Chapter IV and received the same pre deformation heat treatment. The details about the plate dimensions and heat treatment can be found in Chapter IV. After the heat treatment, two

bars, namely Bar-1 and Bar-2 of dimensions 5 x 5 x 25 cm^3 each were sectioned from the plate with the long side of the bars being along the plate rolling direction. Bar-1 and Bar-2 were ECAE processed at 200 °C through a tool having a sharp 90° deformation angle in a sliding wall tool via four passes of route A and B_C respectively and quenched after each pass to retain the microstructure. Note that all the ECAE passes were conducted without the application of back-pressure. Magnesium alloys ECAE processed without back-pressure have a tendency to shear localize or form large cracks on the sample surface even at elevated temperature processing [119, 120]. Such shear localization did not occur in the current study.

Table 5.1 Description of sample processing and sample labels. ED, FD, and LD show extrusion direction, flow direction, and longitudinal direction; 2 passes here means one expansion step followed by one contraction step.

Sample label	Processing
AsRec	Initial material after heat treatment.
4A	4 passes of ECAE via route A
$4B_C$	4 passes of ECAE via route B_C
4A-tECAE-ED	Tube cut from 4A bar with tube axis along ED followed by 2 passes of tECAE
4A-tECAE-FD	Tube cut from 4A bar with tube axis along FD followed by 2 passes of tECAE
4A-tECAE-LD	Tube cut from 4A bar with tube axis along LD followed by 2 passes of tECAE
$4B_C$ -tECAE-ED	Tube cut from $4B_C$ bar with tube axis along ED followed by 2 passes of tECAE
$4B_C$ -tECAE-FD	Tube cut from $4B_C$ bar with tube axis along FD followed by 2 passes of tECAE
$4B_C$ -tECAE-LD	Tube cut from $4B_C$ bar with tube axis along LD followed by 2 passes of tECAE

ED: extrusion direction; FD: flow direction; LD: Longitudinal direction

Both the ECAE processed bars were used as the starting material for tECAE processing. Tubes having an outer diameter 38 mm, wall thickness of 3 mm, and length of 25 mm were obtained using wire electro-discharge machine (EDM) from three different orientations of the bar as shown in Figure 5.1. The descriptions of all the

samples used are shown in Table 5.1. All the tubes were tECAE processed through a tool having 135° deformation angle at 200 °C via 2 passes (expansion and contraction) and subsequently water quenched. An even number of passes through the tECAE process ensures that the tube regains its original dimensions. During both ECAE and tECAE processing, the workpiece was wrapped in Teflon sheet which acted as lubricant. The shear strain applied during ECAE processing is 1.15 per pass, whereas the shear strain applied during tECAE process is calculated to be 1.05 per pass. Therefore, the total accumulated strain in the tubes after 4 passes of ECAE and 2 passes tECAE processing is 6.7 each.

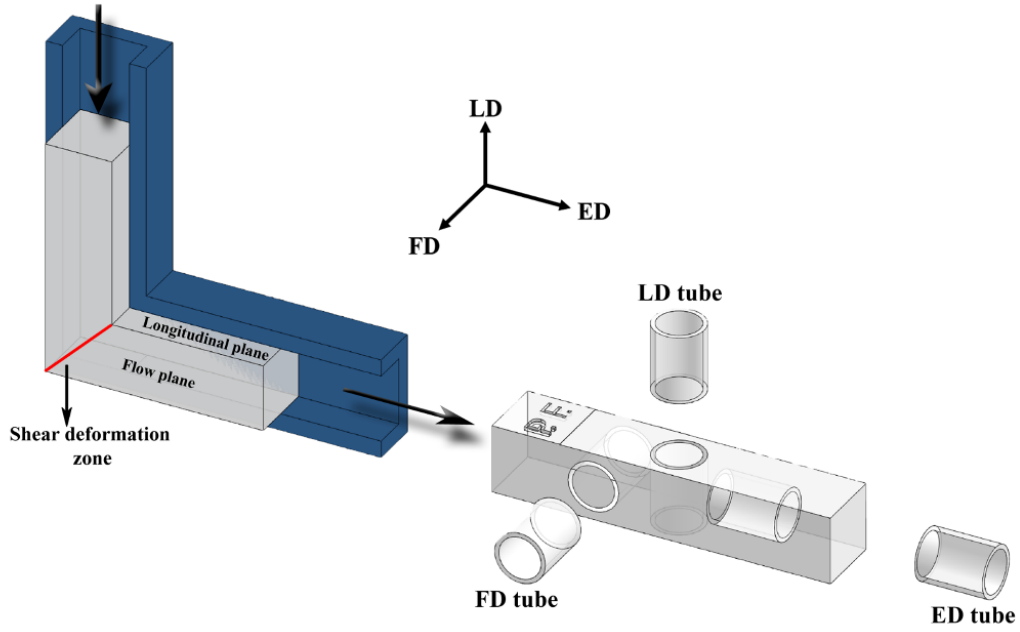

Figure 5.1 Schematic of ECAE and tubes sectioned from ECAE processed bar. P.F. designates the punch face, where the punch pushes the bar into the ECAE inlet channel.

The sample preparation and post-processing technique for microstructure and texture analysis were the same as used in Chapter IV, therefore it is not repeated here for the sake of brevity. For mechanical property analyses, tension tests and Vickers hardness measurements were taken, the procedures of which are discussed in previous chapters. For the ECAE processed materials, tension specimens were obtained from the ED, FD, and LD orientations (refer to Figure 5.1 for axes notation), whereas, for the tECAE processed material, all the tension specimens were obtained from tED orientation. Vickers hardness measurements were taken on the transverse plane of AsRec sample, from the tangential plane of tECAE processed samples, and from all the three planes of ECAE processed material. At least 10 measurements were taken on each. The Vickers hardness values are given in Table 5.2.

Table 5.2 Grain size, tensile test, and microhardness results of AZ31 alloy processed via various routes.

Sample	Orientation	Average Grain size (μm)	0.2 % YS (MPa)	UTS (MPa)	% Elongation	VH_{300}
AsRec	0° ND	10.8 ± 9.9	62.8 ± 0.5	293.9 ± 0.3	11.5 ± 0.3	55.8 ± 3.0
	90° ND		180.3 ± 2.6	270.3 ± 0.1	9.2 ± 0.2	
4A	ED	2.3 ± 1.4	219.9 ± 3.6	327.0 ± 0.3	14.4 ± 0.8	66.0 ± 2.0
	FD		242.8 ± 4.7	322.2 ± 3.8	14.0 ± 1.2	
	LD		130.4 ± 0.5	325.0 ± 2.5	15.4 ± 0.8	
$4B_C$	ED	1.5 ± 0.9	114.6 ± 3.3	280.5 ± 1.0	19.9 ± 0.8	70.9 ± 1.1
	FD		200.7 ± 3.3	320.4 ± 10.2	12.9 ± 4.3	
	LD		108.5 ± 3.4	253.9 ± 3.6	14.7 ± 0.8	
4A-tECAE-ED	tED	1.5 ± 0.9	126.8 ± 5.8	311.5 ± 6.4	17.6 ± 0.5	68.5 ± 1.8
4A-tECAE-FD	tED	2.3 ± 1.4	247.7 ± 0.7	321.5 ± 0.1	13.8 ± 0.9	72.9 ± 1.05
4A-tECAE-LD	tED	1.8 ± 1.2	146.3 ± 3.7	301.9 ± 7.3	14.0 ± 0.8	72.0 ± 1.0
$4B_C$ -tECAE-ED	tED	1.9 ± 0.8	185.0 ± 25.2	328.0 ± 0.8	15.7 ± 3.6	69.9 ± 1.0
$4B_C$ -tECAE-FD	tED	1.8 ± 1	161.7 ± 5.0	316.9 ± 14.3	15.7 ± 2.9	68.13 ± 0.7
$4B_C$ -tECAE-LD	tED	1.4 ± 0.7	181.7 ± 2.5	325.0 ± 13.9	16.3 ± 5.2	71.5 ± 1.2

5.2 Results

5.2.1 Microstructure and texture evolution

The microstructure and texture of AsRec material are shown in Figure 4.2 (a) and (b) and Figure 4.3 respectively of Chapter IV. Figure 5.2 shows the microstructure in the as-worked conditions. Much finer grains were formed after the SPD processing. The average grain sizes are shown in Table 5.2 for all conditions. While a drastic reduction in the grain size is achieved after 4 passes of ECAE as expected, the grain refinement in $4B_C$ is slightly higher than that in the 4A specimen. The grain size of the tubes processed via tECAE after ECAE processing do not show much further refinement. In all the cases, a homogeneous equiaxed fine grain structure is achieved after the two stages of SPD, with a very few relatively coarse grains distributed sporadically in the microstructure.

The crystallographic texture results measured via EBSD for the as-worked material are presented in Figures 5.3-5.9. The following information is reported here: inverse pole figure maps, kernel average misorientation (KAM) maps, band contrast with overlaying twin boundary maps, and (0002) and $(10\bar{1}0)$ pole figures. The SPD processing caused significant changes in the texture.

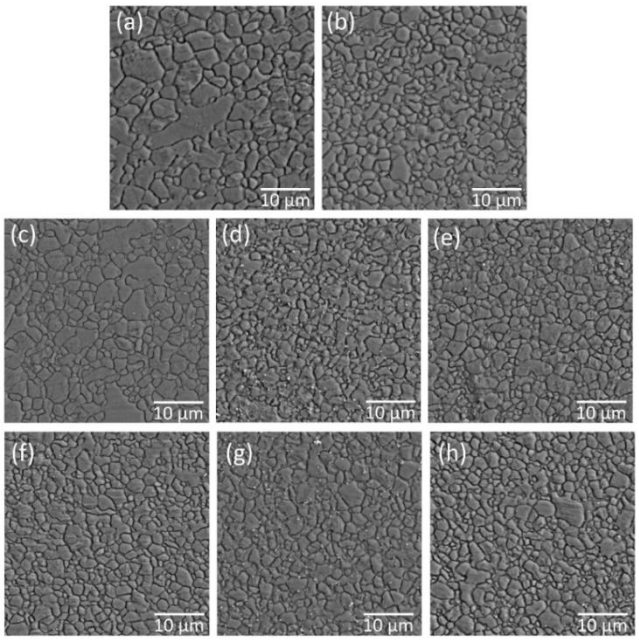

Figure 5.2 SEM images of as-worked AZ31 samples (a) 4A ECAE (b) $4B_C$ ECAE. (c), (d), and (e) are 4A ECAE followed by 2 passes of tECAE processed ED, FD, and LD tubes respectively. (f), (g), and (h) are $4B_C$ ECAE followed by 2 passes of tECAE processed ED, FD, and LD tubes respectively.

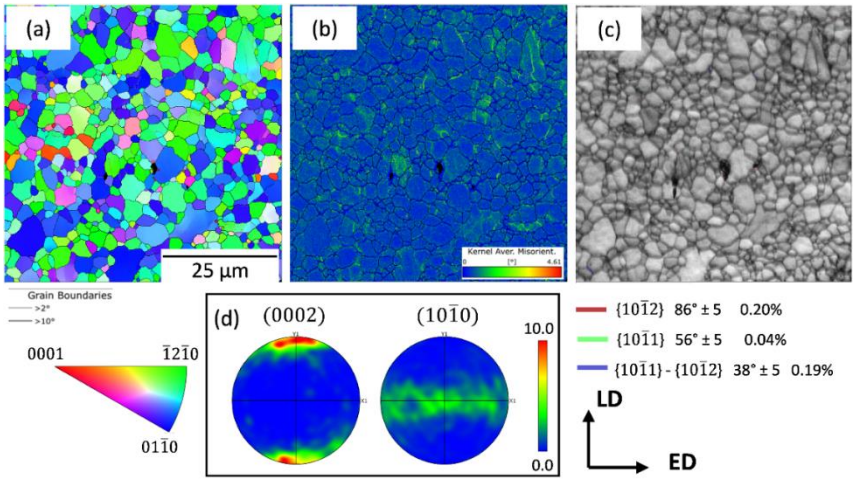

Figure 5.3 Texture results of 4A ECAE processed sample: (a) inverse pole figure map, (b) kernel average misorientation map, (c) band contrast map with twin boundaries, and (d) (0002) and $(10\bar{1}0)$ pole figures.

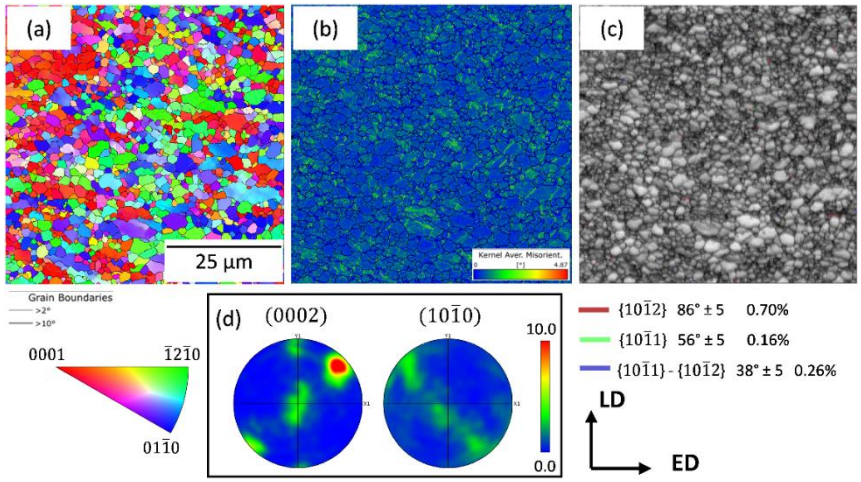

Figure 5.4 Texture results of $4B_C$ ECAE processed sample: (a) inverse pole figure map, (b) kernel average misorientation map, (c) band contrast map with twin boundaries, and (d) (0002) and $(10\bar{1}0)$ pole figures.

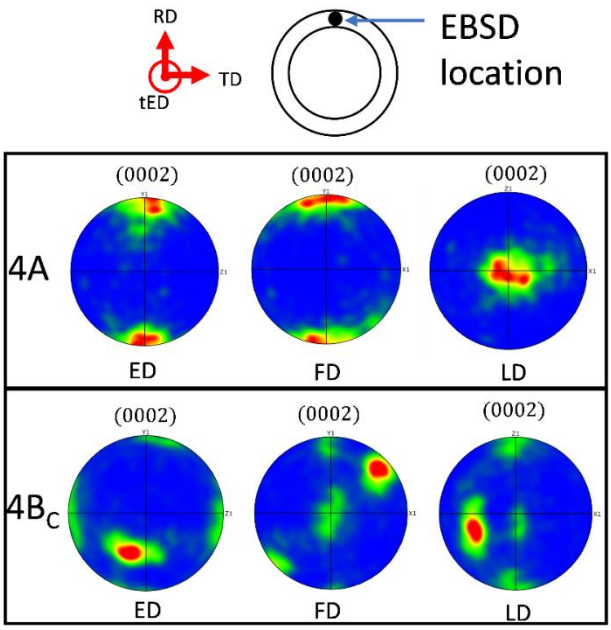

Figure 5.5 The basal pole orientations after ECAE and before tECAE. This is the starting orientation for tECAE processing for tubes cut from different orientations.

Figure 5.3 shows the texture evolution after 4A processing. The basal poles are spread around LD with an angle of 20°. Negligible fractions of twins were formed as seen in the band contrast map (Figure 5.3(c)). The texture evolution after $4B_C$ processing is shown in Figure 5.4. The basal poles are rotated by 45° away from the ED in this case. While the texture evolution after 4A ECAE processing is similar to that pre tECAE texture of AZ sample in Chapter IV, the $4B_C$ route provides a unique starting texture for further tECAE processing.

The texture evolution after ECAE plus tECAE process was also investigated. The starting texture for tECAE processing for all the tube orientations are shown in Figure 5.5. Figure 5.6 (a)-(d) present the texture results for 4A-tECAE-ED from the tEP, which is the plane perpendicular to the tube extrusion direction. Most of the basal poles show an inclination of 15-30° away from the tED and towards the RD. Similar texture results have been obtained for the AZ samples that were directly tECAE processed from the plate and are discussed in Chapter IV.

The texture evolution of 4A-tECAE-FD specimen is illustrated in Figure 5.6 (e)-(h). The texture change in this case is slightly less than that observed for the 4A-tECAE-ED case. For the 4A-tECAE-LD case, drastic texture changes were observed as shown in Figure 5.7. In this case, the presence of randomly oriented coarse grains can also be seen which can skew the texture results, hence pole figures are also obtained by excluding these coarse grains to get more representative texture. Weakened basal poles and a more randomized grain orientations are observed in this case.

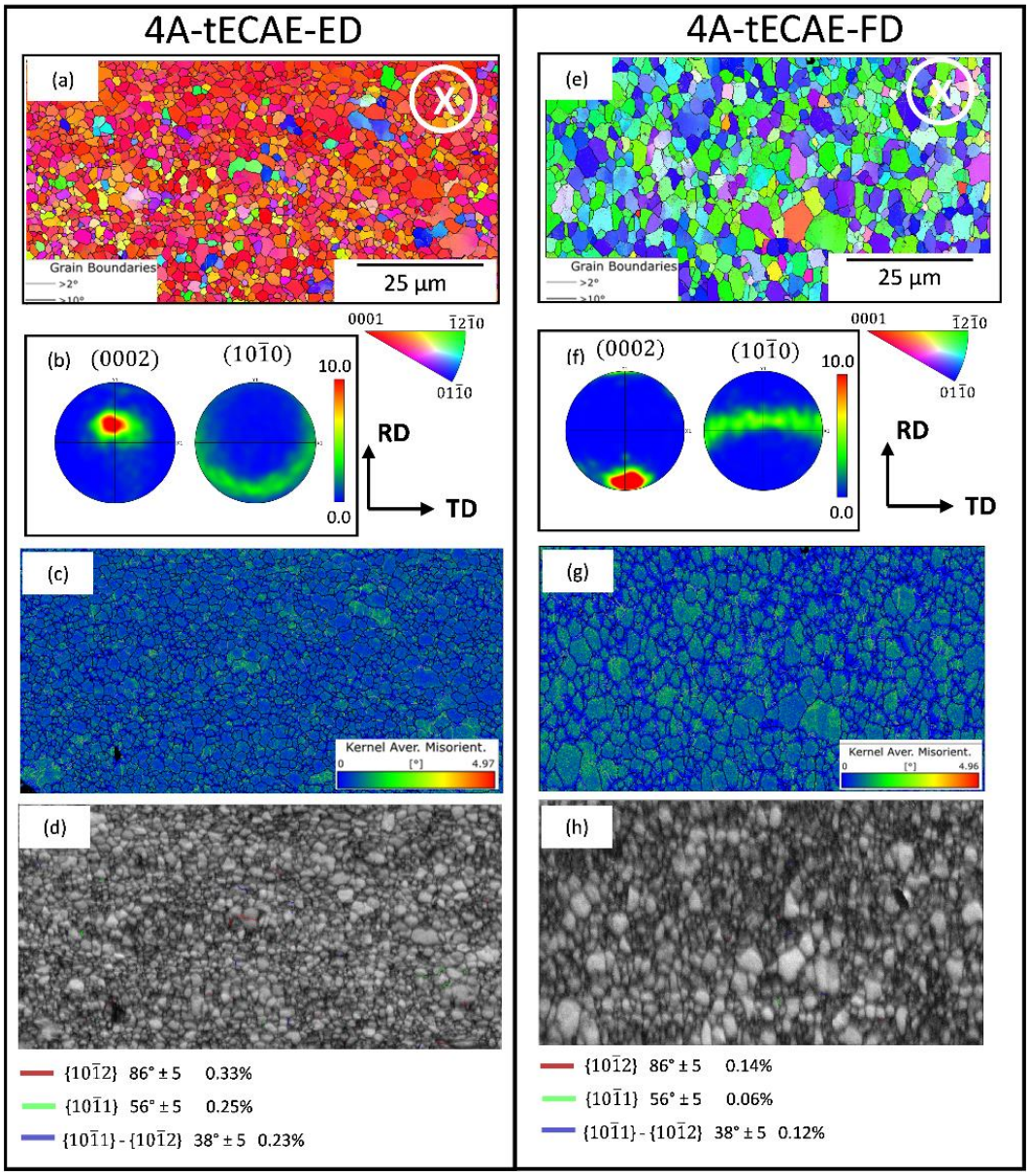

Figure 5.6 Texture results of 4A-tECAE-ED is shown in (a) - (d) and those of 4A-tECAE-FD are shown in (e)-(h). (a) and (e) show the inverse pole figure maps with tED into the plane; (b) and (f) show the (0002) and $(10\bar{1}0)$ pole figures; (c) and (g) represent the kernel average misorientation maps; (d) and (h) show band contrast maps with twin boundaries.

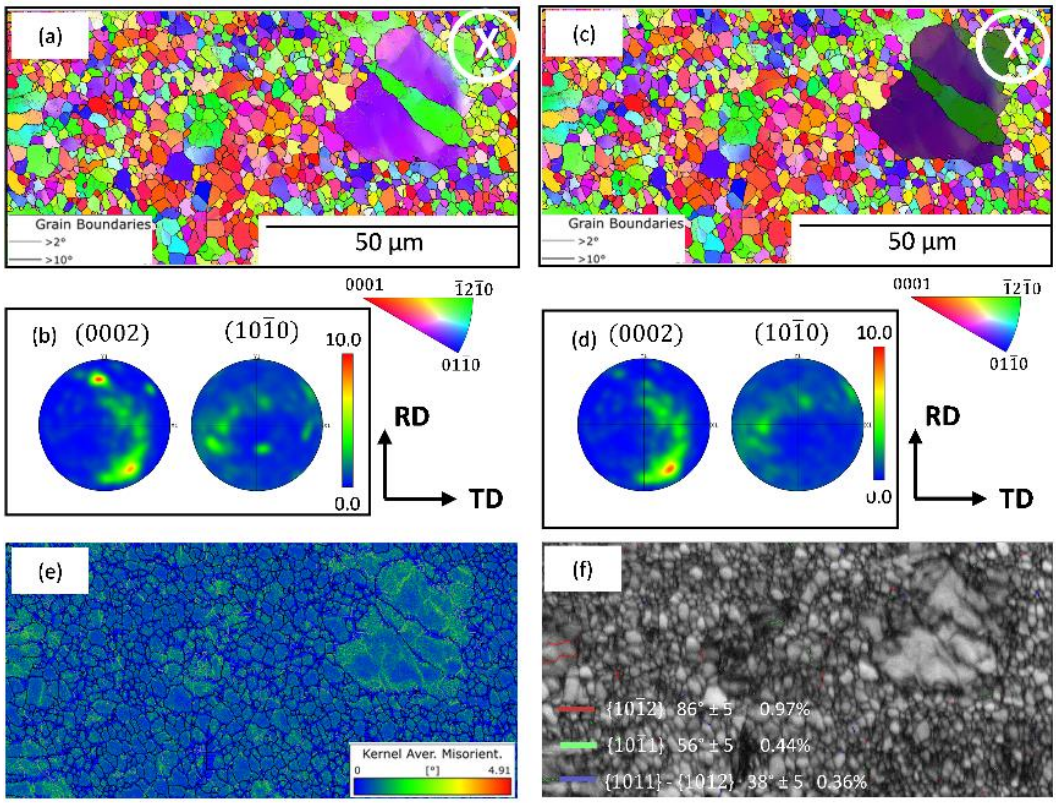

Figure 5.7 Texture results of the 4A-tECAE-LD sample: (a) and (c) are the inverse pole figure maps with and without coarse grains respectively; (b) and (d) are the (0002) and (10$\bar{1}$0) pole figures with and without coarse grains respectively; (e) is the kernel average misorientation map; (f) is the band contrast map with twin boundaries.

The texture evolution after tECAE processing $4B_C$ processed ED tube is depicted in Figure 5.8 (a) – (d). It is interesting to note that some of the grains have their basal poles oriented toward the tED orientation while some grains have their basal poles perpendicular to the tED direction. This results in enhanced mechanical properties as discussed in the next section.

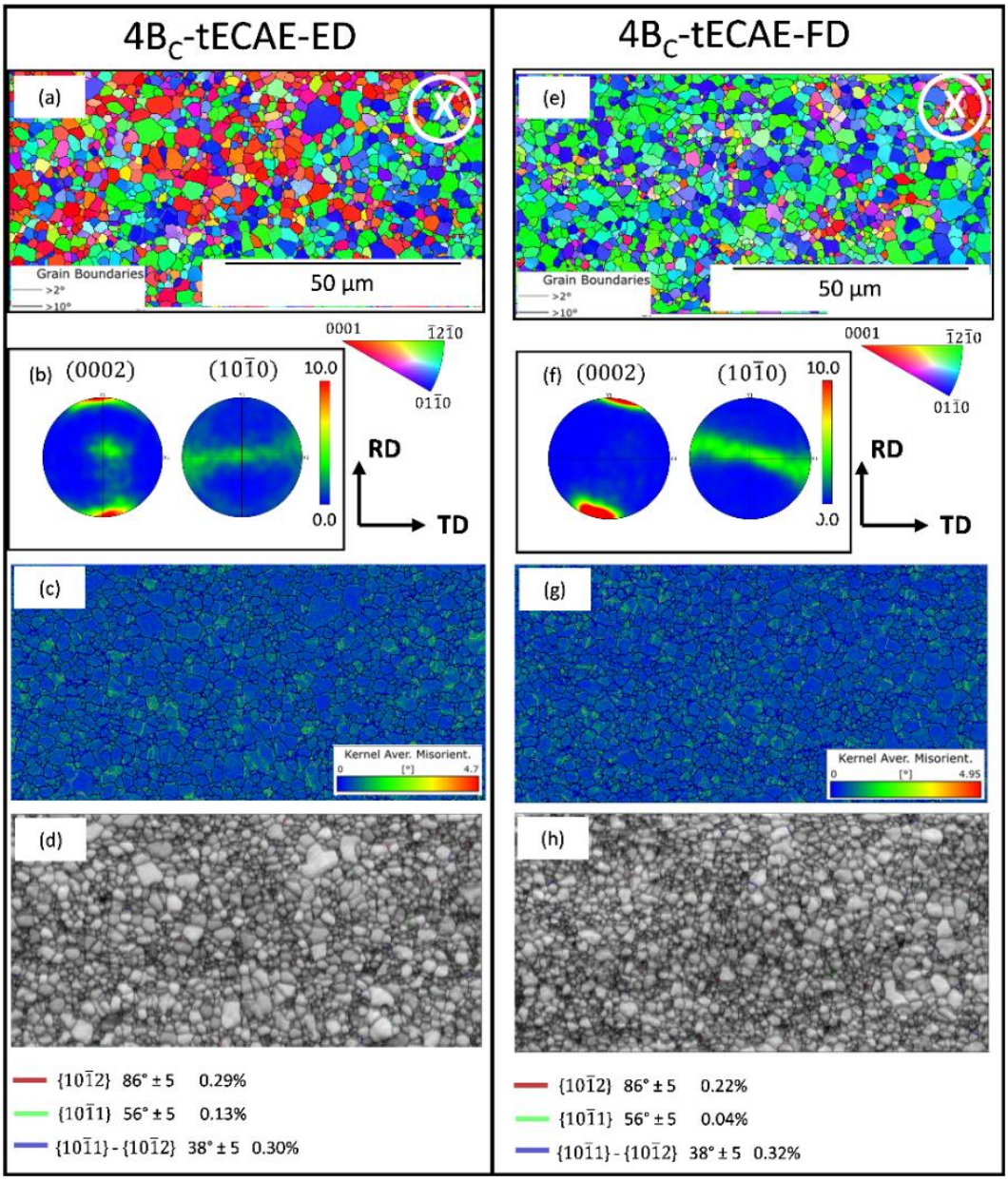

Figure 5.8 Texture results of 4BC-tECAE-ED is shown in (a) - (d) and that of 4BC-tECAE-FD is shown in (e)-(h). (a) and (e) show the inverse pole figure maps with tED into the plane; (b) and (f) show the (0002) and $(10\bar{1}0)$ pole figures, (c) and (g) represent the kernel average misorientation maps; (d) and (h) show band contrast maps with twin boundaries.

For the $4B_C$-tECAE-FD case (see Figure 5.8 (e)-(h)), the basal poles are inclined away from the tED orientation and tilted by ~ 15 - 30° away from RD. Similar texture results are obtained for the $4B_C$-tECAE-LD specimen as shown in Figure 5.9.

The KAM plots shown in all the cases show a strain gradient in different grains. Coarse grains and low angle grain boundaries have high strain compared to their surroundings. Additionally, band contrast maps are shown along with twin boundaries. In all the cases, a negligible amount of twin formation was seen.

5.2.2 Evolution of mechanical properties

The tensile flow responses of the as-worked samples are shown in Figure 5.10 and 5.11. The strength and elongation values along with Vickers hardness are presented in Table 5.2. Mechanical response of the AsRec sample is discussed in previous chapters, hence it is not repeated here. The UTS and elongation of the three orientations from the 4A material are similar, but a difference in yield strengths is apparent.

Among the samples that were further tECAE processed after 4A, 4A-tECAE-ED shows the highest ductility. The tensile strengths of tECAE processed materials are again comparable with each other, while being slightly lower than the 4A processed material. The yield strengths after tECAE processing are higher for all the cases when compared with respective orientations of 4A processed material, except for the 4A-tECAE-ED condition. For $4B_C$ samples, ED has the highest ductility followed by LD and FD respectively (refer to Figure 5.11 and Table 5.2). The yield strengths of ED and LD are similar while it is higher for the FD orientation. Additionally, $4B_C$ FD shows the highest tensile strength.

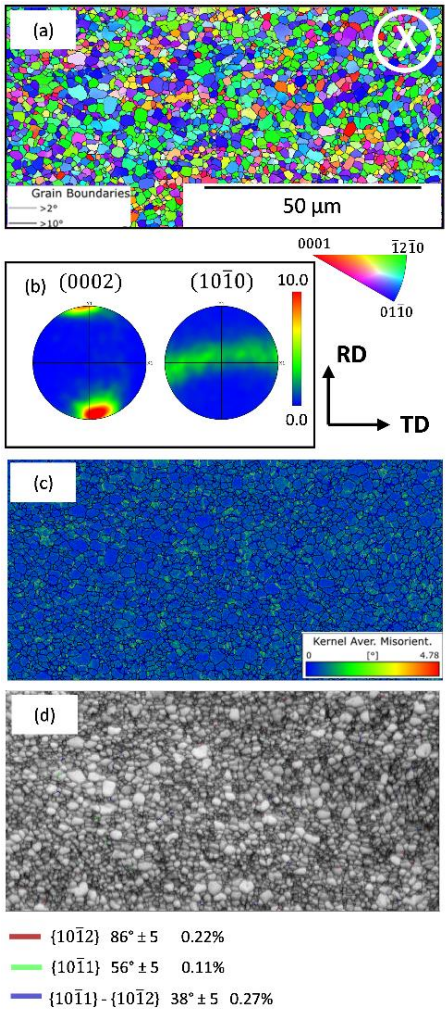

Figure 5.9 Texture results of 4B$_C$-tECAE-LD sample: (a) inverse pole figure map, (b) (0002) and (10$\bar{1}$0) pole figures, (c) kernel average misorientation map, and (d) band contrast map with twin boundaries.

The samples that were further tECAE processed after 4B$_C$, 4B$_C$-tECAE-LD have the highest ductility while the tensile strengths are similar in all the cases (see Figure 5.11). The variation in yield strength is less after tECAE when compared to only 4B$_C$ processed material. Overall, the tensile behavior of as-worked materials shows substantial improvement over the starting material.

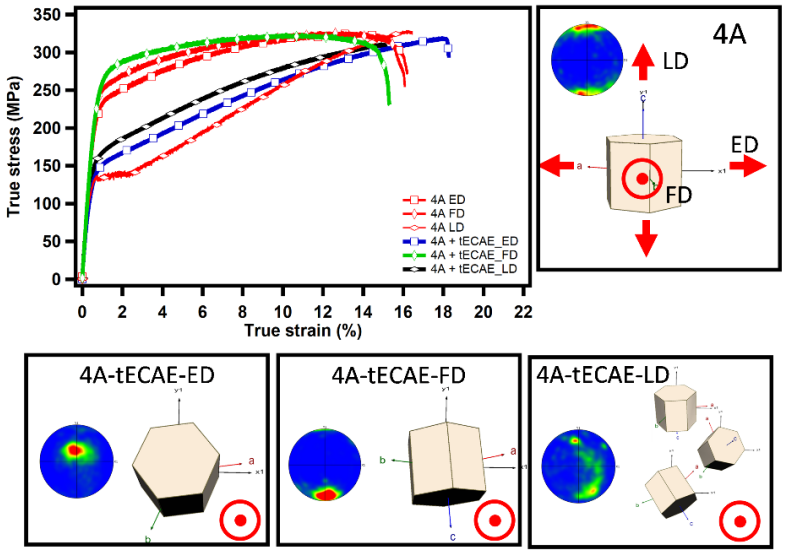

Figure 5.10 Tensile test response of 4A ECAE and 4A ECAE + tECAE processed samples along with the orientation of grains with respect to the tensile axis. Red arrows show the tensile test pull direction which is vertical and horizontal for 4A LD and 4A ED but it is out of the plane for 4A FD, and all the 4A + tECAE.

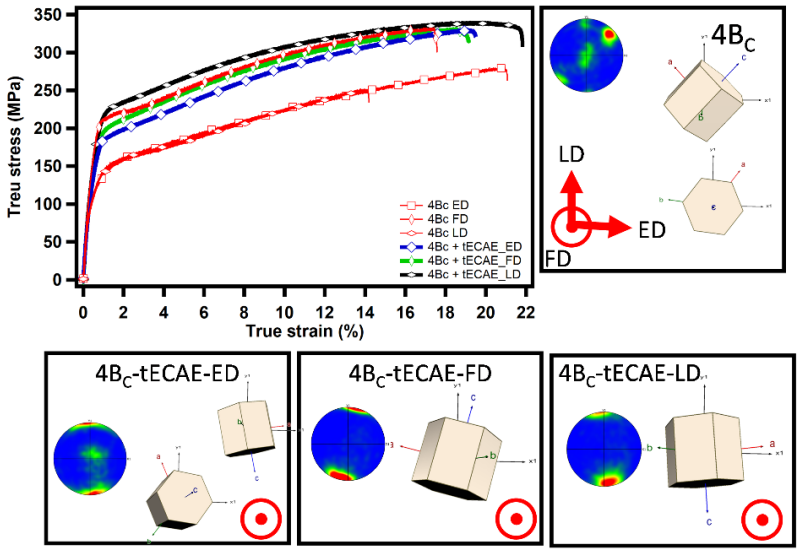

Figure 5.11 Tensile test response of $4B_C$ ECAE and $4B_C$ ECAE + tECAE processed samples along with the orientation of grains with respect to the tensile axis. The reference axis shows the tensile test pull direction which is vertical and horizontal for $4B_C$ LD and $4B_C$ ED sample, whereas it is out of plane for $4B_C$ FD, $4B_C$ -tECAE-ED, $4B_C$ -tECAE-FD, and $4B_C$ -tECAE-LD.

5.3 Discussion

5.3.1 Microstructure evolution

Route A and B_C were selected for ECAE processing AZ31 alloy because in each pass of these routes, the following pass has a very distinct shear plane orientation compared to the previous pass [11]. While no rotation occurs in between each route A pass, during route B_C, bars are rotated by 90° between passes. Thus, the shear plane rotations are different leading to variation in grain morphology, grain size, and texture evolution. Grain refinement starts to occur during ECAE processing even after one pass due to the application of plastic shear strain [19]. But to achieve uniformly refined grains, the material needs to be extruded through at least four passes, which results in accumulation of a large plastic shear strain of 4.6. Generally, four passes of ECAE are conducted due to following reasons: first, the routes involving a 90° rotation are realized along four spatially different planes after four passes. Second, a near saturation in grain refinement is reached after four passes due to reaching the limit of dislocation density. Further processing causes a very slight increased refinement which has also observed in previous studies [121, 122]. Therefore, the tECAE processing performed post ECAE did not cause much change in the grain size but it did influence the texture which is discussed later in the text. Overall, extensive grain refinement is achieved after four passes of ECAE processing, irrespective of the route while further tECAE processing led to texture changes but not necessarily contributed to further grain refinement.

The as-worked microstructures depict no twin formation (see Figure 5.2). Further detailed investigations of twins were performed through the band contrast maps in which

twins have been superimposed. A negligible amount of twin fraction is seen in the ECAE and ECAE + tECAE processed tubes. This is due to the processing being performed at 200 °C which is a high enough temperature to activate pyramidal $< c + a >$ II slip system to accommodate the c-axis deformation. Twinning gets suppressed when the pyramidal slip system is activated [25, 45].

5.3.2 Mechanical properties

The mechanical behavior of Mg alloys is be discussed next. In general, with grain refinement, the yield strength increases as per the Hall-Petch relation [56]. For Mg alloys, the interplay between grain size and grain orientation plays a significant role in their mechanical response. The difference in tensile flow behavior of AsRec material is already explained in previous chapters of this report. Now, let us first understand the tensile behavior of 4A material. The schematic of the hcp unit cell shown in Figure 5.10 and it represents the orientation of majority of the grains in 4A and subsequently tECAE processed material. The direction of tension pull is also shown for each tension test orientation. For Mg deformation, the activation of different slip and twin systems is based on Schmid's law [43]. The critical resolved shear stress (CRSS) values for each deformation mode are significantly different, hence, the mechanical response of the material depends on the angular relationship between crystallographic texture and the mechanical loading direction. In the present case of the 4A LD sample, the deformation will occur by activation of basal slip and extension twinning. In the initial part of deformation, extension twinning activates which reorient the grains by 86° along $< 1\bar{2}10 >$ orientation away from the tension direction [53, 117]. Such a reorientation

allows the hard non-basal prismatic slip system to accommodate the deformation, which results in strain hardening [25]. As the deformation proceeds, twin boundaries limit dislocation motion inside the twins, causing further strain hardening [104]. The obtained texture is also responsible for the tension behavior of 4A ED and 4A FD being similar to each other. The yield strength of both 4A ED and 4A FD are similar and higher than 4A LD. Since the tension pull in both these samples leads to c-axis contraction, such deformation can be accommodated largely by hard non-basal prismatic slip. Since the CRSS for activation of prismatic slip is high, this leads to a higher yield strength. Similar observations have been made in refs.[121, 123, 124]. The pyramidal and contraction twins are not considered here because their CRSS values are very high at room temperature [25, 117].

Second, the tensile flow response of 4A ECAE + 2 passes of tECAE processed materials is discussed. The texture evolution of 4A-tECAE-LD involves grains with various orientations, hence, various slip and twin systems are possibly active during tensile loading. The activation of multiple deformation modes in this case has improved the yield strength compared to the 4A LD case, but it is lower than the other two orientations after 4A processing. Similarly, for the 4A-tECAE-ED case, the strain hardening is not observed, and majority of the grains are oriented around 45° away from the tension axis, hence resulting in deformation by basal slip. The slip dominated deformation is the reason for the ductility being higher in the 4A-tECAE-ED case than other cases. The 4A-tECAE-FD material shows the highest yield strength as extension twins accommodate the deformation. Note, that the texture difference between 4A and

4A-tECAE-FD specimens is not much, which is the reason for their stress-strain flow response being similar.

Third, the tensile flow response of $4B_C$ along with the orientation of most of the grains are shown in Figure 5.11. In this case, most of the grains are oriented at an angle of around 45° away from both ED and LD. Hence, the yield strength of both $4B_C$ ED and $4B_C$ LD are similar. This happens because the grain orientation is favorable for deformation via basal slip. No strain hardening is observed in both these cases. However, $4B_C$ LD failed abruptly showing a lower ductility than $4B_C$ ED and $4B_C$ FD. This could be due to the presence of either coarse grains or grains having an orientation different from most of the grains leading to early crack initiation and fracture.

Lastly, the 4Bc + 2 pass tECAE sample's tensile behavior is discussed. Similar tensile flow curves are obtained for all three conditions, namely, $4B_C$-tECAE-ED, $4B_C$-tECAE-FD, and $4B_C$-tECAE-LD. This is because the majority of the grains are oriented in such a way that the tensile axis will contract the c-axis, resulting in activation of hard prismatic slip to accommodate the deformation, and a high yield strength is achieved.

The microhardness results reported in Table 5.2 show a drastic increase in hardness after ECAE processing. This increase occurs due to grain refinement following the Hall-Petch relation [56]. A saturation in hardness increase is achieved after ECAE processing and not much increase in hardness is obtained after further tECAE processing. This occurs due to limitations in further grain refinement as discussed previously. A homogenous hardness distribution is achieved after tECAE processing as shown in Chapter IV.

So, to sum this up, the ECAE processing does improve mechanical properties of Mg alloys and further development of a unique texture can be obtained in tubes via tECAE processing, which is not possible in conventional tube processing techniques resulting in inferior tube properties. Due to the hcp crystal structure of Mg alloys, anisotropy will exist in the material, but it can be reduced by reducing and reorienting the basal pole intensity, which could be achieved by selecting suitable processing routes.

5.4 Summary

A combination of ECAE and tECAE processing was successfully performed on AZ31 alloy tubes. The unique route of SPD processing imparted a high accumulated plastic strain of 6.7. The grain refinement obtained in AZ31 during tECAE process, after 4 passes of ECAE, was modest but a drastic variation in texture was obtained. A saturation in grain refinement occurs in SPD which has been observed in various earlier studies. From the results obtained it can be concluded that the ECAE process can be successfully scaled-up to sizes usable for manufacturing components in industries. The microstructure obtained after ECAE is independent of the workpiece size. Similarly, this principle can work for processing longer tubes using the tECAE method. Unique textures were developed in the subsequent tECAE processed samples which imparted improved strength and ductility to AZ31 alloy. Therefore, it can be concluded that with a suitable thermomechanical treatment, optimized microstructures can be produced in Mg alloys with enhanced mechanical properties via ECAE and tECAE.

CHAPTER VI

MICROSTRUCTURE, TEXTURE, AND MECHANICAL PROPERTIES OF SEVERE PLASTIC DEFORMATION PROCESSED AND RECRYSTALLIZED NIOBIUM TUBES

It is evident from the previous chapters that the ECAE based SPD processing techniques lead to grain refinement and improvement in mechanical properties in hcp material. In continuation of this, tECAE processing of a bcc metal, niobium, is investigated in this chapter. The tECAE method imparts uniform strain throughout the tube resulting in uniform grain refinement. The objectives of this study are:

1. To obtain fine-grained Nb tubes which may be used for hydroforming operations to produce SRF cavities.
2. To obtain axisymmetric properties in the tubes processed via tECAE. The experimental design enables application of axisymmetric strain to the tubes which causes homogenous deformation.
3. Investigate the recrystallization behavior and evolution of mechanical properties after tECAE and post-processing heat treatments.

6.1 Materials and Methods

A cast ingot of commercially pure niobium obtained from CBMM was used for this study. The nominal purity of material is 0.997 with the major substitutional impurity of Tantalum ~ 1500 ppm, and interstitial impurities of H (<10 ppm), C (<30 ppm), O (67-88 ppm), and N (<10 ppm). The material was pre-processed by multi-pass ECAE

processed to break down the initial large grain size and obtain a more uniform grain structure. Subsequently, 8mm thick wall tube with an outer diameter (OD) of 25 mm and 200 mm long was machined from the ECAE processed bar. Then the tube was forward extruded (FE) to obtain the desired OD of 38 mm and thickness of 3 mm. The details of the pre-processing conditions are described in ref. [125], a schematic is provided in Figure 6.1. This tube was sectioned into five 25 mm long tubes, followed by a heat treatment at 1000 °C for 3 hours in vacuum furnace (10^{-6} torr). The tubes were allowed to cool in the furnace. This ensures uniform and equiaxed microstructure. This is the starting condition of the material for tECAE processing and is referred to as FE-annealed throughout the text.

Several passes of tECAE processing was accomplished on the tubes at room temperature. Boron Nitride was used as the lubricant to reduce the friction between the workpiece and the tool. Out of the five tubes prepared, one tube did not undergo tECAE processing and was characterized to provide starting microstructure and mechanical properties. Rest of the four tubes underwent tECAE processing for 1, 2, 3, and 4 passes accumulating a strain of 1.05, 2.1, 3.15, and 4.2 respectively.

Specimens were sectioned from each as-worked tube via the wire-electro discharge machine (EDM) to perform post-processing heat treatments at various temperatures for 3 hours in a vacuum furnace (10^{-6} torr) to investigate the recrystallization behavior. The heat treatment temperatures selected were 300 °C, 500 °C, 700 °C, 800 °C, 900 °C, 1000 °C, 1100 °C. These temperatures were selected based

on the results obtained by in prior work [65, 125]. After the heating step, the samples were left to cool down in the furnace.

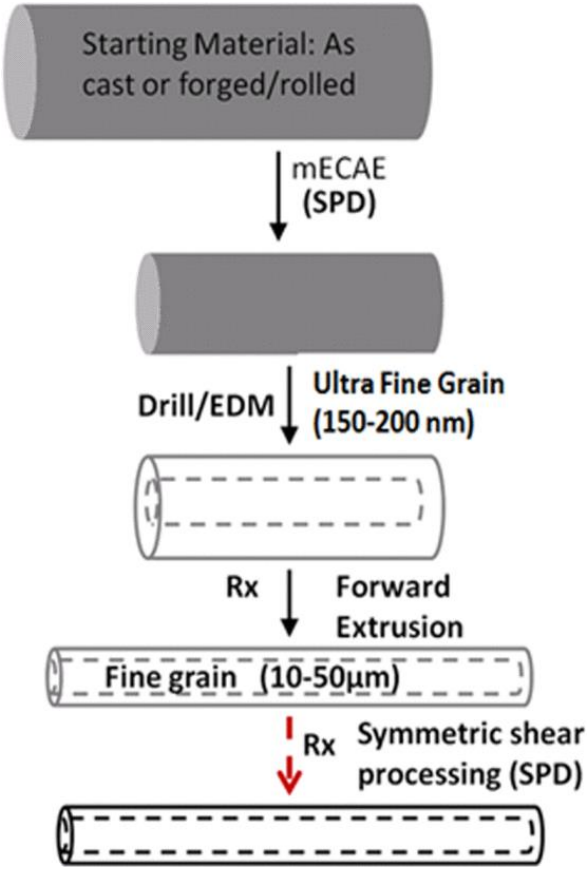

Figure 6.1 A schematic of the Nb processing prior to tECAE [125].

The samples for mechanical property measurements both in the as-worked and post-processing heat-treated conditions were also cut by wire-EDM. Flat dog-bone tensile specimens having dimensions of 2 x 3 x 8 mm^3 were obtained from two different orientations, one with tensile axis along the tECAE direction (tED) and the other with tensile axis along tangential or circumferential direction (TD) as shown in Figure 6.2. To

obtain the TD tensile specimens, the tubes were first cut in half along tED direction and then flattened using a hydraulic press. The dog-bone shaped specimens were cut from the flattened part (see Figure 6.2 (b)). Tension tests were performed on a servo-hydraulic MTS system with an initial strain rate of $5 \times 10^{-4}\ s^{-1}$ at room temperature using an MTS extensometer for recording strain. Several small specimens having dimensions 3 x 3 x 10 mm^3 were obtained for microstructural, microhardness and texture analysis. Specimens for mechanical testing and characterization were also obtained from the FE-annealed case for comparison between pre and post tECAE conditions.

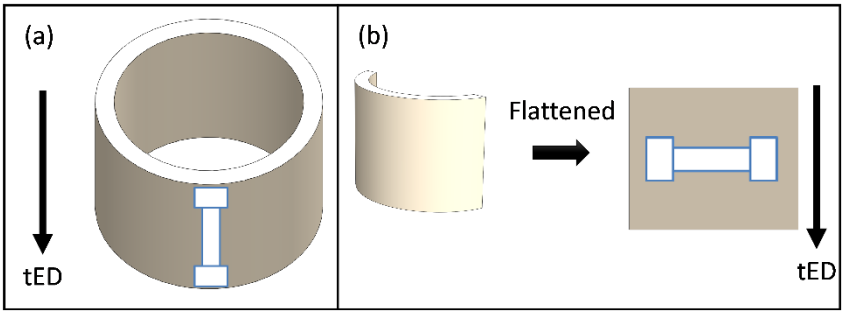

Figure 6.2 Sample orientation for tension tests from niobium tubes. (a) Tensile specimens with gage length along tECAE (tED) orientation. (b) Tensile specimens with gage length along circumference or tangential direction (TD).

For microstructure, the samples were mechanically polished to 1 μm, followed by vibratory polishing in colloidal silica for 24 hours. The etchant consisted of a 1:1:3 volume mixture of hydrofluoric acid: nitric acid: lactic acid to reveal the grain boundaries. A field emission Zeiss – ESB scanning electron microscope (SEM) was used to obtain the microstructure images of the FE-annealed and as-worked material. The

Vickers hardness measurements were taken at room temperature on the extrusion plane (plane perpendicular to tED) of all the samples using a Leco LM300AT Vickers hardness equipment by applying a load of 300 g for 13 seconds. For the Vickers hardness measurements, the samples' surface were polished to 1200 grit size SiC paper, and at least 10 measurements were taken for each condition. The crystallographic texture measurements were taken on the extrusion plane using a Bruker-AXS D8 X-ray diffractometer with Cu K_α (wavelength = 0.15406 nm) radiation. A Matlab MTEX toolbox [96] was used to plot the pole figures.

6.2 Results

6.2.1 Microstructure evolution

Figure 6.3 shows the SEM images of FE-annealed, and the as-worked materials from their respective extrusion planes. The microstructure for Nb tube processed via 3 passes of tECAE was not analyzed as it is one of the intermediate passes. The FE-annealed microstructure has equiaxed grains with an average grain size of 12.5 ± 7.6 μm, providing a strain free starting material for tECAE processing. The microstructure obtained after 1 pass of tECAE shows a collection of deformed coarse and fine grains. As the number of passes increase, more grain refinement is observed.

6.2.2 Hardness evolution with recrystallization

The FE-annealed condition (pre tECAE) microhardness is 67 ± 1.8 HV. The hardness increases to 123 ± 4.4 HV, 136 ± 1.9 HV, 137 ± 5.2 HV, and 141 ± 2.1 HV after 1, 2, 3, and 4 passes respectively. A significant increase in hardness after 1 pass of tECAE can be seen which is expected. Additionally, the degree of increase in hardness

with subsequent passes decreases. Such a saturation in hardness is generally observed in conventional ECAE processing [65].

To understand the recrystallization behavior of Nb processed with different strain levels (number of passes), a variation in microhardness is seen after different annealing temperatures as shown in Figure 6.4. The hardness values are tabulated in Table 6.1. It is important to note that a significant decrease in hardness occurs in the material after recrystallization. A material's hardness may decrease further with heat treatment due to subsequent grain growth. The 2 pass and 4 pass of tECAE processed samples show a slight increase in hardness from the as-worked condition (25 °C) to 300 °C annealing. This is followed by a gradual decrease in hardness to a constant level. For 3 passes of tECAE sample, the initial change in hardness is small but the standard deviation is high. The 1 pass sample showed a slight decrease in the hardness value compared to the as-worked condition (25 °C) to 300 °C annealing. Samples with different levels of strain reach the minimum hardness values at different annealing temperatures. While the 1 and 2 passes samples reach the minimum hardness at around 1000 °C annealing, the 3 and 4 passes samples reach the minimum hardness at around 900 °C.

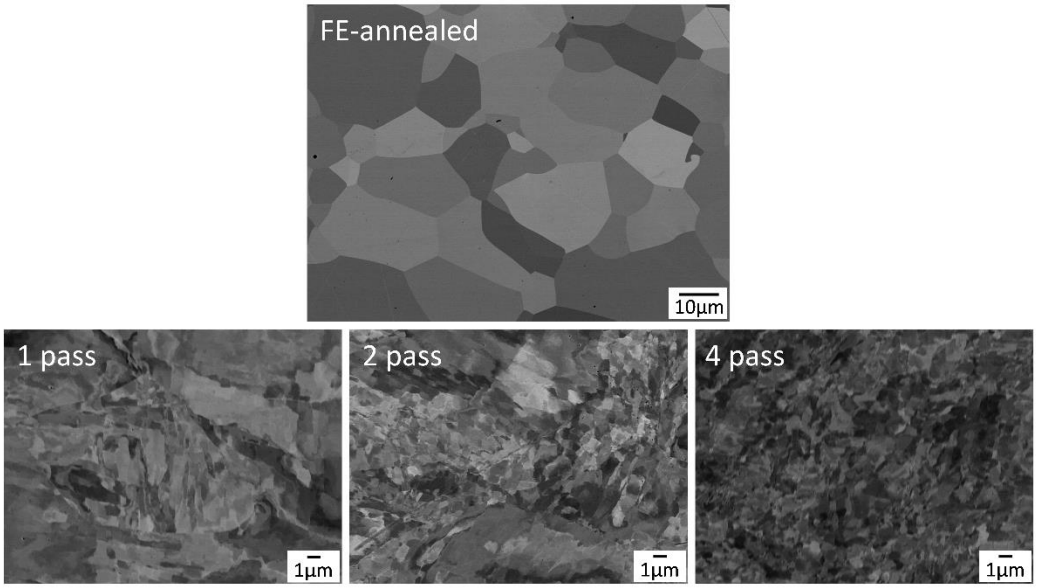

Figure 6.3 SEM images of niobium before and after tECAE processing. FE-annealed shows the forwarded extrusion annealed material's microstructure which is the starting condition for tECAE. The microstructures after 1,2, and 4 passes are shown.

Table 6.1 Microhardness evolution with different heat treatment temperatures in samples tECAE processed for various number of passes.

# tECAE passes	25°C	300°C	500°C	700°C	800°C	900°C	1000°C	1100°C
1P	123 ± 4.4	121 ± 3.7	121 ± 3.9	110 ± 2.9	111 ± 2.3	111 ± 2.4	75 ± 9.0	77 ± 1.8
2P	136 ± 1.9	141 ± 5.5	144 ± 6.3	134 ± 6.5	127 ± 2.4	97 ± 5.8	80 ± 3.1	77 ± 2.2
3P	137 ± 5.2	136 ± 8.0	132 ± 2.5	130 ± 3.0	111 ± 7.1	80 ± 4.3	80 ± 3.8	79 ± 1.5
4P	141 ± 2.1	148 ± 2.7	148 ± 4.0	136 ± 2.9	132 ± 3.0	81 ± 4.1	76 ± 3.5	76 ± 2.2

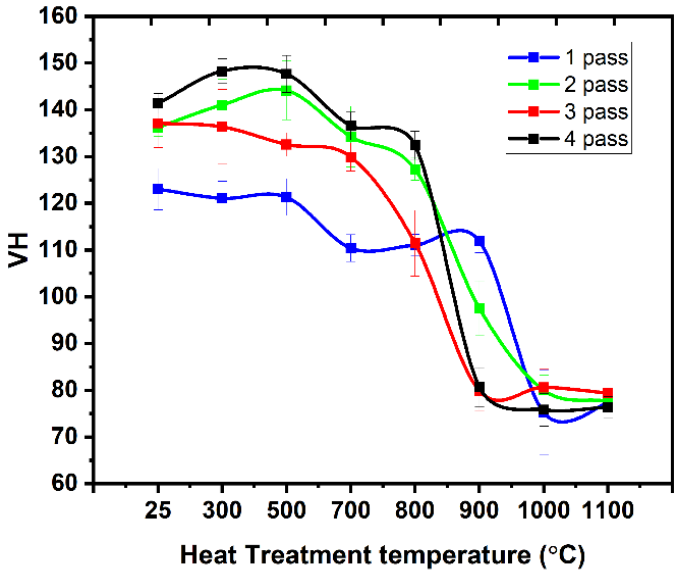

Figure 6.4 Recrystallization curves of 1, 2, 3, and 4 pass of tECAE processed Nb. The hardness measurements were taken on the extrusion plane.

6.2.3 Tension flow curves

The tension response for the FE-annealed and the as-worked materials are shown in Figure 6.5. Tension tests were also performed on the materials that underwent recrystallization heat treatment at 1000 °C after 2 and 4 passes of tECAE processing and the results are shown in Figure 6.5 (b) and (c) respectively. The tension specimens were prepared from both tED and TD direction to investigate the yield strength asymmetry after tECAE. The FE-annealed sample shows a significant difference in YS in the tED and TD orientations, while the difference in UTS and %elongation is not much. After 1 pass tECAE, significant improvement in YS is achieved. After 2 and 4 passes, the YS increases further, but the degree of increase is less, similar to the trend in hardness evolution. The increase in YS, leads to an expected decrease in elongation. Interestingly,

the difference in YS between the tED and the TD orientation reduces as the number of tECAE passes increase.

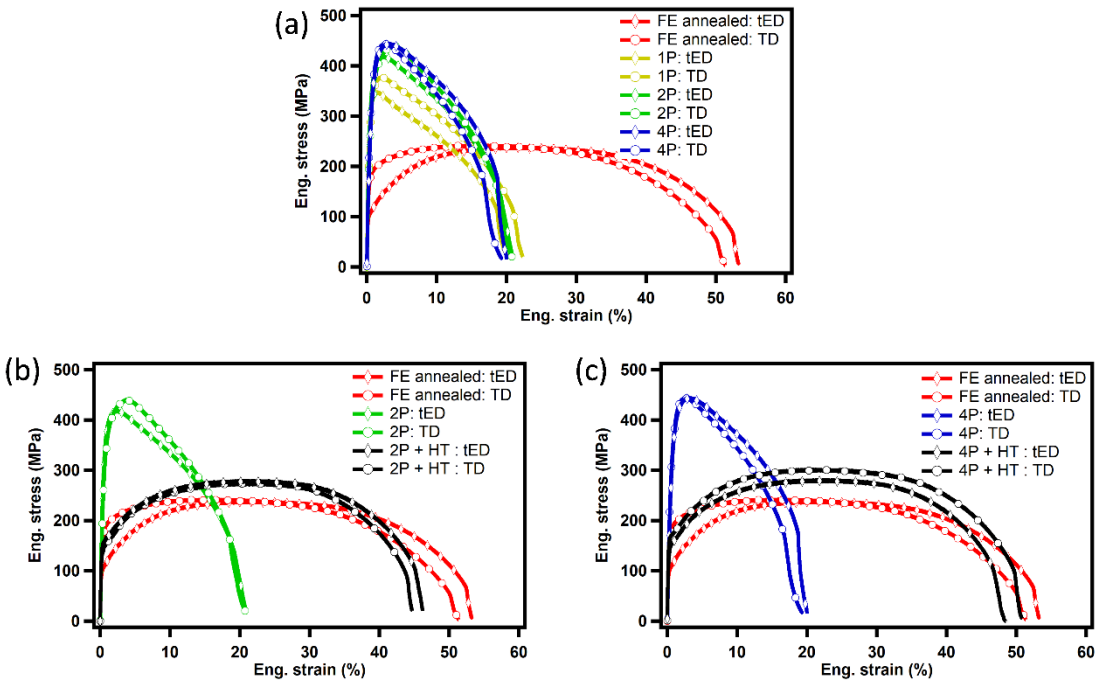

Figure 6.5 (a) Tensile engineering stress-strain curves of FE-annealed and 1, 2, and 4 passes tECAE processed Nb. (b) Tensile engineering stress-strain curves of FE-annealed, 2 pass tECAE processed, and 1000 °C heat treated (recrystallized) Nb samples. (c) Tensile engineering stress-strain curves of FE-annealed, 4 pass tECAE processed, and 1000 °C heat treated (recrystallized) Nb samples. (tED: tECAE direction, TD: Tangential direction, HT: Heat treated at 1000 °C)

Further analyses of the mechanical properties after recrystallization was performed on the 2 and 4 pass tECAE samples as those are of higher importance due to the tube sizes being the same as the pre-tECAE sample. After recrystallization, both 2 and 4 pass tECAE samples show a decrease in the YS while the elongation increases.

The UTS is higher than the FE-annealed material. Additionally, the YS is still similar in both the orientations.

6.2.4 Texture evolution

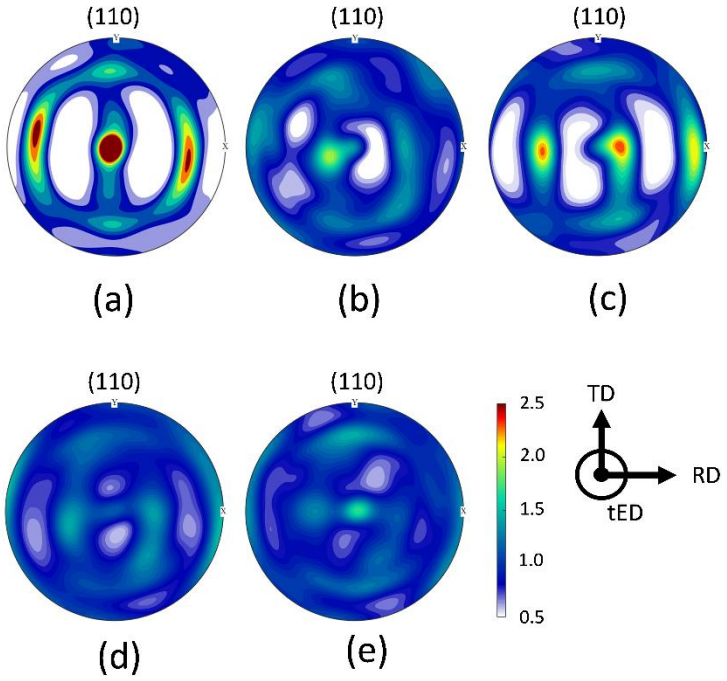

Figure 6.6 (110) pole figures of various passes of tECAE processed Nb. (a), (b), (c), (d), and (e) are pole figures of FE-annealed, 1 pass, 2 pass, 3 pass, and 4 pass Nb respectively. The tECAE direction is out of plane.

The texture evolution results are shown via (110) pole figures in Figure 6.6. The FE-annealed sample has strong (110) poles parallel to the tube extrusion direction. In the tECAE processed samples, weakening of (110) texture components can be observed as the number of passes increase. The texture components are also slightly rotated away from the tED orientation.

6.3 Discussion

6.3.1 Microstructural evolution

The pre-processed Nb was used in this study because the as-cast microstructure is extremely large grained and non-uniform. Secondary worked products such as sheet and tube often suffer from non-uniform and inconsistent grain size and texture because of cast texture persistence, leading to non-uniform mechanical properties. This could result in non-uniform deformation of sheet and tube during SRF cavity fabrication. Additionally, non-uniform microstructure causes a decrease in product yield and an increase in manufacturing costs. Therefore, to breakdown initial microstructure, the material was multi-pass ECAE processed followed by forward extrusion and then annealed to obtain a homogenous equiaxed microstructure.

The starting grain size for tECAE processing is relatively coarse which gets refined via the tECAE processing [57, 58, 125]. The tECAE process causes grain refinement by shear deformation [85] as seen in Figure 6.3. After 1 pass, the accumulated shear strain is relatively low in the material, hence the grain refinement achieved is not uniform and several coarse grains still exist in the microstructure. The fine grains are arranged between the large grains. As the number of passes increased, further reduction in grain size was observed due to accumulation of large shear strain upto 4.2. Previous work on conventional ECAE processing has also proven to be effective in grain refinement [58, 65].

6.3.2 Microhardness and recrystallization behavior

The microhardness increases with the number of passes because of the accumulated strain which leads to higher dislocation density and forms tangled substructures. The hardnesses increase levels off after two passes and further passes result in only a small increase as seen in Table 6.1 and Figure 6.4. Such variation in hardness is explained by Hartwig et. al. [65] for the conventional ECAE processing which applies well for the tECAE processing. According to ref. [65], during the first pass, the grains have different orientations, hence, the grains will show a difference in the deformation tendency when strain is applied. Some grains will be oriented along the shear deformation direction and accommodate the deformation easily whereas, some grains whose slip system is not favorably oriented with the shear deformation direction will not deform readily or may rotate, resulting in non-uniform deformation, which in turn results in non-uniform grain size. Thus, the variation in hardness is large after 1 pass of tECAE as can be seen from the large standard deviation values. As the number of passes increase, more grains are favorably oriented resulting in more uniform deformation, and higher accumulated dislocation density and high microhardness.

The effect of different annealing temperatures on hardness evolution are shown in Figure 6.4. Heat treatment of Nb tubes is performed because the residual dislocations may reduce the SRF cavity performance [57]. The initial increase in hardness could be due to recovery or formation of a Cottrell atmosphere restraining the dislocation motion [38, 65]. For the tubes processed with different strain levels, the minimum hardness is reached at different annealing temperatures. This happens because as the accumulated

strain increases in the material with increasing the number of passes of tECAE, more stored energy is accumulated in the dislocations, which results in lower temperature of recrystallization. Similar results of recrystallization have been obtained in other studies based on copper [126] and niobium [65]. Note that the hardness and recrystallization temperature for the commercially pure reactor grade Nb (99.7% pure) used in this study are higher than RRR grade Nb (>99.99% pure). While for the reactor grade Nb, complete recrystallization occurs around 1000 °C, it occurs at around 800 °C for the RRR grade Nb [57, 66]. This happens due to the presence of more impurities in reactor grade Nb which restrains dislocation motion. The recrystallization temperature is also influenced by the amount of dislocations, strain path, and heating rate. The difference in the purity level also influences texture evolution.

6.3.3 Tensile flow behavior

The tECAE processed samples have higher strength than the FE-annealed material due to grain refinement. It is well known as per the Hall-Petch relation [56] that as the grain size decreases, the strength of a material increases whereas the ductility decreases. The FE-annealed material shows a difference in yield strength in the extrusion direction and tangential directions. This is due to the strong texture in the tube. After tECAE processing, a weakened texture is formed, leading to reduction in the anisotropic mechanical properties which is evident from the tensile flow response. After recrystallization heat treatment at 1000 °C, the yield strength and tensile strength decrease whereas ductility is restored close to the pre-tECAE condition. The recrystallized material still has higher UTS than the pre-tECAE condition and the yield

strength is similar in both orientations. The higher mechanical UTS is a result of a smaller grain size even after recrystallization as observed in previous studies as well [58, 65, 125, 127]. Therefore, it can be concluded that tECAE results in fine grain structure and increased isotropic behavior of Nb tubes even after recrystallization.

6.3.4 Texture evolution

The texture obtained in the FE-annealed material (Figure 6.6) is similar to the dominant textures in extruded and drawn bcc material in which {110} is parallel to the major axes [128]. Variation in texture can be seen after tECAE processing with the {110} poles being inclined away from tED and weakened in intensity. The texture obtained after tECAE is different than that observed after rolling. It is plausible to assume that such texture change made the Nb tubes more isotropic.

6.4 Summary

The tECAE processing approach was successfully applied to commercially pure niobium tubes without causing any fracture in the material. The tubes were processed up to four passes of tECAE at room temperature. Post-processing heat treatment was performed on the as-worked material to investigate the variation in hardnesses and the role of accumulated plastic strain on recrystallization temperature. Tensile test results of both the as-worked and heat-treated samples show drastic improvement in tension properties with reducing the asymmetry between yield strengths from two orientations separated by 90°. Weakening of texture was also observed after tECAE processing. Therefore, it can be concluded that the new thermomechanical processing of tECAE is a promising technique to improve the properties of Nb, which could subsequently be used

for hydroforming SRF cavities. Further investigations on the effect of more passes of tECAE on the mechanical properties, microstructural evolution, and EBSD texture measurements remains to be performed.

CHAPTER VII

SUMMARY OF RESULTS, CONCLUSIONS AND SUGGESTIONS FOR FUTURE WORK

7.1 Results and conclusions

1. The new severe plastic deformation technique called tube equal channel angular extrusion (tECAE) successfully processed AZ31 magnesium alloy tubes at various low temperatures (120 °C, 175 °C, 200 °C).
2. The starting crystallographic textures and grain size significantly influence the evolution of texture, grain morphology, and mechanical responses of the processed AZ31 tubes due to the activation of different slip systems.
3. While the AZ31 material with basal poles along tECAE direction did not achieve large variation in texture after tECAE processing, all the other starting orientations lead to major changes to the texture. The significant effect of texture was observed in the mechanical flow response of the material.
4. The hybrid ECAE and tECAE processing was successfully conducted with unique starting textures for tECAE, which enabled a better understanding of the influence of starting texture on grain refinement and texture evolution as a function of strain.
5. ECAE can be scaled-up to process large Mg alloy bars. It is concluded that the grain refinement, texture modification and improvement in strength is independent of the size of the workpiece in ECAE.

6. Viscoplastic self-consistent (VPSC) crystal plasticity modeling accurately predicts the texture after tECAE processing of AZ31 alloy. The active deformation modes during processing were modeled successfully. The understanding of different deformation mode activities obtained from VPSC could help in developing the best processing route for Mg alloys that result in the highest strength and ductility.
7. Pure niobium tubes were successfully processed up to four passes of tECAE at room temperature resulting in a significant increase in the strength of the material due to grain refinement.
8. Post-processing heat treatment of niobium processed to different tECAE strain levels show a variation in recrystallization temperature as a function of accumulated plastic strain.
9. The tECAE processing resulted in similar mechanical properties in two orientations separated by 90°. It is concluded that tECAE can be an effective thermomechanical technique to fabricate Nb tubes with consistent, reproducible material properties that show potential for improved hydroformability.

7.2 Future work

Based on the findings of this research, several recommendations are offered for future studies.

1. Given the success of the tECAE technique in processing tubular forms of materials, new tools must be designed to process longer tubes for applications such as in transportation vehicles. Also, designing a tool to process thin tubes

with small diameter for implant stents will be beneficial for the biomedical industry.

2. A greater number of tECAE passes should be performed on new Mg alloys at lower temperatures (<120 °C) which could possibly lead to further grain refinement, enabling one to achieve better mechanical properties and reduce anisotropy.
3. The tECAE processing approach applies axisymmetric shear strain to tubes. Therefore, more mechanical tests should be performed from different orientations. Since Mg alloys are generally brittle, flattening the tubes to obtain the tensile test samples from circumferential (tangential) direction will be challenging. Techniques such as ring hoop tensile testing must be investigated.
4. The effect of tECAE processing on precipitation kinetics, and the corrosion response of Mg alloy tubes should be explored.
5. Hydroforming experiments should be performed on the tECAE processed tubes, to evaluate hydroformability relative to that of conventionally fabricated tubes.
6. The tECAE processing of long Nb tubes will provide the opportunity to produce multi-cell SRF cavity via hydroforming, eliminating the need of welding which should significantly improve the cavity performance. Thus experiments should be carried out that explore the tube geometry (diameter, length, wall thickness) and material limits of tECAE.

REFERENCES

[1] M. Liewald, R. Pop, Magnesium tube hydroforming, Materialwissenschaft und Werkstofftechnik: Entwicklung, Fertigung, Prüfung, Eigenschaften und Anwendungen technischer Werkstoffe 39(4-5) (2008) 343-348.

[2] R. Sikand, A.M. Kumar, A.K. Sachdev, A.A. Luo, V. Jain, A.K. Gupta, AM30 porthole die extrusions—A comparison with circular seamless extruded tubes, Journal of Materials Processing Technology 209(18) (2009) 6010-6020.

[3] E. Aydogan, S.A. Maloy, O. Anderoglu, C. Sun, J.G. Gigax, L. Shao, F.A. Garner, I.E. Anderson, J.J. Lewandowski, Effect of tube processing methods on microstructure, mechanical properties and irradiation response of 14YWT nanostructured ferritic alloys, Acta Materialia 134 (2017) 116-127.

[4] V. Palmieri, R. Preciso, V.L. Ruzinov, S.Y. Stark, S. Gambalonga, Forming of seamless high beta accelerating cavities by the spinning technique, Nuclear Instruments and Methods in Physics Research Section A: Accelerators, Spectrometers, Detectors and Associated Equipment 342(2) (1994) 353-356.

[5] C. Zhang, G. Zhao, Z. Chen, H. Chen, F. Kou, Effect of extrusion stem speed on extrusion process for a hollow aluminum profile, Materials Science and Engineering: B 177(19) (2012) 1691-1697.

[6] R. Waksman, R. Pakala, P.K. Kuchulakanti, R. Baffour, D. Hellinga, R. Seabron, F.O. Tio, E. Wittchow, S. Hartwig, C. Harder, R. Rohde, B. Heublein, A. Andreae, K.H. Waldmann, A. Haverich, Safety and efficacy of bioabsorbable magnesium alloy stents in porcine coronary arteries, Catheter Cardiovasc Interv 68(4) (2006) 607-17; discussion 618-9.

[7] R. Erbel, C. Di Mario, J. Bartunek, J. Bonnier, B. de Bruyne, F.R. Eberli, P. Erne, M. Haude, B. Heublein, M. Horrigan, C. Ilsley, D. Böse, J. Koolen, T.F. Lüscher, N. Weissman, R. Waksman, Temporary scaffolding of coronary arteries with bioabsorbable magnesium stents: a prospective, non-randomised multicentre trial, The Lancet 369(9576) (2007) 1869-1875.

[8] R.K. Roy, S.K. Das, A. Srivastava, A.K. Panda, A. Mitra, Damage evaluation of fossil fuelled power plant boiler tubes through magnetic Barkhausen technique, Eng. Failure Anal. 44 (2014) 195-201.

[9] W. Singer, X. Singer, I. Jelezov, P. Kneisel, Hydroforming of elliptical cavities, Physical Review Special Topics - Accelerators and Beams 18(2) (2015) 022001.

[10] V. Segal, Materials processing by simple shear, Materials Science and Engineering: A 197(2) (1995) 157-164.

[11] R.Z. Valiev, T.G. Langdon, Principles of equal-channel angular pressing as a processing tool for grain refinement, Prog. Mater. Sci. 51(7) (2006) 881-981.

[12] V.M. Segal, Engineering and commercialization of equal channel angular extrusion (ECAE), Materials Science and Engineering: A 386(1-2) (2004) 269-276.

[13] A.V. Nagasekhar, U. Chakkingal, P. Venugopal, Equal Channel Angular Extrusion of Tubular Aluminum Alloy Specimens—Analysis of Extrusion Pressures and Mechanical Properties, Journal of Manufacturing Processes 8(2) (2006) 112-120.

[14] A.V. Nagasekhar, U. Chakkingal, P. Venugopal, Candidature of equal channel angular pressing for processing of tubular commercial purity-titanium, Journal of Materials Processing Technology 173(1) (2006) 53-60.

[15] J. Valder, M. Rijesh, A.O. Surendranathan, Forming of Tubular Commercial Purity Aluminum by ECAP, Mater Manuf Process 27(9) (2012) 986-989.

[16] F. Djavanroodi, A.A. Zolfaghari, M. Ebrahimi, K.M. Nikbin, Equal channel angular pressing of tubular samples, Acta Metallurgica Sinica (English Letters) 26(5) (2013) 574-580.

[17] K.T. Hartwig, R.E. Barber, Processing of hollow sections, U.S. Patent No. 9,776,232, Washington, DC: U.S. Patent and Trademark Office., 2017.

[18] J.X. Xie, T. Murakami, K. Ikeda, H. Takahashi, Experimental simulation of metal flow in porthole-die extrusion, Journal of Materials Processing Technology 49(1) (1995) 1-11.

[19] M. Al-Maharbi, I. Karaman, I.J. Beyerlein, D. Foley, K.T. Hartwig, L.J. Kecskes, S.N. Mathaudhu, Microstructure, crystallographic texture, and plastic anisotropy

evolution in an Mg alloy during equal channel angular extrusion processing, Materials Science and Engineering: A 528(25-26) (2011) 7616-7627.

[20] D.C. Foley, M. Al-Maharbi, K.T. Hartwig, I. Karaman, L.J. Kecskes, S.N. Mathaudhu, Grain refinement vs. crystallographic texture: Mechanical anisotropy in a magnesium alloy, Scripta Materialia 64(2) (2011) 193-196.

[21] E. Dogan, M. Vaughan, S. Wang, I. Karaman, G. Proust, Role of starting texture and deformation modes on low-temperature shear formability and shear localization of Mg–3Al–1Zn alloy, Acta Materialia 89 (2015) 408-422.

[22] E. Dogan, S. Wang, M.W. Vaughan, I. Karaman, Dynamic precipitation in Mg-3Al-1Zn alloy during different plastic deformation modes, Acta Materialia 116 (2016) 1-13.

[23] T.T.T. Trang, J.H. Zhang, J.H. Kim, A. Zargaran, J.H. Hwang, B.C. Suh, N.J. Kim, Designing a magnesium alloy with high strength and high formability, Nat. Commun. 9 (2018) 6.

[24] A. Vinogradov, V.N. Serebryany, S.V. Dobatkin, Tailoring microstructure and properties of fine grained magnesium alloys by severe plastic deformation, Advanced Engineering Materials 20(4) (2018) 1700785.

[25] M.W. Vaughan, W. Nasim, E. Dogan, J.S. Herrington, G. Proust, A.A. Benzerga, I. Karaman, Interplay between the effects of deformation mechanisms and dynamic recrystallization on the failure of Mg-3Al-1Zn, Acta Materialia 168 (2019) 448-472.

[26] A. Fata, G. Faraji, M.M. Mashhadi, V. Tavakkoli, Hot tensile deformation and fracture behavior of ultrafine-grained AZ31 magnesium alloy processed by severe plastic deformation, Mater. Sci. Eng. A-Struct. Mater. Prop. Microstruct. Process. 674 (2016) 9-17.

[27] S. Sepahi-Boroujeni, A. Sepahi-Boroujeni, Improvements in microstructure and mechanical properties of AZ80 magnesium alloy by means of an efficient, novel severe plastic deformation process, Journal of Manufacturing Processes 24 (2016) 71-77.

[28] A. Fata, M. Eftekhari, G. Faraji, M.M. Mashhadi, Enhanced Hot Tensile Ductility of Mg-3Al-1Zn Alloy Thin-Walled Tubes Processed Via a Combined Severe Plastic

Deformation, Journal of Materials Engineering and Performance 27(5) (2018) 2330-2337.

[29] T.M. Pollock, Weight Loss with Magnesium Alloys, Science 328(5981) (2010) 986-987.

[30] F. Witte, The history of biodegradable magnesium implants: A review, Acta Biomater. 6(5) (2010) 1680-1692.

[31] J.-F. Nie, Precipitation and Hardening in Magnesium Alloys, Metallurgical and Materials Transactions A 43(11) (2012) 3891-3939.

[32] A.A. Luo, Magnesium casting technology for structural applications, Journal of Magnesium and Alloys 1(1) (2013) 2-22.

[33] C. Bettles, M. Gibson, Current wrought magnesium alloys: Strengths and weaknesses, JOM 57(5) (2005) 46-49.

[34] M.K. Kulekci, Magnesium and its alloys applications in automotive industry, The International Journal of Advanced Manufacturing Technology 39(9-10) (2008) 851-865.

[35] H. Hermawan, D. Dubé, D. Mantovani, Developments in metallic biodegradable stents, Acta Biomater. 6(5) (2010) 1693-1697.

[36] M.P. Staiger, A.M. Pietak, J. Huadmai, G. Dias, Magnesium and its alloys as orthopedic biomaterials: a review, Biomaterials 27(9) (2006) 1728-1734.

[37] X. Gu, Y. Zheng, Y. Cheng, S. Zhong, T. Xi, In vitro corrosion and biocompatibility of binary magnesium alloys, Biomaterials 30(4) (2009) 484-98.

[38] G.E. Dieter, D.J. Bacon, Mechanical metallurgy, McGraw-hill New York1986.

[39] K. Hantzsche, J. Bohlen, J. Wendt, K. Kainer, S. Yi, D. Letzig, Effect of rare earth additions on microstructure and texture development of magnesium alloy sheets, Scripta Materialia 63(7) (2010) 725-730.

[40] W. Liu, F. Cao, L. Chang, Z. Zhang, J. Zhang, Effect of rare earth element Ce and La on corrosion behavior of AM60 magnesium alloy, Corros. Sci. 51(6) (2009) 1334-1343.

[41] J. Bohlen, M.R. Nürnberg, J.W. Senn, D. Letzig, S.R. Agnew, The texture and anisotropy of magnesium–zinc–rare earth alloy sheets, Acta Materialia 55(6) (2007) 2101-2112.

[42] H. Fan, J.A. El-Awady, Molecular dynamics simulations of orientation effects during tension, compression, and bending deformations of magnesium nanocrystals, Journal of Applied Mechanics 82(10) (2015).

[43] E. Schmid, W. Boas, Plasticity of crystals, (1950).

[44] A. Chapuis, J.H. Driver, Temperature dependency of slip and twinning in plane strain compressed magnesium single crystals, Acta Materialia 59(5) (2011) 1986-1994.

[45] S.R. Agnew, Ö. Duygulu, Plastic anisotropy and the role of non-basal slip in magnesium alloy AZ31B, Int. J. Plast. 21(6) (2005) 1161-1193.

[46] J. Koike, T. Kobayashi, T. Mukai, H. Watanabe, M. Suzuki, K. Maruyama, K. Higashi, The activity of non-basal slip systems and dynamic recovery at room temperature in fine-grained AZ31B magnesium alloys, Acta Materialia 51(7) (2003) 2055-2065.

[47] R.v. Mises, Mechanik der plastischen Formänderung von Kristallen, ZAMM-Journal of Applied Mathematics and Mechanics/Zeitschrift für Angewandte Mathematik und Mechanik 8(3) (1928) 161-185.

[48] G.I. Taylor, Plastic strain in metals, J. Inst. Metals 62 (1938) 307-324.

[49] M.H. Yoo, Slip, twinning, and fracture in hexagonal close-packed metals, Metallurgical Transactions A 12(3) (1981) 409-418.

[50] A. Jain, S.R. Agnew, Modeling the temperature dependent effect of twinning on the behavior of magnesium alloy AZ31B sheet, Materials Science and Engineering: A 462(1) (2007) 29-36.

[51] O. Muránsky, D.G. Carr, M.R. Barnett, E.C. Oliver, P. Šittner, Investigation of deformation mechanisms involved in the plasticity of AZ31 Mg alloy: In situ neutron diffraction and EPSC modelling, Materials Science and Engineering: A 496(1) (2008) 14-24.

[52] F. Hauser, P. Landon, J. Dorn, DEFORMATION AND FRACTURE OF ALPHA SOLID SOLUTIONS OF LITHIUM IN MAGNESIUM. Technical Report No. 4, California. Univ., Berkeley. Minerals Research Lab., 1956.

[53] M.R. Barnett, Twinning and the ductility of magnesium alloys: Part I: "Tension" twins, Materials Science and Engineering: A 464(1) (2007) 1-7.

[54] M.R. Barnett, Twinning and the ductility of magnesium alloys: Part II. "Contraction" twins, Materials Science and Engineering: A 464(1) (2007) 8-16.

[55] S.E. Ion, F.J. Humphreys, S.H. White, Dynamic recrystallisation and the development of microstructure during the high temperature deformation of magnesium, Acta Metall. 30(10) (1982) 1909-1919.

[56] N. Hansen, Hall–Petch relation and boundary strengthening, Scripta Materialia 51(8) (2004) 801-806.

[57] T.R. Bieler, N.T. Wright, F. Pourboghrat, C. Compton, K.T. Hartwig, D. Baars, A. Zamiri, S. Chandrasekaran, P. Darbandi, H. Jiang, E. Skoug, S. Balachandran, G.E. Ice, W. Liu, Physical and mechanical metallurgy of high purity Nb for accelerator cavities, Physical Review Special Topics - Accelerators and Beams (2010) Medium: X; Size: 031002-1-031002-13.

[58] K.T. Hartwig, J. Wang, D.C. Baars, T.R. Bieler, S.N. Mathaudhu, R.E. Barber, Microstructural Refinement of Niobium for Superconducting RF Cavities, IEEE Transactions on Applied Superconductivity 17(2) (2007) 1305-1309.

[59] W. Singer, Seamless/bonded niobium cavities, Physica C: Superconductivity 441(1) (2006) 89-94.

[60] H. Padamsee, The science and technology of superconducting cavities for accelerators, Supercon. Sci. Technol. 14(4) (2001) R28-R51.

[61] V. Palmieri, Advancements on spinning of seamless multicell reentrant cavities, Proc. 11th Int. Workshop on RF Superconductivity, 2003, pp. 357-361.

[62] K. Saito, T. Fujino, H. Inoue, N. Hitomi, E. Kako, T. Shishido, S. Noguchi, M. Ono, Y. Yamazaki, V. Palmieri, Feasibility study of Nb/Cu clad superconducting RF cavities, IEEE Transactions on Applied Superconductivity 9(2) (1999) 877-880.

[63] D. Finnemore, T. Stromberg, C. Swenson, Superconducting properties of high-purity niobium, Phys. Rev. 149(1) (1966) 231.

[64] G. Simmons, Single crystal elastic constants and calculated aggregate properties, Southern Methodist Univ Dallas Tex, 1965.

[65] K. Hartwig, D. Bryant, S. Mathaudhu, R. Barber, J. Im, Grain refinement of Niobium by severe plastic deformation, AIP Conf. Proc., American Institute of Physics, 2004, pp. 441-449.

[66] S. Balachandran, A. Polyanskii, S. Chetri, P. Dhakal, Y.-F. Su, Z.-H. Sung, P.J. Lee, Direct evidence of microstructure dependence of magnetic flux trapping in niobium, Scientific Reports 11(1) (2021) 5364.

[67] Y. Huang, T.G. Langdon, Advances in ultrafine-grained materials, Materials Today 16(3) (2013) 85-93.

[68] V. Segal, K. Hartwig, R. Goforth, In situ composites processed by simple shear, Materials Science and Engineering: A 224(1-2) (1997) 107-115.

[69] A.P. Zhilyaev, T.G. Langdon, Using high-pressure torsion for metal processing: Fundamentals and applications, Prog. Mater. Sci. 53(6) (2008) 893-979.

[70] Y. Saito, H. Utsunomiya, N. Tsuji, T. Sakai, Novel ultra-high straining process for bulk materials—development of the accumulative roll-bonding (ARB) process, Acta materialia 47(2) (1999) 579-583.

[71] M. Richert, Q. Liu, N. Hansen, Microstructural evolution over a large strain range in aluminium deformed by cyclic-extrusion–compression, Materials Science and Engineering: A 260(1-2) (1999) 275-283.

[72] D.M. Jafarlou, E. Zalnezhad, M.A. Hassan, M.A. Ezazi, N.A. Mardi, A.M.S. Hamouda, M. Hamdi, G.H. Yoon, Severe plastic deformation of tubular AA 6061 via equal channel angular pressing, Materials & Design 90 (2016) 1124-1135.

[73] L. Tóth, M. Arzaghi, J. Fundenberger, B. Beausir, O. Bouaziz, R. Arruffat-Massion, Severe plastic deformation of metals by high-pressure tube twisting, Scripta Materialia 60(3) (2009) 175-177.

[74] J.T. Wang, Z. Li, J. Wang, T.G. Langdon, Principles of severe plastic deformation using tube high-pressure shearing, Scripta Materialia 67(10) (2012) 810-813.

[75] G. Faraji, M.M. Mashhadi, H.S. Kim, Tubular channel angular pressing (TCAP) as a novel severe plastic deformation method for cylindrical tubes, Materials Letters 65(19-20) (2011) 3009-3012.

[76] G. Faraji, A. Babaei, M.M. Mashhadi, K. Abrinia, Parallel tubular channel angular pressing (PTCAP) as a new severe plastic deformation method for cylindrical tubes, Materials Letters 77 (2012) 82-85.

[77] H.S. Kim, Evaluation of strain rate during equal-channel angular pressing, J. Mater. Res. 17(1) (2002) 172-179.

[78] C. Gu, L.S. Toth, D. Field, J.-J. Fundenberger, Y.D. Zhang, Room temperature equal-channel angular pressing of a magnesium alloy, Acta Materialia 61(8) (2013) 3027-3036.

[79] H. Zhang, Y. Yan, J. Fan, W. Cheng, H.J. Roven, B. Xu, H. Dong, Improved mechanical properties of AZ31 magnesium alloy plates by pre-rolling followed by warm compression, Materials Science and Engineering: A 618 (2014) 540-545.

[80] L. Chang, Y. Wang, X. Zhao, J. Huang, Microstructure and mechanical properties in an AZ31 magnesium alloy sheet fabricated by asymmetric hot extrusion, Materials Science and Engineering: A 496(1) (2008) 512-516.

[81] O. Saray, G. Purcek, I. Karaman, Principles of equal-channel angular sheet extrusion (ECASE): application to IF-steel sheets, Rev. Adv. Mater. Sci 25 (2010) 42-51.

[82] J.C. Springs, A. Srivastava, Z.S. Levin, R.E. Barber, K.T. Hartwig, Microstructure and Mechanical Properties of Heavily Worked and Recrystallized Copper for Low-Temperature Superconductor Applications, IEEE Transactions on Applied Superconductivity 27(4) (2017) 1-5.

[83] S. Agnew, J. Horton, T. Lillo, D. Brown, Enhanced ductility in strongly textured magnesium produced by equal channel angular processing, Scripta Materialia 50(3) (2004) 377-381.

[84] Y. Iwahashi, J. Wang, Z. Horita, M. Nemoto, T.G. Langdon, Principle of equal-channel angular pressing for the processing of ultra-fine grained materials, Scripta Materialia 35(2) (1996) 143-146.

[85] A. Srivastava, M.W. Vaughan, B. Mansoor, W. Nasim, R.E. Barber, I. Karaman, K.T. Hartwig, Tube equal channel angular extrusion (tECAE) of Mg–3Al–1Zn alloy, Materials Science and Engineering: A 814 (2021) 141236.

[86] K. Nakashima, Z. Horita, M. Nemoto, T.G. Langdon, Development of a multi-pass facility for equal-channel angular pressing to high total strains, Materials Science and Engineering: A 281(1-2) (2000) 82-87.

[87] R.A. Lebensohn, C.N. Tomé, A self-consistent anisotropic approach for the simulation of plastic deformation and texture development of polycrystals: Application to zirconium alloys, Acta Metallurgica et Materialia 41(9) (1993) 2611-2624.

[88] C.N. Tomé, R.A. Lebensohn, U.F. Kocks, A model for texture development dominated by deformation twinning: Application to zirconium alloys, Acta Metallurgica et Materialia 39(11) (1991) 2667-2680.

[89] R.A. Lebensohn, C.N. Tomé, A self-consistent viscoplastic model: prediction of rolling textures of anisotropic polycrystals, Materials Science and Engineering: A 175(1) (1994) 71-82.

[90] P. Van Houtte, L. Rabet, Generalization of the relaxed constraints models for the prediction of deformation textures, Rev. Met. Paris 94(12) (1997) 1483-1494.

[91] R. Hill, A self-consistent mechanics of composite materials, J. Mech. Phys. Solids 13(4) (1965) 213-222.

[92] R.J. Asaro, A. Needleman, Overview no. 42 Texture development and strain hardening in rate dependent polycrystals, Acta Metall. 33(6) (1985) 923-953.

[93] C.N. Tomé, P.J. Maudlin, R.A. Lebensohn, G.C. Kaschner, Mechanical response of zirconium—I. Derivation of a polycrystal constitutive law and finite element analysis, Acta Materialia 49(15) (2001) 3085-3096.

[94] S.M. Razavi, D.C. Foley, I. Karaman, K.T. Hartwig, O. Duygulu, L.J. Kecskes, S.N. Mathaudhu, V.H. Hammond, Effect of grain size on prismatic slip in Mg-3Al-1Zn alloy, Scripta Materialia 67(5) (2012) 439-442.

[95] J.M. Sosa, D.E. Huber, B. Welk, H.L. Fraser, Development and application of MIPAR™: a novel software package for two- and three-dimensional microstructural characterization, Integrating Materials and Manufacturing Innovation 3(1) (2014) 123-140.

[96] F. Bachmann, R. Hielscher, H. Schaeben, Texture analysis with MTEX–free and open source software toolbox, Solid State Phenomena, Trans Tech Publ, 2010, pp. 63-68.

[97] M. Knezevic, A. Levinson, R. Harris, R.K. Mishra, R.D. Doherty, S.R. Kalidindi, Deformation twinning in AZ31: influence on strain hardening and texture evolution, Acta Materialia 58(19) (2010) 6230-6242.

[98] S. Biswas, H.-G. Brokmeier, J.-J. Fundenberger, S. Suwas, Role of deformation temperature on the evolution and heterogeneity of texture during equal channel angular pressing of magnesium, Materials Characterization 102 (2015) 98-102.

[99] R.B. Figueiredo, T.G. Langdon, Grain refinement and mechanical behavior of a magnesium alloy processed by ECAP, Journal of Materials Science 45(17) (2010) 4827-4836.

[100] Q. Yang, A.K. Ghosh, Production of ultrafine-grain microstructure in Mg alloy by alternate biaxial reverse corrugation, Acta Materialia 54(19) (2006) 5147-5158.

[101] J.C. Tan, M.J. Tan, Dynamic continuous recrystallization characteristics in two stage deformation of Mg–3Al–1Zn alloy sheet, Materials Science and Engineering: A 339(1) (2003) 124-132.

[102] T. Al-Samman, G. Gottstein, Dynamic recrystallization during high temperature deformation of magnesium, Materials Science and Engineering: A 490(1) (2008) 411-420.

[103] A. Galiyev, R. Kaibyshev, G. Gottstein, Correlation of plastic deformation and dynamic recrystallization in magnesium alloy ZK60, Acta Materialia 49(7) (2001) 1199-1207.

[104] L. Jiang, J.J. Jonas, R. Mishra, A. Luo, A. Sachdev, S. Godet, Twinning and texture development in two Mg alloys subjected to loading along three different strain paths, Acta Materialia 55(11) (2007) 3899-3910.

[105] A. Kaya, Physical metallurgy of magnesium, Fundamentals of Magnesium Alloy Metallurgy, Woodhead Publishing Limited 2013, pp. 33-84.

[106] M. Lentz, A. Behringer, C. Fahrenson, I.J. Beyerlein, W. Reimers, Grain Size Effects on Primary, Secondary, and Tertiary Twin Development in Mg-4 wt pct Li (-1 wt pct Al) Alloys, Metallurgical and Materials Transactions A 45(11) (2014) 4737-4741.

[107] M. Arul Kumar, I.J. Beyerlein, C.N. Tome, Grain size constraints on twin expansion in hexagonal close packed crystals, J. Appl. Phys. 120(15) (2016) 155105.

[108] A. Styczynski, C. Hartig, J. Bohlen, D. Letzig, Cold rolling textures in AZ31 wrought magnesium alloy, Scripta Materialia 50(7) (2004) 943-947.

[109] D. Ando, J. Koike, Y. Sutou, Relationship between deformation twinning and surface step formation in AZ31 magnesium alloys, Acta Materialia 58(13) (2010) 4316-4324.

[110] I.J. Beyerlein, C.N. Tomé, Analytical modeling of material flow in equal channel angular extrusion (ECAE), Materials Science and Engineering: A 380(1) (2004) 171-190.

[111] S.B. Yi, S. Zaefferer, H.G. Brokmeier, Mechanical behaviour and microstructural evolution of magnesium alloy AZ31 in tension at different temperatures, Materials Science and Engineering: A 424(1) (2006) 275-281.

[112] Y. Estrin, S. Yi, H.-G. Brokmeier, Z. Zúberová, S. Yoon, H. Kim, R.J. Hellmig, Microstructure, texture and mechanical properties of the magnesium alloy AZ31 processed by ECAP, International journal of materials research 99(1) (2008) 50-55.

[113] M.R. Barnett, M.D. Nave, C.J. Bettles, Deformation microstructures and textures of some cold rolled Mg alloys, Materials Science and Engineering: A 386(1-2) (2004) 205-211.

[114] H. Ding, L. Liu, S. Kamado, W. Ding, Y. Kojima, Study of the microstructure, texture and tensile properties of as-extruded AZ91 magnesium alloy, Journal of Alloys and Compounds 456(1) (2008) 400-406.

[115] G. Faraji, M.M. Mashhadi, H.S. Kim, Tubular channel angular pressing (TCAP) as a novel severe plastic deformation method for cylindrical tubes, Materials Letters 65(19) (2011) 3009-3012.

[116] G. Faraji, H. Kim, Review of principles and methods of severe plastic deformation for producing ultrafine-grained tubes, Materials Science and Technology 33(8) (2017) 905-923.

[117] Y. Wang, H. Choo, Influence of texture on Hall–Petch relationships in an Mg alloy, Acta Materialia 81 (2014) 83-97.

[118] S.H.M. Azghandi, M. Weiss, B.D. Arhatari, J. Adrien, E. Maire, M.R. Barnett, A rationale for the influence of grain size on failure of magnesium alloy AZ31: An in situ X-ray microtomography study, Acta Materialia 200 (2020) 619-631.

[119] S. Agnew, P. Mehrotra, T. Lillo, G. Stoica, P. Liaw, Texture evolution of five wrought magnesium alloys during route A equal channel angular extrusion: Experiments and simulations, Acta Materialia 53(11) (2005) 3135-3146.

[120] R.Y. Lapovok, The role of back-pressure in equal channel angular extrusion, Journal of Materials Science 40(2) (2005) 341-346.

[121] V.M. Segal, Severe plastic deformation: simple shear versus pure shear, Materials Science and Engineering: A 338(1) (2002) 331-344.

[122] S. Ding, W. Lee, C. Chang, L. Chang, P. Kao, Improvement of strength of magnesium alloy processed by equal channel angular extrusion, Scripta Materialia 59(9) (2008) 1006-1009.

[123] M.R. Barnett, Z. Keshavarz, A.G. Beer, D. Atwell, Influence of grain size on the compressive deformation of wrought Mg–3Al–1Zn, Acta Materialia 52(17) (2004) 5093-5103.

[124] J. Jiang, A. Godfrey, W. Liu, Q. Liu, Microtexture evolution via deformation twinning and slip during compression of magnesium alloy AZ31, Materials Science and Engineering: A 483-484 (2008) 576-579.

[125] S. Balachandran, R.C. Elwell, D. Kang, R.E. Barber, T.R. Bieler, K.T. Hartwig, Nb Tubes for Seamless SRF Cavities, IEEE Transactions on Applied Superconductivity 23(3) (2013) 7100904-7100904.

[126] J.C. Springs, A. Srivastava, Z.S. Levin, R.E. Barber, K.T. Hartwig, Microstructure and Mechanical Properties of Heavily Worked and Recrystallized Copper for Low-Temperature Superconductor Applications, Ieee Transactions on Applied Superconductivity 27(4) (2017) 5.

[127] S. Balachandran, N. Seymour, R. Mezyenski, R. Barber, K.T. Hartwig, Microstructure and mechanical properties of fine grain seamless Nb tube by a novel shear deformation process, AIP Conf. Proc. 1574(1) (2014) 197-203.

[128] S.I. Hong, M.A. Hill, Microstructural stability of Cu–Nb microcomposite wires fabricated by the bundling and drawing process, Materials Science and Engineering: A 281(1-2) (2000) 189-197.